Delft University of Technology

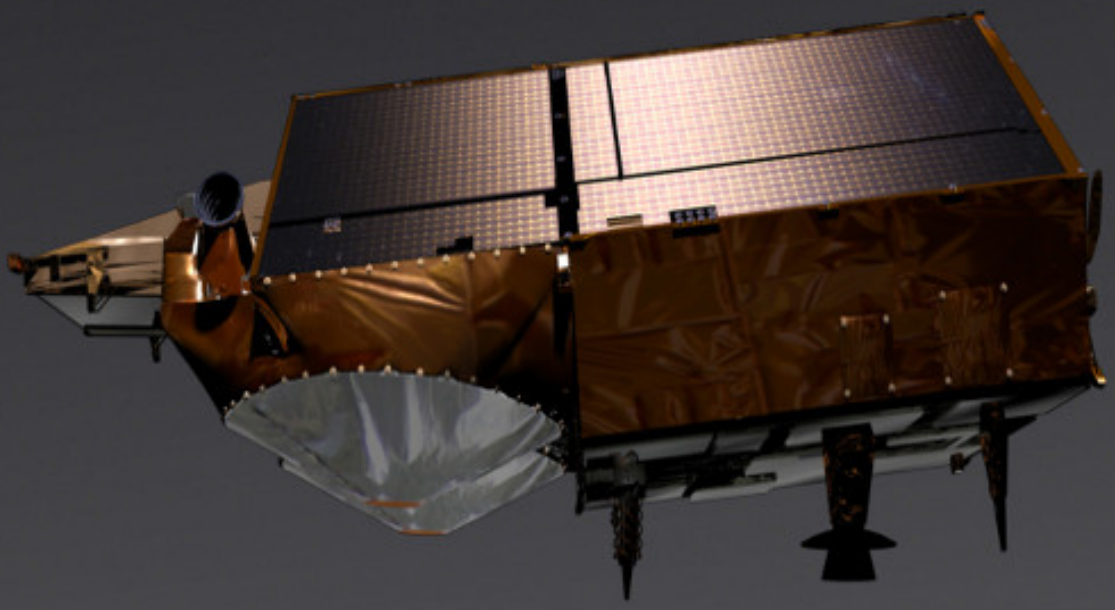

SATELLITE ALTIMETRY ON GREENLAND ICE SHEET MASS BALANCES

MSc Thesis - AE5810

ENEKO BERGARETXE OTAEGI

TU Delft Delft University of Technology

Challenge the future

Satellite Altimetry on Greenland Ice Sheet Mass Balances

MSc Thesis - AE5810

by

ENEKO BERGARETXE OTAEGI

in partial fulfilment of the requirements for the degree of

Master of Science
in Aerospace Engineering, Space-flight.

at the Delft University of Technology,
to be defended publicly on Friday 12^{th} of June, 2015 at 13:00.

Student number:	4254589	
Supervisor:	Dr. Ir. E.J.O. Schrama	
Thesis committee:	Prof. Dr. Ir. P.N.A.M. Visser,	TU Delft, AE
	Ir. M.C. Naeije,	TU Delft, AE
	Ir. D.C. Slobbe,	TU Delft, CITG
	Dr. Ir. E.J.O. Schrama,	TU Delft, AE

This thesis is confidential and cannot be made public until December 31, 2015.

TU Delft Delft University of Technology

Abstract

Throughout Earth's history the cryosphere, and more specifically its ice sheets, have responded to every major climate change event by expanding or retreating its extension pulled on the direction of the new climatic situation. Thus, for the currently ongoing climate change, the Antarctic and Greenland Ice Sheets hold a significant relevance as they are one of the most sensitive indicators of climatic changes. On this scenario, this thesis project studies the process of characterizing the mass changes on the Greenland Ice Sheet (GrIS) making use of satellite radar altimetry data provided by the K_a band altimetry mission SARAL/Altika. The data have been obtained from the RADS radar altimetry data base of the TU Delft.

One of the main focuses has been put into the characteristics of employing the radar altimetry techniques over ice sheets and the specific phenomena that need to be taken into account when computing range values. The slope-induced deviations have been estimated by calculating the along- and across-track surface slopes on the nadir direction and correcting for the deviation caused by these on the range estimates. The result has been satisfactory when compared with an independent DEM.

On a second phase of the project, the elevation changes have been computed at the intersections between ascending and descending tracks, the crossover points. Three methods have been used to analyse these elevation changes: an overall GrIS estimate that uses all crossover points as equal; a regionalized averaging method for the crossover points; and a Laplacian differential molecule method for adding a dynamic dimension to the regionalized data and thus have a smoother and better covered GrIS data. The regionalized methods have yielded a distribution of elevation changes where the north-western and north-eastern coastal areas are where the main ice loss is measured, while the interior areas show no change or a slight increase on the southern interior area.

By using the elevation change estimates, annual volume changes have been derived for each of the methods mentioned above. The resulting estimates are similar from one method to the other, giving an average of -272 $\pm$ 55 km^3/yr for the January 2013 - December 2014 period. When translated into annual mass balances using an effective ice density of 900 kg/m^3 a total mass change of -245 $\pm$ 50 Gt/yr is obtained.

This thesis has successfully calculated annual mass change estimates for the GrIS using SARAL/Altika measurements, results that come into agreement with the ones obtained in other independent studies. In addition, it has confirmed the validity of the applied methods for the correction of slope-induced deviations and the calculation of regionalized elevation changes. The availability of longer period data records and an improved re-tracking procedure could significantly improve the accuracy of the final results.

Preface

On the ascend of the public's awareness on the climate change, the monitoring of the Earth's cryosphere, and more concretely its ice sheets, has become one of the main information sources for the scientific community. On this scenario, studying the evolution of the Greenland Ice Sheet using satellite radar altimetry data and seeing through my own means how the ice is indeed on the decline has been a spectacular experience. During these months, I have been able to personally test the advances that satellite remote sensing missions are capable of providing on the Earth observation sciences and see how relevant these missions are for understanding the world that surrounds us.

This report is the result of these months of work, it collects the journey that I have made from taking raw radar altimetry measurements to identifying regional ice volume changes on the ice sheet that covers Greenland and estimating annual mass losses.

This thesis is the culmination of my experience at TU Delft, the end to a chapter in my life, it has been a great one. When I look back I see how I have become involved in a world of wonder where Astrodynamics, Space Exploration or Planetary Sciences have been my daily life. It has been a pleasant and life-changing journey and for that I want to thank the whole TU Delft and the Netherlands for giving me this chance. Heel erg bedankt!

Acknowledgements

I would like to use these lines to show my gratitude and appreciation to all the people that have lived through this project next to me. First, Ejo, thanks for making this possible, your help and guidance have been crucial for bringing this project to a good end, I have really enjoyed working under your supervision. It has been a pleasure. I am also very grateful to Marc Naeije, for his technical help and insight on the initial phases of this project. Third, I want to express my gratitude with the thesis committee members Prof. Dr. Ir. P.N.A.M. Visser, Ir. M.C. Naeije and Ir. D.C. Slobbe. Last, I can not express how grateful I am for all the great people that I have met on this time, thanks Anna, Francisco, Guillaume, Marco, Martijn, Pablo, Tiemen and all the people at 9^{th} floor; and of course, thanks to my family and specially Andrea. Thank you all very much for staying next to me with your unconditional support at every moment, I hope we all continue being close in the coming experiences.

On a special mention, I would also like to thank the Basque Government, Eusko Jaurlaritza, for funding mine and many other students' MSc studies abroad. This MSc degree has been developed with the funding of the scholarship *"EAErentzako interesgarriak diren gaietan, 2013-2014 ikasturtean, atzerrian espezializazio-ikasketak egiteko beka"*.

Eneko Bergaretxe Otaegi
Delft, April 2015

Contents

List of Figures

List of Acronyms

AIS	Antarctic Ice Sheet
BP	Before Present
BRAT	Basic Radar Altimetry Toolbox
BRF	Burst Repeat Frequency
CHAMP	Challenging Mini-Satellite Payload for Geo-scientific Research and Applications program
CNES	Centre National d'Études Spatiales
CryoSat-2	Cryosphere Satellite
DBL	Data Block File
DEM	Digital Elevation Model
DEOS	Department of Earth Observation and Space Systems
DORIS	Doppler Orbitography and Radiopositioning Integrated by Satellite
ERS	European Remote Sensing
ERO	Exact Repeat Orbit
ESA	European Space Agency
GDR	Geophysical Data Record
GMT	Generic Mapping Tool
GOCE	Gravity field and steady-state Ocean Circulation Explorer
GRACE	Gravity Recovery and Climate Experiment
GrIS	Greenland Ice Sheet
GRL	Geophysical Research Letters
GUI	Graphic User Interface
HDR	HeaDeR file
ICGEM	International Centre for Global Earth Models
ISRO	Indian Space Research Organization
LGM	Last Glacial Maximum
LRR	Laser Retro-Reflector
NASA	National Aeronautics and Space Administration
NetCDF	Network Common Data Form
NGA	National Geospatial-Intelligence Agency
NOAA	National Oceanic and Atmospheric Administration

NSIDC	National Snow and Ice Data Center
PIOMAS	Pan-Arctic Ocean Modelling and Assimilation System
POE	Precise Orbit Ephemeris
PRF	Pulse Repetition Frequency
RADS	Radar Altimeter Database System
RCU	Radiometer Calibration Unit
SAR	Synthetic Aperture Radar
SARAL	Satellite with ARgos and ALtika
SARM	SAR Mode
SIRAL	SAT Interferometric Radar Altimeter
SLR	Satellite Laser Ranging
SRS	Satellite Remote Sensing
SSH	Sea Surface Height
TTC	Telemetry, Tracking and Command

1 Introduction

The topic of this thesis is related one of the most relevant global scale events that is defining the future of the planet as well as humankind's, the warming of global temperatures. The study of the Earth's cryosphere has become the field where the first major scale signs of the climate change can be observed and thus the scientific community has committed its efforts into the monitoring of the Earth's icy elements, with special focus on the Greenland and Antarctic ice sheets. The main goal of this monitoring is to be able to analyse, quantify and predict how the cryosphere is evolving and decide what the best actions are to prevent dramatic situations in the future.

With the necessity to cover vast land areas in some of the most inhospitable regions of the world, the application of satellite remote sensing techniques like altimetry or gravimetry have become the main tool for the study of the evolution of the Earth's ice sheets. Currently, two operational missions make use of radar altimetry to measure the variability of the ice volume on the ice sheets, SARAL/Altika by the CNES and ESA's CryoSat-2, with more planned for the future.

This thesis project is set on this background and attempts to contribute to the calculation of annual ice loss estimates. On the next sections a detailed description of a few general aspects of the thesis project are presented; the motivation 1.1, the research question or objective 1.2 and the structure of the report 1.3.

1.1. The Motivation

The confirmation of humanity's role on the global warming process as explained on the IPCC report released on 2007 [7] has brought the Earth's cryosphere into the spotlight of the scientific community and even the general public's interest. Earth's ice sheets are a crucial element for the global climatic and hydrological equilibrium, as they are one of the most sensitive elements on the planet.

Alongside the relevance of the climatic change, the last forty years have seen the rise in the amount and performance of satellite remote sensing technology, instrumentation and applications to observe the evolution of the Earth. Their advantageous point to provide on both spatial and temporal coverage and resolutions makes them an extremely useful tool to study Earth's cryosphere. As mentioned in the introduction, currently, there are two main missions gathering radar altimetry data over the ice sheets, SARAL/Altika and CryoSat-2, launched on February 2013 and April 2010, respectively.

Recent results using CryoSat-2 and older missions data show a decreasing trend on the total ice masses of the ice sheets, as published by Zwally et al. 2011 [8], McMillan et al. 2014 [9], Sørensen et al. 2011 [10] or by Helm et al. 2014 [11]. These publications all agree on the overall trend describing the regional evolution of the Greenland Ice Sheet (GrIS) and the Antarctic Ice Sheet (AIS). However when quantifying the amount of annual mass loss some divergences appear, specially when taking

results from independent measurement methods like gravimetry, laser or radar altimetry.

This situation presents an interesting chance to test the issues related to the use of radar altimetry techniques over the Earth's ice sheets, as most of the ice melt, as reported on the above mentioned sources predominantly happens on the coastal areas where the ice sheet surface shows the most abrupt changes and steepest slopes. In addition, the availability of almost real-time altimetry measurements at the TU Delft radar altimetry data base (RADS) from the SARAL/Altika and CryoSat-2 missions sets the perfect chance to attempt the characterization of the evolution trend of the ice sheets and estimate the amount of these variations.

1.2. Research Objective

The research objective of this thesis project has been defined in the following way:

"To calculate ice mass change estimates of the Greenland ice sheet using radar altimetry data."

1.2.1. Intermediate Goals

On the pursue of the main research goal some intermediate milestones or goals have been identified. They are listed in the following points.

- To compute atmospheric, geoid and instrumental error corrected thickness estimations for the GrIS
- To compute 2D terrain slope-induced radar range corrections over the GrIS and to apply them to thickness estimations
- To identify crossover points and compute elevation changes at these crossover points
- To estimate annual volume and mass changes on the GrIS from the crossover point elevation changes applying different methods
- To compare the obtained mass and volume change estimates to other results that use independent methods and to assess the validity of the applied methods

This set of goals is considered within the challenge of reproducing the results of those state-of-the-art estimations, as well as with the ambitions of optimizing the calculations by introducing and analysing new methods and models.

1.3. Structure

The work effort has been structured in a bottom-to-top scheme, where the starting point has been handling the raw satellite altimetry data bundles and going through different processing steps at a time until the final estimation of mass changes on the GrIS has been achieved. The report is thus, organized in a similar pattern, where the first chapters introduce the main concepts and phenomena, while the later ones describe the applied data processing schemes and the obtained results.

On the initial chapters the main theoretical aspects related to the research objective are presented; introducing the characteristics of Earth's cryosphere and its dynamics on chapter 2; reviewing the concept of ice sheet remote sensing with radar altimeters on 3 and with a brief description of the main currently on-going radar altimetry missions 4.

The 5^{th} chapter introduces the hardware and software resources that have been necessary for the development of this project. It also includes a description of the satellite and other scientific data resources that have been used.

On chapter 6 the initial satellite data processing is explained, with the pertinent corrections and verification procedures also being described. Chapter 7 introduces the concept of crossovers and describes the processing applied on the satellite data to compute the elevation changes on these crossover points. With the elevation changes available, the analysis of the processed data has been done and the corresponding volume and mass changes are presented on chapters 8 and 9.

On the last chapters of the report; the general discussion of the obtained results and implemented methods is presented, chapter 10; followed by the conclusions and the recommendations for future work chapter 11.

2

Glaciology

Glaciology as the science that studies the phenomena related to ice sheets, glaciers and other icy elements has been responsible for the characterization of the Earth's cryosphere and its dynamics, as well as for explaining their origin and evolution through the geological epochs. This area of science is to some extent the meeting point or overlapping between many scientific areas such as: geology, geophysics, meteorology or hydrology. All these areas when working under the constraints of the cryosphere, the portion of the Earth where water is in its frozen state, form the science known as glaciology.

This chapter gives a brief introduction to the scientific area of glaciology, describing some of the main concepts and elements that will be extensively used throughout the whole report. The first section 2.1 presents the main characteristics of the Earth's cryosphere and its current state, while in a second part 2.1.2 the dynamics of the cryospheric system are explained.

2.1. Cryosphere

Currently, the Earth's cryosphere is composed by the Antarctic Ice Sheet (AIS), the Greenland Ice Sheet (GrIS), ice caps, sea ice, glaciers and frozen ground (permafrost). The dependence of the cryosphere on the planet's climatic conditions is enormous and vice-versa. As mentioned on the introductory chapter, the sensitivity of the cryosphere to the changes in the global climate makes the study and understanding of the processes that shape its evolution a priority for the scientific community. As a matter of fact the slightest changes on the evolution of the Earth's cryosphere could lead to unforeseeable and tremendous changes on the planet's climate and hydrology, in fact the ice sheets (GrIS and AIS) contain 76% of the world's freshwater resources, equivalent to a 68.1 meters sea-level rise and the future evolution of hydrological cycles strongly depends on them. Competition for water resources has in the past been a matter of dispute and could lead to a deterioration of the current situation in a water-cycle scenario change as mentioned by Thorsteinsson et al. 2013 [12] and B. Chellaney 2011 [13].

Since the formation of the Earth, some 4500 million years ago, the surface of the Earth has undergone various geological phases that brought extreme climatic conditions and extreme surface shaping processes. The glacial periods are the cold extreme of these processes, time periods where the planet is under cooled temperature conditions and considerable areas of the planet are frozen. These periods are triggered by complex mechanisms that set up special conditions that allow the cooling of global temperatures, like orbital variations or decreases on carbon dioxide and greenhouse effects. During the Earth's evolution several glacial ages have been identified, in fact, the planet is currently at an Ice Age, the Quaternary Ice Age.

The Quaternary Ice Age has cyclically expanded and retreated during glacial maximum and minimum periods during the last 2.58 Myr. Currently the planet is at a glacial minimum or interglacial known as the Holocene that started at 10-12 Kyr BP (Before Present). After the dynamic started at the Last Glacial Maximum (LGM), 18 Kyr BP, the increase on the global temperatures led to the melting of major ice sheets and glaciers, on the Northern Hemisphere both the Laurentide and North European ice sheets have completely disappeared (only the GrIS and the Arctic Sea ice remain). The Patagonian ice sheet has also melted during this time. Due to this melting, the amount of water now being part of the hydrological cycle of the oceans is higher, the sea-level has risen 120 m and vast land areas have been covered by water.

The LGM period has strongly influenced the characteristics and shape of the present planet; its consequences are still a relevant factor for many Earth science studies. As an example, the Earth geoid and the gravitational potential are affected by the Glacial Isostatic Adjustment (GIA) 2.1.2, the rebound of the ground that once was compressed below the past ice sheets.

2.1.1. Current Cryosphere

The present cryosphere is mainly composed by the Antarctic and Greenland ice sheets (AIS and GrIS) that contain 99% of the total glacial ice in the planet and around 76% of the total freshwater reserves.

Earth's cryosphere has considerably changed due to the climatic warming started with the Holocene period. After the melting of the Laurentian, South American and North European ice sheets only the highest latitude ice sheets, around 60° latitude or above, have survived the first 12 thousand years of the Holocene. Both together contain 25.71 (AIS) and 2.85 (GrIS) million cubic kilometre of ice, the equivalent to around 68.1 meters rise of the sea-level, as stated on the IPCC 2003 report [14]. In addition, the increased global warming has speeded up the warming and therefore the melting.

Extensive study of their recent past evolution shows that the GrIS is responding to the global warming with much faster melting speed records, while the general dynamic of the AIS is not completely clear with diverging behaviours in its different regions (West and East divided by the Transantarctic mountains). The estimates from different technique and campaigns do not fully agree when quantifying the mass variations of the ice sheets; however they reach a consensus on the general trend of the dynamic. This consensus acknowledges a relevant melting of the GrIS and WAIS, while the EAIS shows a slight increase on its total mass for some regions, Shepherd et al. 2012 [15] or Zwally et al. 2011 [8].

The next section introduces a more detailed description of the Greenland Ice Sheet, as it is the main focus of this study.

Greenland Ice Sheet (GrIS)

The GrIS represents around the 10% of the world's ice mass with 2.85 million cubic kilometres of ice, 7.2 meters of sea level equivalent variation. As can be seen in figure 2.1 the thickness of the GrIS gets bigger in the centre of the island, with greyer levels depicting thicknesses up to 3200 meter. The GrIS is located approximately between the latitudes 60 and 82. The current measurements, Shepherd et al. 2012 [15], estimate an annual mass lose of 142 $\pm$ 49 Gt for the period between 1992-2011 and of 263 $\pm$ 30 Gt for the 2005-2011. The consensus also enables to state that the general trend is that of an accelerated melting of the GrIS, with values up to annual -278 $\pm$ 19 Gt/yr and -31 $\pm$ 3 Gt/yr^2 acceleration calculated with gravimetry measurements from GRACE between 2003 and 2010, Schrama et al. 2011 [16].

There are indications of the existence of ice sheets in Greenland as early as the Miocene, 18 million years ago. However, the current ice sheet is considered to have appeared on the last glacial advance and established during the last 110.000 years. Since the LGM, during the interglacial period it has experienced a considerable retreat, which with the current dynamic could end in the complete de-glaciation

of the GrIS, what could be irreversible according to the IPCC 2007 report [7].

Due to the location compared to the AIS the annual period at which the GrIS is receiving solar radiation is considerably higher, and thus the melting. In addition, the effect of the ocean currents that interact with its coastal climate and areas lacks the isolation that the Antarctic Ocean currents provide the AIS with. Together with this, the extended melting of the Arctic Ocean ice is also related to this change in the ocean current circulation on the north hemisphere. All these factors make the GrIS specially vulnerable to the changes in global temperatures.

As published by Enderlin et al. 2014 [17], the main part of the ice mass discharge, 42% for the period 2000-2012, is happening on 5 outer glaciers on coastal areas like the Jakobshavn Isbræ, Helheim, Petermann, and Kangerdlugssuaq. However, in the same article he also notes that the relevance of the discharge mass loss on the overall mass loss by the GrIS is decreasing as the surface melting and run-off increase. This gives an overview of the elevation change patterns that the radar altimetry will deliver.

Figure 2.1: **The GrIS over Greenland. [Credit: Wikimedia Commons]**

2.1.2. Cryospheric Evolution Dynamics

Regarding the motion of the cryospheric elements, the main leading forces are the gravitational, structural and frictional forces that act on the ice masses. Factors like, the slope, the temperature, the structure, the viscosity profile, the thickness of the shelf or the amount of melting on the base are relevant factors for characterizing the evolution of the cryospheric elements.

In addition, the interaction with the hydrological systems and geological processes also affects the

shape and dynamics of the ice layers and are therefore described in the following paragraphs too.

Ice sheet & Glacier Motion

The general motion of glaciers and ice sheets is driven by the gravitational force in contraposition to the friction from the basal drag. This creates a basal shear stress on the direction of the slope dependent on the angle that pulls the ice mass down slope.

The general pattern of the motion could be compared to the flow of other fluids, where there is a relation between the shear stress applied to the mass and the strain produced. Ice mass flow is ruled by the Glen-Nye Flow Law that links the amount of shear stress to the shear strain rate [18].

$$\dot{\epsilon} = K\tau^n \tag{2.1}$$

Where $\dot{\epsilon}$ is the shear strain rate, K is dependent on temperature, τ stress and n is another constant related to the ice's stress-strain relation.

Following this equation, ice shows behaviours in between fully viscous (n = 1) and perfect plastic relation (n = ∞), although the common values used in studies range from 1.5 to 4.0. Like in the case of other viscous fluids the flow is faster in the centre of the ice mass than in the boundaries (ground or sides), this is also depicted in figure 2.2.

However, the contribution of the friction forces to motion of the ice masses is much more complicated than the pure surface friction example. The heat produced from friction itself, in combination with the geothermal heat from the ground, melts the base of the ice sheets or glaciers, what leads to a basal sliding effect. The basal melt water acts as a lubricant for the motion of the mass on top of this melt ice layer. The complicated hydrological flow systems present on the subglacial depths on ice sheets make it even more difficult to correctly simulate their motion.

Examples of the result of basal melting are the 'seasonal waves', where clear advance differences can be observed between the seasons by the variations on the sliding velocity due to more extended basal melting and water run-off. On the dynamic of the ice masses, other kinematic waves that produce undulations on the downwards direction are also common, but do not show much faster speeds than the surface speeds. During their life-cycles glaciers produce an enormous eroding effect on their surroundings, specifically on their basal and side rocks and ground, shaping what after their retreat remains as valleys and fjords.

On the following paragraphs a few phenomena that have an effect on the ice sheet dynamics and the measurements done on them are introduced.

Ice Streams

Ice streams occur when through basal melting and the deeper carving of channels in which the ice flows, the ice flow becomes increasingly more rapid. This creates a positive enhancement cycle as a higher speed induces further melting and carving, through friction with the ground, leading to even more rapid flow of these parts of the ice. Such streams can reach speeds as fast as 10 kilometres per year, as in the Jakobshavn Isbrae in Greenland or the Lambert Glacier in the AIS.

Ice Shelves

Ice shelves are formed when an ice sheet slides over the limits of the continental lands and expands into the sea. The grounding line is the contact point of the shelf with the continental ground and where the floating shelf on the sea starts. As can be seen in 2.2 most of the shelf is under the sea-level, usually around 90% of the volume; depending on the specific densities of the ice and the local water

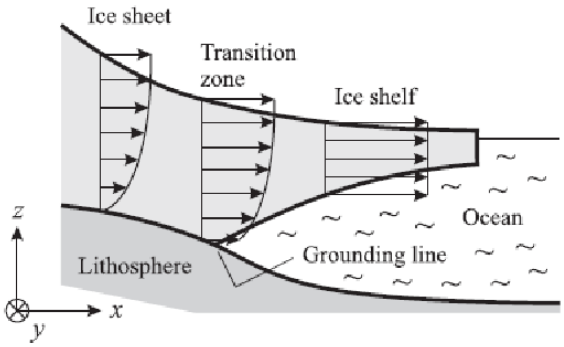

Figure 2.2: **Ice shelves structure. [Credit: Greve et al. 2009 [1]]**

this proportion will be different. The ice shelves thickness can go from 100 to 1000 meters.

The ice shelves show a specific discharge process, called calving, where big parts of ice break off and float out into the ocean, creating icebergs or becoming part of sea ice. This process involves warm-cold water forming currents below the ice shelf, where after the contact with the ice shelf in the grounding line area the cooled water with higher density goes down into deeper ocean. This process slowly warms and thins the ice shelf, severely in the outer areas, and the 90% underwater volume proportion is slowly diminished until the water's buoyancy cannot hold the remaining volume outside the water. This process is worsened by the cracks and water run-off happening in the surface of the shelves that slowly erodes the structure and speeds up the calving.

Apart from the expansion and discharge processes, the ice shelves are quite dynamic, as they lay on top of a sea. The tides on the oceans also affect the ice shelves as these tidal variations can be observed on their elevation, even kilometres inland from an ice shelf.

On the present Earth ice shelves are present on both ice sheets, but are much more relevant on the AIS. The main ice shelves are the Ross Sea and the Filchner-Ronne Ice Shelves, with around 400.00 km^2, however, currently there are many smaller ones in the AIS and GrIS that are suffering much severer retreats.

Global Isostatic Adjustment

The GIA is the response of the crust that was once compressed by the weight of the ice sheets during the past glacial advances that is now growing back to its isostatic, pressure free, state (R. Sabadini and B. Vermeersen [19]). Therefore in the areas where this adjustment is going on, the main effect is that an increased elevation of the surface crust is measured within the rest of the data that can alter the results if it is not accurately modelled. The outermost layer of the Earth, the crust, shows mostly elastic solid behaviours, while deeper layers show more viscous responses. Therefore the response given by these layers to the glacial retreat on top of their areas is very different. For the correct determination of the GIA the characterization of the viscosity profiles of the Earth's surface layers is very relevant, in some research the inverse process is applied, where GIA measurements are used to estimate the crust's properties.

Currently, the areas that show GIA adjustments are the ones that had considerable ice sheets during the last glacial advance; the northern American continent shows a considerable uplift of its crust, as well as northern Europe. South America shows some GIA where the Patagonian ice sheet existed during the last glacial maximum.

Regarding the Antarctic peninsula the GIA is only measured in the western part of it and in a small scale, while in the east part the ice is vastly still present and even causing some sinking of the ground land.

3

Satellite Remote Sensing

Observational sciences have always relied heavily on the acquisition of information through remote sensing techniques, without making physical contact with the target object. The advantageous position that satellite technologies provide for direct observations has enabled the development of one of the most powerful techniques for studying and monitoring the evolution of our planet, **Satellite Remote Sensing (SRS)**.

A wide variety of technologies have been designed for SRS purposes like altimetry, gravimetry or sonar technologies. Each of these set different design characteristics for the measurements; providing different data type outputs, setting different operational requirements or working under different conditions. All these different techniques offer extended design and development options for the design of observation missions.

On this chapter the focus is put into the **Altimetry** remote sensing technique, as it is the central interest of this project. On the next sections, first, the physical principles are introduced 3.1, while a detailed description of its sources of error and deviation 3.1.1 is provided afterwards. On the last section of this chapter the specific scenario of the radar altimetry over ice sheets is considered 3.1.2.

3.1. Satellite Altimetry

An altimeter is an instrument that measures the altitude of a surface with respect to a reference. In the case of space-borne altimeters they are used to determine the range between the orbiting spacecraft and the terrain above which it is flying. This range data is referenced to the orbit altitude of the satellite itself and through a simple geometric subtraction of the altitude and the range, the profile of the sampled terrain topography with respect to the Earth's gravitational centre is obtained. In this process the determination of the pointing of the signal transmission needs to be considered, as this will define the point at which the pulse will get reflected and the geometry of the signal's travel.

The basic principle behind altimetry is the two-way echo time-delay measurement, where the satellite emits an electromagnetic pulse that travels down until it is reflected by the target surface and then the echo is detected on its way up to the orbit height 3.1. From the time that the radiation takes to travel this two-way trip the range can be derived using the speed for the radiation's propagation on the atmosphere,

$$r = \frac{c(T_R - T_T)}{2} \tag{3.1}$$

T_R being the reception time; T_T the transmitted one; c the speed of light and r the range between the satellite and the terrain. On the ideal case these profiles of ranges could be converted into Earth's geoid's reference frame by subtracting the satellite's orbit altitude and thus get Earth centred elevation profiles.

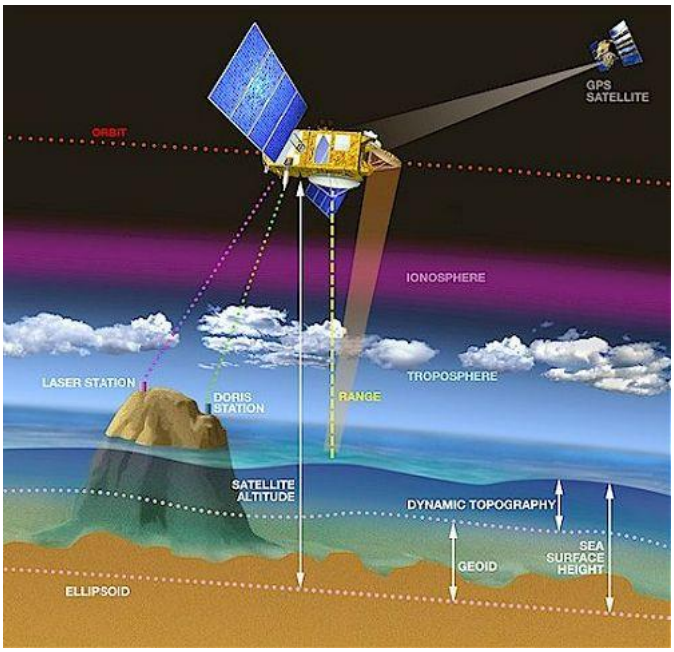

Figure 3.1: **Altimetry measurement technique, two-way range determination. [Credit: ESA Earth Observation]**

However, altimetry is not as simple as this, the signals used and the interactions of these with the atmosphere and the surface are a complex phenomena. The radiation used for altimetry is selected from a wide spectrum of frequencies and the use of complex signals is necessary to do the measurements, as well as many corrections and processing to extract the correct values from the raw range data.

The electromagnetic signals used for altimetry use a pulse-limited altimetry technique in order to enhance the spatial resolution of the size-constrained antennas. This technique is based on sending radiation separated on pulses of a specific length with a width of $c\tau$, although in radar altimetry continuous wave frequency modulation is used instead of real radiation pulses, this is further explained in the next section. This gives a body to the signal that gets modified on reflection; this process is depicted on 3.2. As it can be observed, the spherical transmission of the wave makes contact at the nadir point of the satellite and the first part of the radiation gets reflected towards the satellites altitude. The reception of this signal at the satellite takes a characteristic waveform, as the different parts of the pulse get reflected in an equidistant manner from the centre, circles.

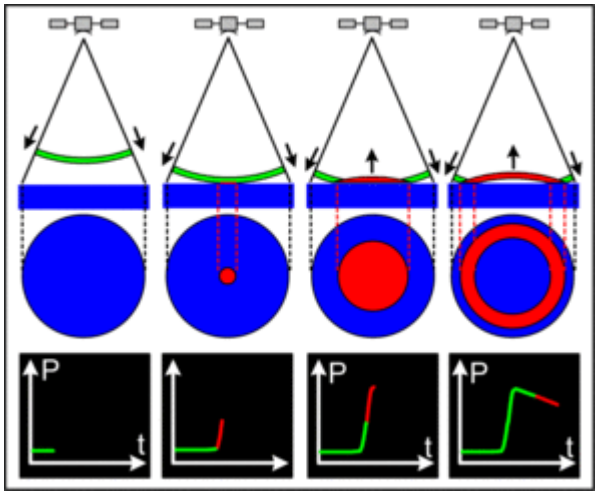

Figure 3.2: **The pulse-limited signal reflected on a flat surface. [Credit: CNES Aviso+]**

These circles are received at the satellite at the same time, together with more centred parts that made contact later. Therefore the waveform of the received radiation can theoretically be calculated. On the next figure 3.3 the waveform of the power received from a pulse reflected on a flat surface is depicted and the information that can be extracted from it is explained. P_0 corresponds to the background noise at the receiver and P to the actual reflected power from the pulse; from this the backscatter coefficient is obtained. The epoch at mid-height gives the value of the time delay for the contact with the surface, from which the range can be derived. However the determination of this point is dependant on the re-tracking algorithm being used for the processing of the waveforms. The leading edge slope is linked to the surface slope variations of the terrain. The trailing edge slope is related to the pointing error of the antenna and the signal penetration. The leading edge width can be related to penetration on the reflective medium, like in the case of ice.

Figure 3.3: **The waveform received at the satellite from a pulse-limited beam reflected on a flat surface. [Credit: CNES Aviso+]**

As the ability of the receiver to correctly receive the waveforms is limited to a range-window and the satellite's orbit flies over huge altitude variations, in order to keep the correct receiving of the waveforms going on some post-processing is done on-board the satellites. An estimation of the range value is done and the earliest part of the received signal is located within the tracking window by the tracker algorithm.

One interesting concept, and a magnitude that carries a lot of information, is the backscatter coefficient, the relationship between the emitted and received power is described by this equation [3]

$$\sigma_0 = \frac{(4\pi)^3 R^4}{t_\lambda^2 G_0^2 \lambda^2 A_{eff}} \frac{P_R}{P_T} \tag{3.2}$$

where G_0 is the boresight antenna gain; R the range to the nadir point; P_R and P_T the received and transmitted power; λ is the wavelength of the signal; τ_λ the atmospheric transmittance at λ wavelength; A_{eff} the effective area of antenna footprint.

3.1.1. Corrections for Range Estimations

In every remote sensing measurement there are several phenomena that affect the accuracy of the range measurements. These are related to the instrumental set-up, the medium through which the signal travels, the medium with which the signal makes contact (the target) and the processing scheme used for calculating the value of the range. The next sections give an introduction to these, for which the book by A. Cazenave and L.L. Fu has been used as a source [3].

Instrumental Error

Instrumental errors are inherent to any kind of measurement, as every set-up has its own limits and can lead to a significant over- or under-estimation of the range measurement values. These are some of the most relevant for the altimetry measurements.

The **pointing error** on the nadir direction can decrease the accuracy of the data by shortening the travel time that the signal needs to meet the first contact point, the off-nadir pointing is linked to the attitude determination accuracy of the satellite system.

The **oscillator drift error** is related to the measurement of time within the satellite, where the time is calculated by counting oscillator cycles. This method is affected by the ageing of the oscillator and the degeneration of the detector crystal, that makes a weekly calibration necessary. This calibration is done using the telemetry signal from an oscillator in the ground.

The **Doppler shift effect** is produced due to the velocity of the spacecraft on the direction of the transmitted pulse in both the transmission and reception events that changes the frequency of the received final signal.

The **tracker response error** is related to the tracker, the system that takes care of the on-board adjustment of the reception window to receive the reflected signals within the window's limits. The error is produced by not taking into account the range acceleration variations.

These errors are generally closely related to the satellite system and the status of the mission, therefore the satellite data releases include the corrections to be applied to the range estimation so that the final user can easily access and apply them.

Atmospheric Error

Regarding the deviations caused by the interaction of the signal with medium that it crosses on its way to the target, generally the atmosphere, these are the phenomena to take into account.

The **ionospheric correction** is related to the amount of free electrons in the ionosphere, a parameter heavily dependent on the solar activity that ionizes them and the satellite's position with respect to the sun. These electrons interact with the radar pulses travelling both ways delaying their transmission, what leads to an over-estimation of the range values.

As for the **tropospheric delay**, it can be separated into two types: the **wet** and **dry tropospheric effects**. The wet is related to the delay caused by water vapour on the atmosphere, while the dry one

is caused by the refraction of the radiation by dry gases on the troposphere.

The corrections are done by using deviation calculation models or directly calculating the deviation using updated data from meteorological, solar activity and atmospheric composition profiles. In some other cases radiometers are incorporated to the instruments in order to identify the interacting elements on the atmosphere and thus better quantify the errors.

Geoid

Another relevant deviation in the measure of altimetry data is the geoid's variations, an integrated signal of the mass distribution changes on the globe through tectonic activity or the glacial isostatic adjustment. The model used for the geoid referencing changes the gravitational potential and thus the orbital trajectories, but also varies the distance of the bedrock from the centre of the Earth. Therefore this bedrock distance variations need to be identified and accounted for, as this leads to an increase or decrease on the elevation of the terrain below the satellite, while the actual range to the target may not have varied.

Other minor deviations related to the variation of the Earth's geoid are the **load tide** and the **solid Earth** corrections. The former is related to the deformation caused by the weight variations on top of the different areas on the Earth, while the latter is related to the deformation caused by the gravity of other gravitational bodies of the solar system, W.E. Farrell 1973 [20].

The Re-tracking Algorithm

A key element on the post-processing phase of the mission that can significantly improve the range estimation accuracies is the re-tracking of the waveform measurements. The significant range variations on the surface of the ice sheets lead to errors on the on-board range estimations and are the cause of a deviation on the waveform's leading edge from the altimeter tracking window. On this process an algorithm is used to re-estimated the waveform processing phase in more detail than the one done on-board.

There are several algorithms that can be used for the retracking of the waveforms, however each satellite system works better with different algorithms and the search for the most appropriate one is one of the ongoing objectives of the scientific community. Due to the time and effort constraints on the development of this project this topic is left uncovered and it is assumed that the re-tracking applied at ESA and CNES on the CryoSat-2 and SARAL/Altika data found on the RADS library is good enough. Some research estimates that this may lead to errors of the order of 15 meters for the data measurements, Forsberg et al. 2013 [21].

3.1.2. Altimetry on Ice Sheet Surface

Although the general pattern of altimetry follows the principles above introduced, a lot more elements are involved in achieving precise measurements over ice with this technique. The medium and conditions in which altimetry is being applied have a major role on the final range calculation and the Earth's ice sheets represent a considerably different medium in which to apply altimetry.

Due to the physical characteristics of the ice sheets, a close attention has to be put into the specific characteristics of a rebound signal from them. Many phenomena are directly derived from the geometry, physical characteristics and structural composition of the ice sheets, as for example; the terrain's surface characteristics (slope and undulations); the interaction of the radiation wave with the surface; the amount of penetration of the signal into the top ice or measurements on ice margins.

The main effect of these phenomena, is the uncertainty to precisely estimate the geodetic position of the altimeter footprint and the migration of the midpoint of the leading waveform edge respect to the

altimeter tracking gate. In addition the back-scattering irregularities due to the radar signal penetration and volume back-scattering cause deviations on the shape of the returned waveform, reducing the accuracy. On the following paragraphs specific features of the observed phenomena; the slope-induced deviations, signal penetration and volume scattering on the ice sheet measurements are described.

Slope & Undulations

The slope and undulations on the ice sheet's surface are the cause of the biggest of the surface feature errors. The non-perpendicular surface on the nadir direction makes the first contact point of the signal, and the point where the first rebound is generated, to be out of the nadir direction. This, as a consequence, reduces the real range value of the nadir point. This is depicted on figure 3.4.

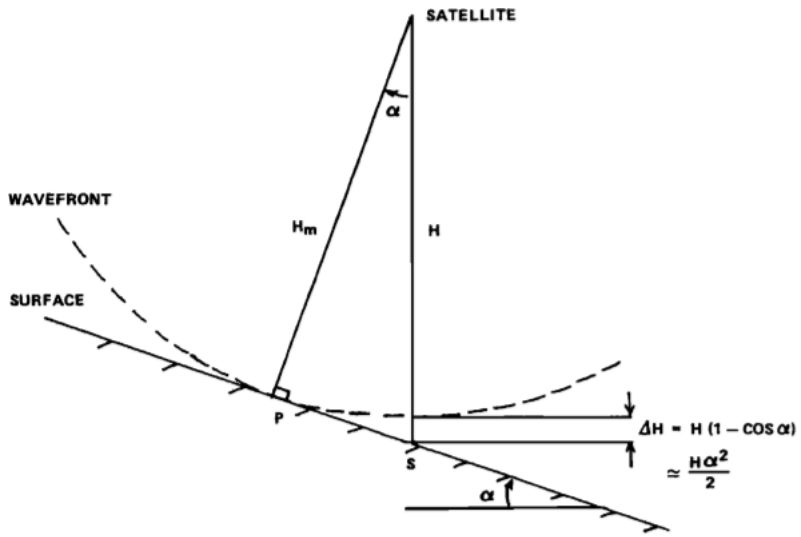

Figure 3.4: **The slope correction geometry. [Credit: Brenner et al. 1987 [2]]**

According to the analysis done by Brenner et al. [2], there are two main methods for the correction of this error: the relocation and the slope-correction method. The first method estimates the real position of the first contact point and modifies the location data of the measurement to a new position. The second method instead uses geometrical relations to estimate the real value of the range data at the nadir point and corrects it. The article concludes that for the cases in which the across-track error is negligible the relocation method is preferred. However, when slopes in both dimensions are considered the slope-correction method is the most efficient.

For this project, as both slope dimensions are considered the slope-correction method is selected. As it can be seen on figure 3.4, the following equation gives the value of the vertical displacement of the first contact point with respect to the nadir contact point:

$$H = \frac{H_m}{\cos\alpha} \tag{3.3}$$

$$\Delta H = H(1 - \cos\alpha) \approx H\alpha^2/2 \tag{3.4}$$

H being the height and α the angle relative to the vector normal to the reference ellipsoid, which also corresponds to the slope in the ice sheet surface. On the horizontal sense the displacement is given by the next equation.

$$\Delta S = H \ \cos\alpha \ \sin\alpha \tag{3.5}$$

These equations describe and correct the deviation in a two-dimensional manner, however, the satellite tracks encounter significant slopes on the direction perpendicular to the flight path. This is why the

slope on both directions the flight-path or along-track slope and perpendicular across-track slopes are required to estimate the deviation.

From these relations a depiction of the deviations caused on the range measurements by the surface slopes (0°-1.0°) can be found on figure 3.5. This shows that the deviation for a 1° surface slope amounts to 120 meter in the range measurement and for a 0.4° slope the error is of 19 meter. Therefore the proper estimation of these angles is very relevant to estimate the range on the nadir direction correctly.

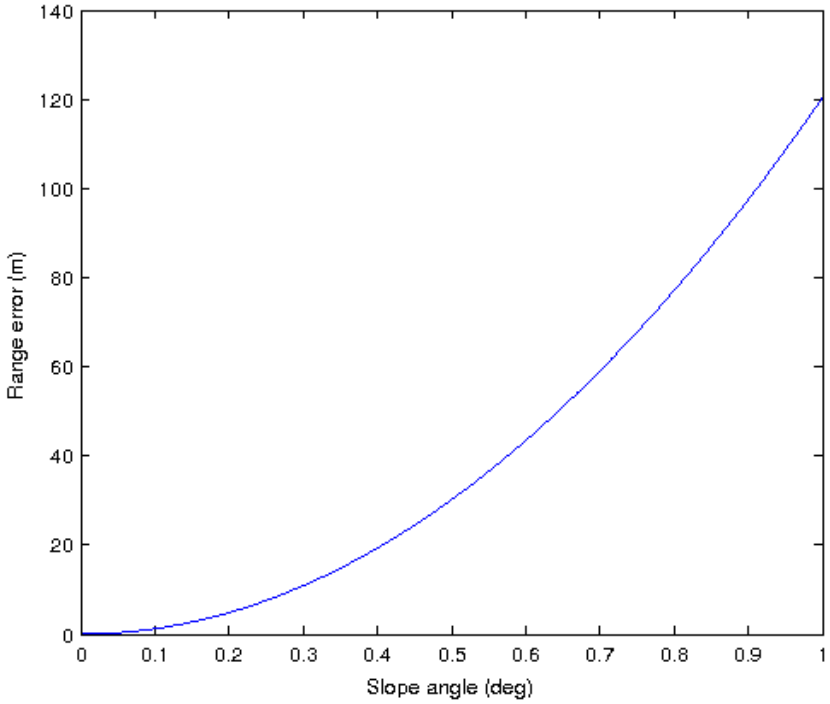

Figure 3.5: **The range deviation (m) caused by the surface slope angle (◦) on the range measurements at 790 km altitude for SARAL/Altika.**

The method used to correct these slope-induced deviations is described on section 6.3.2, where a topographic model of the GrIS terrain, a digital elevation model (DEM), is used to estimate the along- and across-track slopes for each range measurement. The accuracy of the DEM considerably affects the precision at which the range measurements will be corrected. The used DEM has been created by DiMarzio et al. 2007 [22] using measurements from the ICESat mission as described is section 6.3.1.

Signal Penetration and Sub-surface Volume Scattering

The snow firn's densification to form ice sheet layers is a long and complex process that most of the cases leaves the upper few meters of the ice sheets fractioned into grains of more and less dense ice. This allows for the microwave radiation to penetrate these unformed layers and therefore get reflected on the different surfaces within the ice sheet's outer layer and enabling volume scattering to happen. The received waveform shape is thus modified by the volume scattered radiation's contribution.

As shown on the figure 3.6, the volume scattering contribution on the receiver continues to return power after the surface signal has reached its maximum. The mean elevation value can still be identified through the inflection point on the return waveform. The retracking post-processing can greatly improve the corrections for these phenomena.

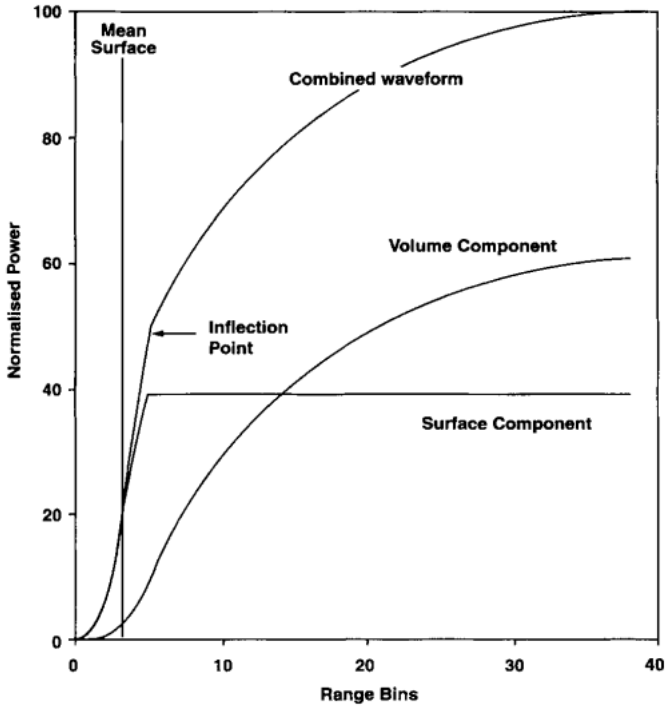

Figure 3.6: **Return echo from ice-snow surface microwave altimetry, the result of signal penetration on the snow-firn and volume scattering. [Credit: Cazenave & Fu 2001 [3]]**

According to a thorough analysis of this phenomena done by Patel et al. 2014 [23] the signal penetration of radar altimetry measurements is highly dependant on the characteristics of the physical conditions of the contact point on both the air-snow and snow-ice interfaces. In addition, factors like the snow accumulation and compaction rates are highly relevant and the use of the signal processing and error estimation can be reduced to the meter level. However, the study made by Remy et al. 2009 [24] found that the deviation caused by the signal penetration on the K_u band can amount to 12 meter in the interior of the ice sheets, while it is lower on the margins.

Surface Roughness

The backscattering coefficient, defined in the previous section, is related to the surface's reflectivity, characteristics and physical features, like the ones produced by the winds erosion, the sastrugi. In addition to this, the backscattering coefficient can also be related to the wind speeds on the surface of the ice sheets and at the same time these winds and other climatic parameters are closely related to the firn densification process. Unfortunately, a much more thorough analysis would be required to clarify these relations and as the focus of the project does not lie on it it will not be analysed in more detail in this section.

4

Satellite Altimetry Missions

The space earth observation era has come with a great variety of missions that make use of altimetry techniques. Throughout these decades altimetry measurements have changed the way we study the Earth, they have provided a systematic method to obtain altimetry data with a high temporal and spatial coverage. From the first satellite altimetry missions the accuracy of the range measurements has increased from the meter level to the centimetre level and further. One of the first attempts to use altimetry over the oceans was mounted on NASA's Skylab (1973-1979) and it produced data with a precision of around 15 meters. Later missions like SeaSat (NASA, 1978), GeoSat (NASA, 1985-1990), TOPEX/Poseidon (NASA, 1992-2006), ERS-1 &2 (ESA, 1991-2000 & 1995-2011) or ICESat (NASA, 2003-2010) achieved accuracies over ice sheets at the decimetre level, with ICESat providing 15 cm precise data with its laser altimeter. The biggest source of error on the first altimetry missions was originated at the poor accuracies of the orbit determinations that could rise up to 5 m.

Most of these missions have been aimed at the characterization of the ocean sea-level and are not optimized to measure over ice sheets. For an ice sheet specific mission the instruments need to be designed for measuring over the icy surface, where steep slopes, different surface reflection phenomena and rough surfaces make altimetry more complex than in the ocean surface. The coverage of polar areas is another issue as for studying the ice sheets the polar areas need to be covered. Thus, there have been few ice specific altimetry missions that make use high inclination orbits, the main ones being the ICESat, Envisat, CryoSat-2 and SARAL/Altika missions.

For this project the currently operational radar altimetry mission measurements are used, CryoSat-2 [25] and SARAL/Altika [26], and therefore an introduction to both missions is given in the following sections 4.2 and 4.1 respectively, where the relevant information on the altimetry performed by each of them is explained. The last section 4.3 includes a brief introduction of the ICESat mission as the source of the DEMs (Digital Elevation Model) used for validation purposes.

4.1. SARAL

SARAL stands for SAtellite for ARgos and ALtika, it is a joint mission by the CNES and the ISRO that aims for preciser sea surface height measurements with high temporal and spatial resolutions. The mission is designed as an inter-mission campaign to keep a continued long-term coverage of the oceanographic and topographic data from Envisat, lost in 2012, to the next Sentinel-3 mission planned to launch mid-2015. Therefore the SARAL mission shares characteristics with these other two missions.

The agreement between the CNES and the ISRO (Memorandum of Agreement) states the separated roles of each organization on the development and management of the mission. Thus, the CNES has been responsible of, for example, the development of the Altika and ARGOS-3 payload modules, as well as of the processing of the obtained data, while the ISRO takes care of the launch system, the ground control and the development of the spacecraft bus, the IMS-2 (Indian Mini-Satellite).

The Altika altimeter is the first satellite to operate on the K_a band at a 35.75 GHz frequency. The use of a high frequency radar improves the performance while reducing the antenna size and resolutions on both the height estimation and spatial resolutions. A drawback of using high frequency signals is the vulnerability of the signal to atmospheric phenomena like rain.

The Altika altimeter antenna is a fixed offset paraboloid antenna with a diameter of 1 meter oriented towards the nadir direction located at the top of the satellite as can be seen on figure 4.1. Just below stands the integrated payload module with the DORIS and the ARGOS L-band (1.7 GHz, 7.5 kbps) antenna. The Small Spacecraft Bus (SSB)/IMS-2 platform at the bottom part of the satellite is connected with the solar panels on both sides and the TTC (Telemetry, Tracking and Command) S-band and X-band antennas and the Argos UHF (Ultra High Frequency 465.98 MHz, 400 bps) transmitter are located on the side.

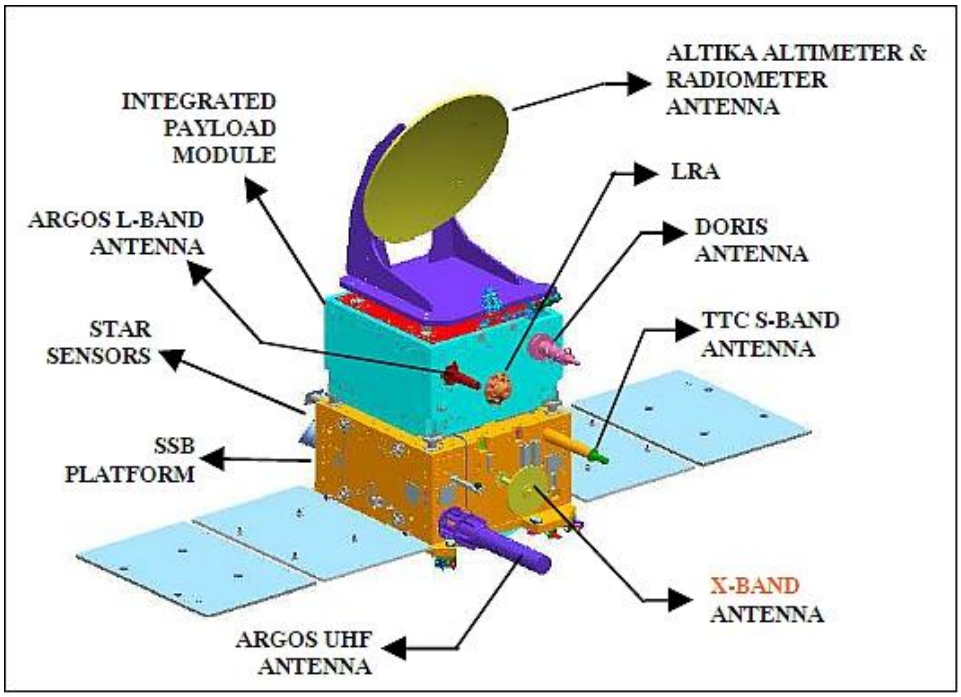

Figure 4.1: **The SARAL spacecraft, with the Altika and Argos instruments. [Credit: SARAL/Altika product handbook [4]]**

SARAL has a mass of 407 kg, with a payload mass of 147 kg. It has been designed to endure a 5 year operational lifetime with a possible extension to seven years.

4.1.1. The mission

The SARAL spacecraft was launched on the 25^{th} of February 2013 on the PSLV-C20 Indian launcher from Sriharikota, India. The satellite was injected into a sun-synchronous near-circular orbit at an altitude of 784 km with an inclination of 98.538°. This inclination lacks the coverage in high latitudes of the other more ice-oriented altimetry missions, however, for the specific focus of this project, the Greenland ice sheet, the coverage offered by SARAL is complete.

The orbit for the SARAL mission has been designed to follow the same path as the Envisat mission with a 1002 pass 35 day ground track repeat cycle orbit. With a perigee altitude of 784.0 km and a semi-major axis of 7162 km the orbital period of SARAL is of 100.5 minutes [27].

The mission goal of the SARAL/Altika is stated as:

"provide data products to oceanographic research user community in studies leading to improve our knowledge of the ocean meso-scale variability, thanks to the improvement in spatial and vertical resolution brought by SARAL/AltiKa"

In addition, SARAL/Altika has various secondary objectives, such as: the study of the continental water levels; the variability of the continental and sea ice masses; or the analysis and forecast of wave and wind fields on the planet's oceans.

Regarding the SARAL/ARGOS-3 subsystem of the satellite, the mission is aimed at contributing for the ARGOS system, which is aimed at the collection and localization of environmental data and the distribution of those to the users.

The ground segment of the SARAL mission is taken care of by both the ISRO and CNES; the ISRO manages the satellite control operations and the processing of the SARAL data for Indian users, while the CNES is responsible for supplying the processed near-real-time and delayed data products outside of India, the calculation of the DORIS provided precise orbits and the future CalVal proceedings.

4.1.2. Instrumentation

The satellite is mainly composed by two main instruments, the Altika altimeter and the ARGOS data acquisition system, along with many other elements to ensure the proper performance of the satellite. The instruments are described in the following paragraphs and can be found depicted in the figure above 4.1.

Altika

AltiKa (ALTImeter in KA band) is a 35.75 GHz K_a band altimeter, the first one to be employed on a satellite altimetry mission as K_u band altimeters 13.6 GHz frequencies. It has been developed in collaboration between the CNES and Thales Alenia Space-France. The instrument carries a dual radiometric capability to be able to quantify the atmospheric refraction effects that affect the precision of the range estimation as the wet tropospheric effect. In addition, the Altika design uses a wide band-width (500 MHz) which allows for an improved accuracy up to a factor of 3:1 (from 0.5 m to 0.3 m) compared to regular K_u band altimeters. Together with this, the use of a K_a band altimeter provides the possibility to avoid the incorporation extra elements to determine the ionospheric delay as the same antenna configuration can be used for the altimeter and radiometer.

The Altika altimeter uses the pulse limited measurement with a pulse repetition frequency (PRF) of 3800 Hz and length of 110 µs, twice as much as in the conventional K_u band altimeters, what allows for increased echo number for the same integration times.

The increased frequency also derives in a smaller signal beam-width and a smaller footprint on the ground, thus increasing the accuracy. Taking into account the altitude (784 km), the footprint of the

satellite is of 8 km, while a usual K_u band altimeter shows footprints around the 20 kilometres.

The radiometer on Altika is a total power radiometer, based on 2 radio frequency receivers, centred on the K_a 37 GHz ($\pm$ 500 MHZ) and K 23.8 GHz ($\pm$ 200 MHz) band frequencies. It is applied for estimating the wet tropospheric correction on the altimeter measurements. The radiometer calibration unit (RCU) The calibration is performed every few seconds and takes 200 ms to perform.

ARGOS-3

The ARGOS-3 instrument is part of the ARGOS (Advanced Research and Global Observation Satellite) data acquisition system that works as a collector, processor and transmitter of environmental data from worldwide located platforms.

DORIS

The Doppler Orbitography and Radiopositioning Integrated by Satellite technology allows the precise orbit determination of the satellite's orbit by measuring the Doppler shift of the frequencies the DORIS antenna receives from around 50 beacons located around the world. The orbit determination processing to obtain the POE is done once the data is downloaded to the ground, then to be made available to users.

Laser Retroreflectors (LRR)

The laser retro-reflector is planned as a support mechanism for the orbit determination of the DORIS system. The design allows for the return of the reflected light in the same direction that it contacted the reflector. It yields a RMS error below 6 mm.

AOCS

The attitude and orbit control system is composed by 4 reaction wheels that provide a 3-axis stabilization down to a 0.1° pointing accuracy and 2 magnetorquers aimed at momentum dumping through Earth's magnetic field. For the attitude determination capability 4 star trackers on-board provide a precision below 30×10^{-6} arcsecs in all axes. In addition to these, a 3 axis magnetometer contributes on the attitude determination process.

RF Communications

The SARAL payload data is transmitted trough a X-band communication, at a speed of 32 Mbit/s, while the TT&C data uses a S-band communication with an 4 kbit/s uplink speed. As for the ARGOS data, the collection of the data is done through an UHF link (465.98 MHz, 400 bps), while the transmission to the data centres a L-band (1.7 GHz, 7.5 kbps) is used.

4.2. CryoSat-2

Inheriting its role of monitoring the evolution of Earth's cryosphere from the earlier CryoSat mission that crashed on its launch in 2005 the CryoSat-2 mission was launched from Baikonur, Kazakhstan, in April 2010 by a Dnepr-1 rocket. The mission is developed under ESA's Living Planet Programme as part of its seven Earth Explorer missions aimed at improving the understanding of the Earth, the systems that form it and their processes. In this specific scenario, CryoSat-2 studies Earth's cryosphere by providing temporally and spatially continuous measurements focusing on the trends of the Greenland and Antarctic ice sheets and the marine Arctic sea ice variations. The proposer and lead investigator of the CryoSat-2 mission is Duncan J. Wingham, a professor at the University College of London and the chief of the Natural Environment Research Council (NERC).

Both CryoSat satellites have been constructed by EADS Astrium, while the main piece of instrumentation, the SIRAL radar altimeter, has been developed by Thales Alenia Space. The main difference between the two designs is the redundancy of the radar altimeter in the second mission, where two SIRAL instruments were included for safety reasons.

4.2.1. The mission

On the 8^{th} of April of 2010 CryoSat-2 was injected into a 92° inclination polar orbit. This has allowed for the study of the highest latitudes of the planet, as the mission has been able to provide data on 96% of the Antarctic continent, only leaving a region of 215 km radius around the pole uncovered. This coverage is the highest ever provided by a satellite remote sensing study of the Polar regions.

With its perigee at an altitude of 719.3 km and the semi-major axis at 7096.65 km the orbit of CryoSat-2 is slightly eccentric, 0.0088, and has a period of 99.15 minutes, NORAD 15 July 2014 [28]. The injection of CryoSat-2 into orbit by the Dnepr rocket was not performed as planned, as the injection orbit was intended to be a frozen orbit, where the eccentricity would not vary due to Earth's shape [29]. CryoSat's thrusters were used to correct for the error, however the final orbit is not the one originally planned, causing some performance problems.

Using the precession of the right ascension of the ascending node (RAAN), due to the mass distribution variations on the Earth (J_2 effect) and other non-radial perturbations, the orbit has been designed to repeat every 369 day cycle, which corresponds to 5344 orbits, with a 30 day complete Earth coverage sub-cycle, C. Goetz 2007 [30].

The mission was initially planned for a duration of 3 years, until 2014, however the good health status and the growing interest of the scientific community on the data provided by the mission will most probably allow for its operational life to be extended, however this has not yet been officially confirmed, Parrinello 2014 [31]. Currently, CryoSat-2 is the only satellite that is uniquely focused at monitoring Earth's cryosphere and a follow-on mission, ICESat-2 by NASA, is expected to be ready by the end of 2015 to take its place.

4.2.2. Instrumentation

The design of CryoSat-2 closely imitates the design of its predecessor CryoSat, which shared the same goals and similar constrains. The main difference between the two is the addition of a second SIRAL instrument for the design of the CryoSat-2 for redundancy, increasing the estimated success probability.

The main payload components of CryoSat-2 are the two SIRAL altimeters, the DORIS receiver, the three star-trackers and a set of retro-reflectors for the SLR. The set-up of the satellite is depicted in figure 4.2. The satellite has no moving body parts, no deployable solar panels; these are body-mounted (upper part). The two-front antennas are the SIRAL altimeters that are set perpendicular to the direction of motion. The DORIS receiver is located in the nadir panel, together with TT&C and data downlink S and X-band antennas and the laser retro-reflectors. The three star trackers are oriented towards the satellite's zenith on the frontal part of its structure.

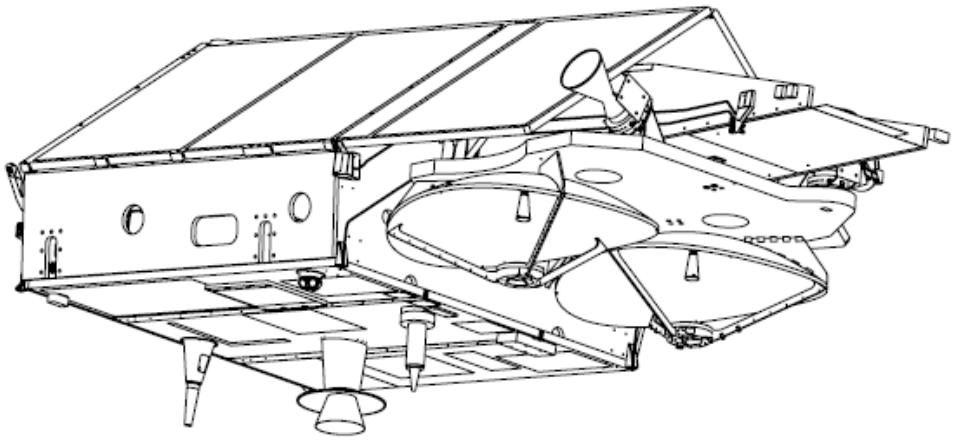

Figure 4.2: **CryoSat-2 set-up. [Credit: Wingham et al. 2006 [5]]**

SIRAL-2

The SAR Interferometric Radar Altimeter represents the state-of-the-art of the radar altimetry technology enhanced for the characterization of the icy surfaces. Built by Thales Alenia Space, it is the main payload of the CryoSat-2 mission. The innovative design of SIRAL is based on its two antennas placed on the cross-track direction that enable the high resolution interferometric measurements for the high slope variations on the coastal regions of the ice sheets.

The 70 kg mass instrument uses a power budget of 149 W and has three operational modes, the Low-Resolution mode (LRM), the Synthetic Aperture Radar mode (SARM) and the SAR Interferometric mode (SARInM). It uses carrier frequency on the Ku-band at 13.575 GHz and a bandwidth of 350 (320) MHz.

LRM (Low Resolution Mode) The Low-Resolution mode of the SIRAL radar altimeter uses the conventional pulse limited measurement mode. It is selected to measure the height variations of the continental ice sheets and ocean surfaces as the surface topography is generally homogeneous within the footprint.

On this mode a pulse repetition frequency (PRF) of 1.971 KHz with a 49 μs long 320 MHz bandwidth chirps are transmitted. The echoes reflected on the surface return after almost 5 ms and the return power and shape are processed through a single receiver channel to form the measurement products. As explained in 3.1 the return waveform's shape and the power distribution define the characteristics of the surface features as well as the topography of the area.

SARM (Synthetic Aperture Radar Mode) The SAR mode is used for measuring over regions that require a high along-track resolution as on sea ice. The motion of the radar emission itself creates the 'synthetic' aperture effect on the radar altimetry. Like the LRM it uses a single receiver channel but the PRF is 10 times higher than the LRM one, 18.2 kHz, and they are emitted in bursts of 64 pulses. The burst's length is of 3.6 ms and there is an interval of 11.7 ms (BRF 85.7 Hz) in-between successive bursts, what allows the burst to go through the receive chain before the next is emitted.

The characterization of the Doppler shift profiles on the received echoes, which are divided in 64 sub-beams, allows for a finer characterization of the footprint returns. The analysis of these smaller footprint returns provides a 250 meter along-track resolution for the SARM, while the cross-track is 15 km. This represents a significant step forward on the spatial resolution of the monitoring of the sea-level variability on the oceans.

SARInM (SAR Interferometric Mode) The SAR Interferometric mode is aimed at improving the cross-track resolution by using a second receive channel for characterizing the marine ice sheets on the coastal part of the GrIS and AIS as these regions tend to show high altitude variations. It is also used for measuring over lower latitude glaciers as these also have high height variations.

For the SARInM both channels use a similar SARM setting (with a BRF of 21.4 KHz) while at the same time the interferometric capabilities allow for the localization of the independent bursts by comparing the phase differences on both antenna channels.

CryoSat-2 carried the DORIS and LRA precise orbit determination instruments as SARAL does, a description can be found on the instrumentation section of the SARAL satellite 4.1.2.

RF Communications

The communication payload allows for a 2 kbit/s uplink and 8 kbit/s downlinks connections on the S-band for TT&C purposes. On the X-band, the downlink speed allows for the transfer of the vast amounts of data of the SIRAL altimeter with a 100 Mbit/s downlink connection with the Kiruna ground station , C. Goetz 2007 [30].

The mission control is located at the ESA's satellite operations centre in Darmstadt, Germany, and during the data downlink of 10-11 minutes per day an amount of 50 GB is downloaded to the ground station at Kiruna, Sweden.

AOCS

The attitude control system encompasses attitude determination, control and stability elements that must ensure that the requirements of below 10 arcsec per axis accuracy (for the SARIn mode) are met. The star trackers provide attitude determination below 3.2 arcsec for lateral axes and below 16 arcsec for the roll axis. A set of 16 attitude control and 4 orbit control nitrogen cold gas thrusters, with 10 mN and 40 mN thrust, are included to perform attitude corrections. The three magnetotorquers ensure that the attitude stability is guaranteed in the event of perturbations.

The satellite flies in a "nose-down" manner, with its nadir being tilted by 6° with respect to the vertical z axis, this enables it to minimize the attitude corrections required due to gravity-gradient disturbances.

4.3. ICESat

The Ice, Cloud, and land Elevation Satellite developed under NASA's Earth Observing System was a satellite altimetry mission aimed at the study of the Earth's cryosphere as well as other surface and atmospheric characteristics of the planet. Initially designed for a period between three and five years, during its seven years of operation it was able to produce one of the most complete and accurate records of satellite altimetric data to date.

Launched in 2003 on a Delta-2 rocket into a near-polar orbit (inclination 94°) at an altitude of 600 km and ground-track repeat period of 91 days to allow for a uniform sampling of the Earth surface with a high resolution. It had the main goal to monitor the evolution of the Earth's polar ice sheets and quantify its contribution to the global sea level change. As second level objectives the satellite was also equipped with the capability to study aerosols and clouds on the atmosphere and surface features on the planet surface, like snow-cover, reflectivity or vegetation height.

The ICESat mission used a laser altimetry technique for its main instrument, GLAS (Geoscience Laser Altimeter System), which makes use of infrared (1064 nm) and visible green (532 nm) light pulses of 4 ns. The infrared light is used for topography, while the green is applied on the study of the atmosphere. The use of laser altimetry allows for a reduced footprint on the ground 60 meter, increasing the accuracy of the received waveform and thus the range estimations.

On October 2009 the laser altimeter GLAS instrument failed and after attempts to bring the satellite back to operation the mission was retired on 2010. A follow-on mission, ICESat-2, is under development to continue working on the monitoring of the Earth's cryosphere, it will carry the improved laser altimetry instrument ATLAS (Advanced Topographic Laser Altimeter System) and it is expected to be launched in 2017, Abdalati et al. 2010 [32].

Within the scope of this project the ICESat data has been used for processing and validation purposes. The DEMs produced from the ICESat mission as provided by DiMarzio et al. 2007 [22] have been used as a reference for the accuracy of the estimations computed from the other satellite data.

5

Data & Software Resources

This chapter presents the data resources and the main software tools employed for the development of this project. Each of these elements correspond to specific goals in the data processing chain, as well as to specific development phases of the thesis. This introduction includes the description of the main data types, formats and sources 5.1 and the used hardware and software platform set-ups 5.2.

5.1. Data

The data that has been involved in the development of this project can be classified in two main groups: the satellite data (on their processed or ESA provided form) and the scientific data used alongside with the satellite data for processing, correction or validation purposes.

The format in which the data is stored, generally, follows similar patterns. A quite extended file format for satellite and scientific data is the NetCDF. The NetCDF is self-describing file format, for which it includes a header that gives the layout and other details to the reader.

In the case of ESA provided datasets, the data products are presented in two files: a header file (.HDR) that includes all the basic layout and format information and a binary data block file (.DBL), which includes the raw satellite data structured as described in the .HDR header file.

5.1.1. Satellite Data

This project focuses on the altimetry missions that provide current data on the topography of the Earth's cryosphere, more specifically the GrIS. The missions with the necessary coverage are ESA's Earth observation mission CryoSat-2 and the CNES's Altika instrument on-board of SARAL. Both missions have been introduced on the related chapter 4.

The satellite data are made available in various levels of processing by the institutions that handle them. The level 0 represents the raw satellite data received at the data centres, while the level 1 and level 2 data sets are processed up to different levels. In the case of SIRAL-2 and Altika data the fitting of the waveform curves and the determination of the range measurement is done in between the level 1 and 2 processing.

The central element of this project is the range measurement once it is estimated from the fitting of the waveforms and therefore the focus is put into level two and higher. The range data are provided together with the scientific data required to apply the corrections in different forms.

The RADS database for which the section 5.2.1 explains the main processing tools contains a post-processed version of the above mentioned datasets in NetCDF format for various satellite missions. The data is regularly updated for the ongoing missions.

5.1.2. Scientific Data

The scientific data serves various purposes: applying corrections on the satellite data; validation or as an input on a processing routine.

In order to properly model some phenomena that produce deviations on the satellite measurements extra scientific data about the state and dynamics of the contacted medium are required. For example, on the first steps of the satellite data processing the altimetry range measurements are corrected for the effects that various atmospheric and earth geophysics phenomena have on the data. Generally, the data for this purpose is provided alongside the range measurements on the higher level distributions of the data.

Other reliable sources of scientific data to build the correction or validation models are the scientific institutes or the peer-reviewed work done by other researchers.

In the calculation the slope correction for the range measurements an estimation for the slope of the reviewed surface is required. In order to determine this a Digital Elevation Model *DEM* is used, the methodology is explained in chapter 6. The DEM has been developed by DiMarzio et al. 2007 [22] using the ICESat/GLAS laser altimetry campaigns. The data contains the thickness of the GrIS for each cell on the grid that uses a stereographic projection, which in this case is in stored in binary format. The same DEM has also been used with validation purposes for initial GrIS thickness estimations, which were compared to the DEM.

5.2. Platform & Software

The platform used to handle these is composed by a 64-bit LINUX running (Ubuntu 14.10) OS personal computer with access to a server provided by the Delft University of Technology to the Delft Institute for Earth-Oriented Space Research to store and work with the Radar Altimeter Database System (RADS), where the university's radar altimetry datasets and utilities are made available.

This thesis project has been developed using several software tools in coordination to produce the final results in step-by-step scheme in which different pieces of software had specific tasks and goals. The software employed on this project has both been obtained from external sources (scientific institutions or experts) or has been developed for the specific purpose of this project. Data processing and visualization tools like *MATLAB* or *GMT* have been used along with *RADS*. In addition a considerable part of the processing chain includes newly produced processing tools that have centred a great part of this project's effort. These have been written using C++ language and have been compiled using a g++ compiler delivered under the GNU compiler collection by the Free Software Foundation. The most relevant parts of these pieces of code can be found on the appendix B. On the next paragraphs an overview of the core software used on this project is introduced.

5.2.1. RADS

The **Radar Altimetry Database System (RADS)** [33], developed by the Delft Institute for Earth-oriented Space Research in cooperation with the NOAA Laboratory for Satellite Altimetry, is a satellite database that gathers Earth observation altimetry measurements done during the last decades in several Earth observation missions. Together with these, RADS offer tools for the reading, editing and processing of the data and although RADS was originally designed for ocean applications on this project it has been used for ice.

The RADS library includes data from several satellite missions, most of them aimed at characterizing and monitoring the evolution of the Earth's oceans, but some of them do also include some coverage of the Earth's ice sheets. In the following table the satellite altimetry mission data available in the RADS database are listed with the period in which the have been operative, the number of modes in which these data were collected and the number of cycles (the operative satellites get regular data updates to date).

Satellite/Instrument	Abbreviation	Years	Phases	cycles	Agency
Geosat	gs	1985-1990	4	93	NASA
ERS-1	e1	1991-2000	7	156	ESA
TOPEX	tx	1992-2006	2	444	NASA
Poseidon	pn	1992-2006	1	68	CNES
ERS-2	e2	1995-2003	1	170	ESA
GFO	g1	1998-2008	1	180	NASA
Jason-1	j1	2001-2013	3	425	NASA/CNES
Envisat	n1	2002-2012	2	113	ESA
Jason-2	j2	2008-	1	241	NASA/CNES/NOAA
CryoSat-2	c2	2010-	1	59	ESA
SARAL/Altika	sa	2013-	1	20	CNES/ISRO

Table 1. Satellite data on RADS database.

The RADS dataset makes use of NetCDF files to store the satellite data obtained from the ESA data files. These files contain up to 50 different data fields for each measurement that give information on every relevant aspect of the measurement's characteristics; measured magnitudes like range or

backscatter; geophysical conditions in the atmosphere and derived corrections; satellite's orbital information or statistical information.

The RADS dataset is organized in folders for every cycle of each satellite mission mode. On each satellite cycle all the pass files pertaining to the cycle are included and carry a specific name in agreement with this format that states the file's main characteristics: satellite mission, pass number and cycle number. As an example, the CryoSat-2 satellite pass number 91 on the 13^{th} cycle is called "c2p0091c013.nc". Odd pass numbers correspond to ascending passes, while descending passes have even numbers.

The **utilities** made available with RADS enable the user to create personal selections from the database with a wide range of possibilities and conditions.

The *"rads2asc"* utility selects and prints the desired data from the user specified satellite mission, cycle, pass and magnitudes, giving the chance to print it to a file in columns.

The *"rads2grd"* tool creates a grid from the user specified data in a similar way as in the *"rads2asc"* utility.

The *"radscolin"* utility creates collinear track selection from single-satellite or multiple-satellite datasets. While the tool *"max2"* creates crossover points from all the crossing passes. The physical reasoning behind this two tools will be introduced in chapter 7.1.

Using *namelists* the user can define its preference to a greater accuracy as this files allow the declaration of constant parameters and the setting of limits on the variables. This way the data from a specific region of the planet or a specific time period can be isolated.

5.2.2. GMT

The Generic Mapping Tool (GMT) is a collection of tools for the manipulation and processing of the satellite and scientific data sets and the creation of postscript visualization images. On both tasks GMT offers a wide range of possibilities and a high degree of customizability for the users.

Developed by Wessel et al. in 1991 [34] and supported by the National Science Foundation, GMT represents one of the finest tools for researchers working on the Earth observation field and is distributed freely under GNU licenses. For this thesis project the latest version to date, version 5.1.1 has been employed.

Some of the data handling tasks performed by GMT include from simple operations with data set columns to the fitting of curves and surfaces or the gridding. It provides most of the processing routines required for the analysis, comparison and visualization of Earth observation data.

The main capability of GMT is its visualization tool. It offers an amount of plotting possibilities (projections, plot settings, text notes, colour palettes, customizable graphics) with libraries that include geographical information. This enables the quick and simple inclusion of shorelines, borders, rivers or other geophysical elements of the Earth together with the scientific data. In addition it also provides processing options like statistical or gridding utilities.

The GMT has been a key tool for the processing, analysis, comparison, visualization and validation on this project, being its capabilities very relevant in various processing phases of the project, validation by DEM comparison or satellite ground-track slope determination being good examples. All the graphical outputs on this project have been produced using GMT and the applied scripts are presented on appendix A.

5.2.3. C++ language, GNU g++ compiler

As mentioned at the beginning of this chapter, C++ coding has been used in order to design and perform some of the main processing phases of the project.

These pieces of code generally aim specific data processing goals throughout the project, on the following chapters more detailed references to these and their main characteristics can be found. Some of the relevant parts can be found on the Appendix B.

5.2.4. Other

Some other software tools have been employed on the specific phases of the project for several objectives, however their relevance is more limited due to their academic purpose or the specific problems they were oriented towards.

The **Basic Radar Altimetry Toolbox (BRAT)** [35] enables the users to access and scroll through the contents of the ESA provide satellite data files (.DBL and .HDR) with a simple GUI. It also allows making simple operations with the different data fields that the files contain, it includes as well, a basic visualization tool. This has been used in specific scenarios to validate the work done with RADS or to initially get familiar with ESA's data formats and their content.

The **MATLAB**™ environment has been used in some specific scenarios where useful previously written code was available for relevant purposes for the project, it has also been applied in matrix calculations in certain phases. In some other cases it has also been used for testing and validation purposes. The code has been included on appendix C.

While manipulating NetCDF files, Unidata [36], the use of standard NetCDF tools has proven useful to on specific moments access the content of the files and progress on the understanding and processing of the data. Some of these tools are the **ncdump**, **nco** or **ncBrowse** utilities.

6

Greenland Ice Sheet Thickness Calculation

The first step in the characterization of the evolution of a physical system is to be able to define the state of the system on a specific moment or short time-period. Therefore, with the final goal of estimating elevation changes, on this first chapter the process towards the determination of the thickness of the GrIS is explained.

On the next sections the method used and the details regarding the computation of the GrIS thickness, on 6.1, and the corrections applied on the range measurements, on 6.3, are described. In addition, a validation method is presented that uses an independent DEM to evaluate the accuracy of the thickness estimation, 6.2. To finish, the resulting thickness estimation and its difference with the DEM are included on section 6.4.

6.1. Initial thickness calculations with RADS

The satellite data, as explained in section 5.1, is a set of individual measurements organized in passes (ascending and descending half orbits) that are part of cycles. The cycles are defined by the fixed amount of time after which the satellite's orbit repeats the same path on the ground. Therefore, the individual element selected to characterize the momentary state of the GrIS is **one orbit repeat cycle**.

In the case of the CryoSat-2 mission the orbit repeat cycle is of 369 days, however the orbit was designed to hold an orbit sub-cycle of 30 days that provides sufficient Earth coverage Goetz et al. 2007 [30]. In the case of SARAL/Altika the orbit repeat cycle is of 35 days.

The data used on this phase has been obtained from the RADS database using the *'rads2asc'* utility to structure the data into a columned file. The data fields extracted to build the thickness profile are the following:

1. latitude [degrees north]
2. longitude [degrees east]
3. GDR-D orbital altitude [m]
4. K_u / K_a-band range corrected for instrument effects [m]
5. ECMWF dry tropospheric correction [m]

6. radiometer wet tropospheric correction [m]
7. JPL GIM ionospheric correction [m]
8. solid earth tide [m]
9. GOT4.8 load tide [m]
10. EGM96 geoid height [m]
11. K_u/K_a-band backscatter coefficient [dB]

This data is able to build **range** values that are corrected for the main altimetry errors. The corrected pseudo-range value can be obtained by adding the **atmospheric correction** values to the K_u / K_a:

$$r = r_0 + \Delta r_{dry\ tropo.} + \Delta r_{wet\ tropo.} + \Delta r_{ion} \tag{6.1}$$

r being the corrected range values; r_0 the instrument effect corrected range; and the Δr are the atmospheric corrections.

When the effect of the Earth's variations on the **geoid's shape** are considered the following **correction** need to be applied.

$$r_{corrected} = r_0 + \Delta r_{atm} + \Delta r_{geoid\ height} + \Delta r_{solid\ earth} + \Delta r_{load\ tide} + \Delta r_{geoid\ tide} \tag{6.2}$$

And from this range value the elevation of the ice sheet over the geoid can be estimated.

$$H_{GrIS} = r_{orbit\ alt.} - r_{corrected} \tag{6.3}$$

where H_{GrIS} is the elevation of the ice sheet.

Using these relations a preliminary calculation of the height profiles can be done. In order to do this, a script has been designed, it can be found on the appendix A.1. In first place, the script makes use of the *awk* command to handle the columns and prepare the proper column setting for the later processing using *GMT* tools. With the columned data, a *blockmean* command is applied in order to write into a standard output the arbitrarily located data using a mean position and value for every $0.1°$x$0.1°$ cell. With this new setting a *nearneighbor* function is applied to the data to create a two dimensional grid that is then used to plot the data. The different parts in this plotting script have been used over the project to produce the visual side of the results using several settings and values for the parameters.

The following figure 6.1 gives a good impression of the capability of this simple scheme.

In the case of CryoSat-2 6.2, only the LRM data are available in the RADS database and therefore the result is limited to the shallower inner parts of the GrIS.

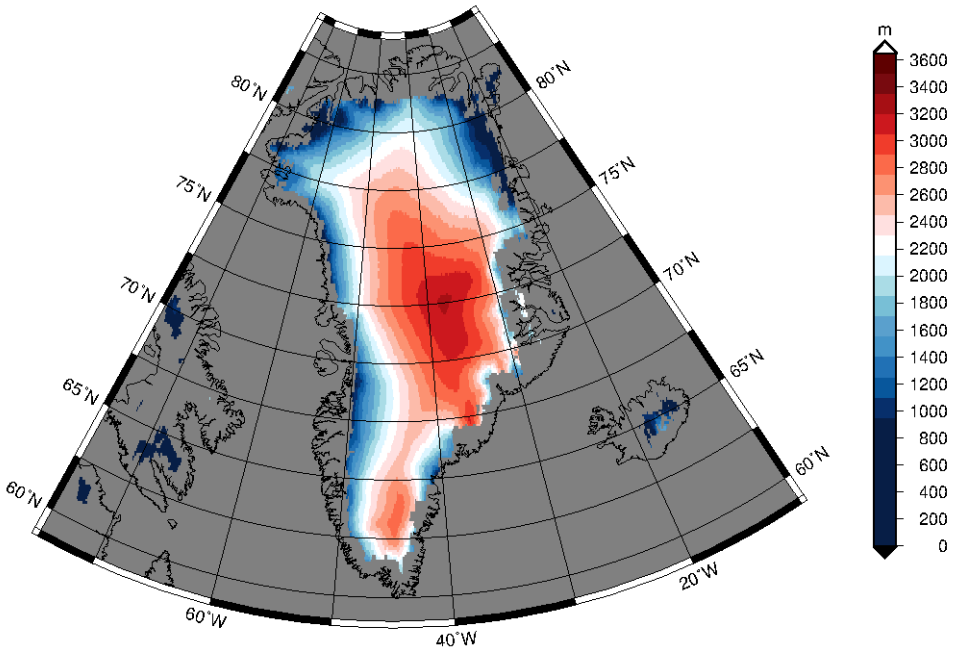

Figure 6.1: **GrIS height from SARAL/Altika data.**

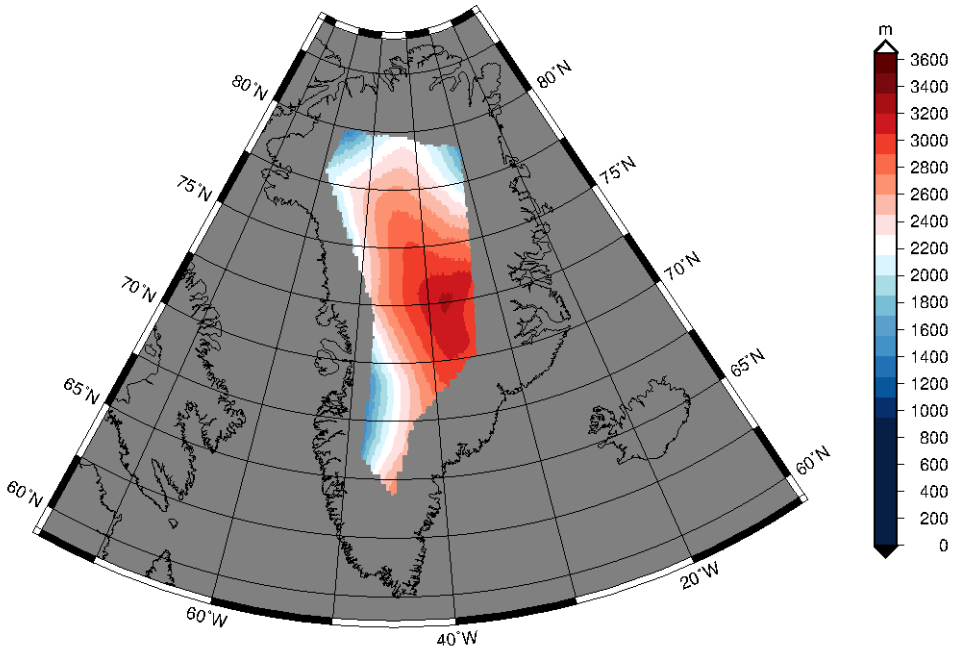

Figure 6.2: **GrIS height from CryoSat-2/SIRAL LRM data.**

Another interesting output obtained from the data, that serves as a validation of the expected behaviour of the satellite data, is the significant difference between the icy and the ocean surfaces on their backscatter coefficient (σ_0). On the next figure 6.3 the clear difference between the surface types can be observed, although the surface of the more steep edges of the GrIS show lower values for the σ_0. This difference on the coastal margins is expectable due to the increased surface inhomogeneities in these regions, with causes like topographical irregularities or higher dust and rock presence.

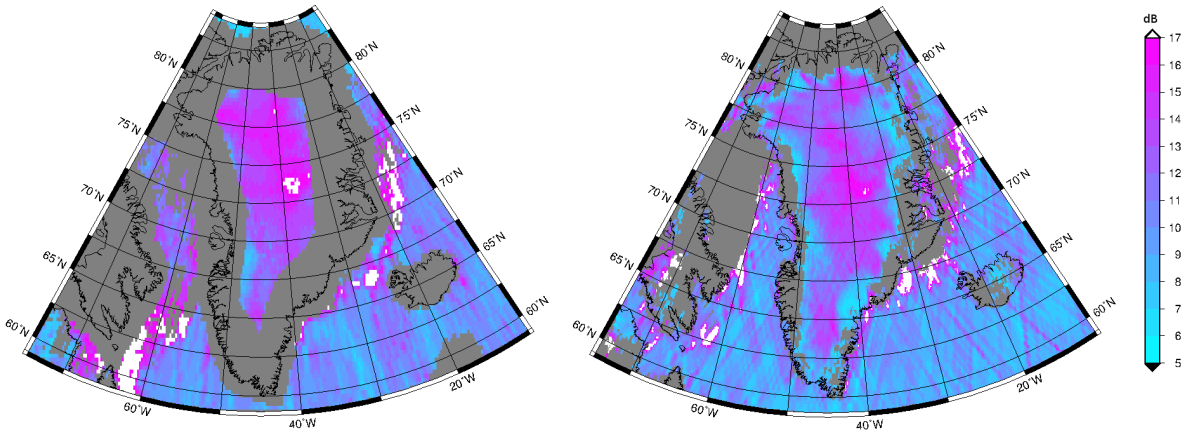

Figure 6.3: **GrIS signal return backscatter coefficient from SIRAL LRM (left) and Altika (right) data.**

6.2. DEM Validation

In order to keep track of the accuracy of the data, a method for validating the obtained results is set-up based on the comparison with a reliable source **Digital Elevation Model (DEM)**. The DEMs are generally publicly released and there is access to a great variety of spatial resolutions, sources and formats. Each DEM has specific characteristics and accuracies and the differences with the satellite data are relevant to explain the observed differences.

For this project the GLAS/ICESat laser altimetry DEM has been chosen. It is released by NSIDC and it was developed by DiMarzio et al. 2007 [22]. It is built using the first seven operational periods of the GLAS instrument (February 2003 and June 2005). The DEM is provided in a binary file that contains the data grid of 1x1 km^2 cells, the information related to the grid is given on a separate header file. The data on the DEM is structured in a polar stereographic projection [37] and the elevations are given relative to the EGM96 ellipsoid [38]. Due to the fact that the CryoSat-2 data available in the RADS library is referenced to the EGM2008 geoid, it requires a specific DEM that fulfils this condition. However, we have been unable to find a publicly available one. With this, added to lack of CryoSat-2 LRM data on the whole GrIS (the processing of the SARInM data has been considered out-of-reach for the time and effort constraints of this thesis project), the conclusion that the project has to continue solely with SARAL/Altika data has been reached.

The extraction and reading tasks with the DEM have been done using newly written *MATLAB* routines, C.2, while for the conversion of the DEM's projection into latitude and longitude coordinates a *MATLAB* script provided by the NSIDC on its website has been employed. From the processing of the binary DEM file, a columned file listing the location and thickness data is produced as an output.

The comparison between the results obtained from the satellite data and the DEM is given by the next equation and it is plotted in the following figure for the SARAL/Altika mission 6.4.

$$\Delta H = H_{Satellite} - H_{DEM} \tag{6.4}$$

By applying the same *nearneighbor* function, as in the satellite data, to the DEM height values to create a grid file. Then using the GMT mathematical commands the subtraction of one grid with another one is done.

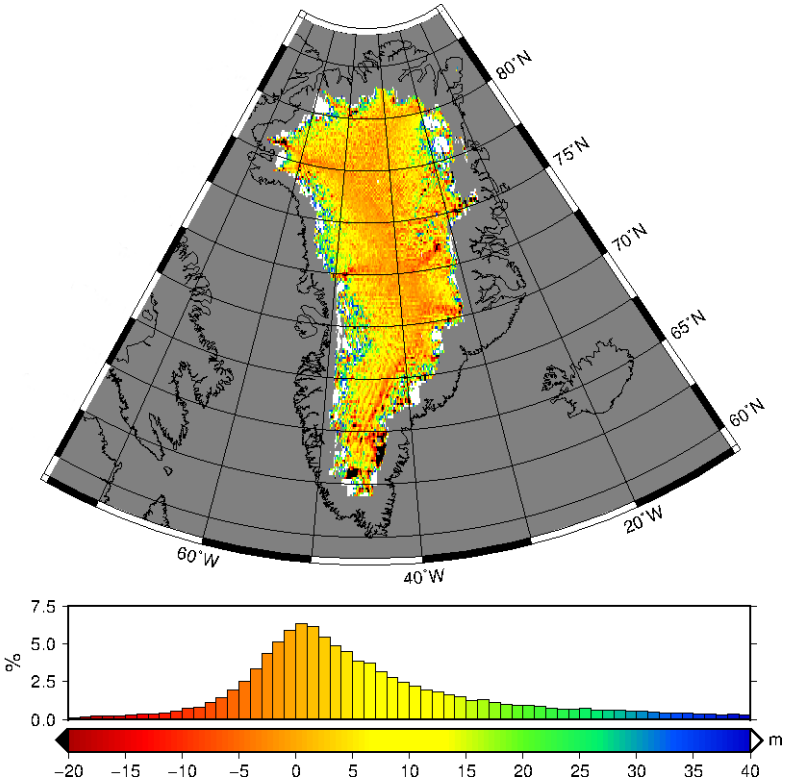

Figure 6.4: **Comparison of satellite thickness estimates and the DEM. Using SARAL/Altika mission data.**

Figure 6.4 shows the result, that for most of the area falls within the ≈ 10 meter error. This is expected as on this data some corrections, like the slope correction and thus the higher error on the edges, have not yet been applied, these will be explained on the next section.

Using this DEM comparison, a validation channel has been established for the GrIS thickness estimates that will be used all along the project. It must also be mentioned that although it is of great help, the main interest and objective of this project is not centred at the precise estimation of the elevation profile of Greenland's ice sheet but at measuring its variation over a certain period. Therefore, non-varying errors will be erased on the temporal comparison and only the evolution signals will remain.

6.3. Corrections

The corrections applied on the range measurements have been obtained from the RADS database at the same time as the range measurements. The following table 6.5 lists the main error sources on altimetry measurements and makes an estimation of the effective value of these errors on the cryospheric measurements.

Correction	Source	Typical winter magnitude at 80°N, averaged over 1 month and 10^4 km^2.	Reference
Ocean tide	FES 02	0.03 m	Le Provost et al. (1998)
Ocean loading tide	FES 02	0.002 m	Francis and Mazzega (1990)
Long-period tide	FES 02	0.0075 m	Le Provost et al. (1998)
Solid Earth	Cartwright Edden	0.015 m	Cartwright and Edden (1973)
Polar tide	Wahr	0.0025 m	Wahr, 1985
Dry troposphere	Meteo France/ECMWF	2.3 m ±0.02 m	Saastamoinen, 1972
Inverse barometric correction	Meteo France/ECMWF	0.03 m	Ponte (1991)
Wet troposphere	Meteo France/ECMWF	0.01 m	Saastamoinen (1972)
Ionosphere	Bent model	0.015 m	Llewwllyn and Bent (1973)

Figure 6.5: **The source and reference value of the corrections applied on altimetry measurements. [Credit: Wingham et al. 2006 [5]]**

These errors are all related to the deviations caused by the atmosphere or the geoid's height variations. However, the errors caused by the measurements on ice sheets have not been taken into account for these phase measurements. As explained on section 3.1.2, the main sources of error are the following.

Correction	Estimated value	Reference
Slope induced (along- and across-track)	10 - 80 m	Brenner et al. 2007 [39]
Signal Penetration & Volume scattering correction	≈12 m (interior) & 1 m (edge)	Remy et al. 2009 [24]

Table 2. Ice sheet specific altimetry error corrections.

Due to its relevance and the time constrains the estimation and correction of the along- and across-track errors has been calculated. As for the combined effect that the signal penetration and the volume scattering have on the shape of the waveforms and the deviations that these cause on the overall range computations, the correction of these has been left out of this project's consideration as the processing of the received waveforms falls out of its scope.

6.3.1. Dry & Wet Tropospheric Correction

Due to unknown causes the RADS database does not include the calculation of the dry and wet tropospheric corrections over the icy surfaces of Greenland for the SARAL/Altika mission.

Therefore the correction for these atmospheric refraction is computed using surface-level pressure models and the Saastamoinen model to calculate the deviations. The routines used for the computation of the tropospheric deviation profiles have been provided by E.J.O. Schrama.

In these routines the delay along the path length of the signal is integrated using the following relation from the book *Understanding GPS: Principles and Applications* by E. Kaplan and C. Hegarty 2005 [40],

$$\Delta S_{tropo} = \int_{Sat}^{Nadir\ point} N\ ds \tag{6.5}$$

where $N \equiv 10^6(n-1)$ represents the refractivity and s the path along which the signal travels.

The values of the refractivity are given by the following relations for the dry and wet tropospheric effects at sea level,

$$N_{d,0} \approx a_1 \frac{p_0}{T_0} \tag{6.6}$$

$$N_{w,0} \approx a_2 \frac{e_0}{T_0} + a_3 \frac{e_0}{T_0^2} \tag{6.7}$$

where the a parameters are empirical constants that can be found on the referenced book, p_0 the partial pressure (*mbar*) and T_0 (*K*) the temperature at the sea level.

As the refractivity is also affected by the height, the following relations are used. For the dry tropospheric component:

$$N_d(h) = N_{d,0}[\frac{h_d - h}{h_d}]^{\mu} \tag{6.8}$$

$$h_d = 0.011385\frac{p_0}{N_{d,0}x10^{-6}} \tag{6.9}$$

with a $\mu = 4$ value from the ideal gas relation, while for the wet component:

$$N_w(h) = N_{w,0}[\frac{h_w - h}{h_w}]^{\mu} \tag{6.10}$$

$$h_w = 0.0113851\frac{1}{N_{w,0}x10^{-6}}[\frac{1.255}{T_0} + 0.05]e_0 \tag{6.11}$$

The temperature and pressure atmospheric conditions at the sea level are obtained from atmospheric models and passed into the equations to compute the tropospheric corrections.

On the following figure the conjunct effect of the dry and wet tropospheric corrections applied on the GrIS are geographically shown. As expected the refraction is reduced as the height on the GrIS is increased due to the lower density and pressure at these altitudes as well as due to the shorter travel distance for the radiation.

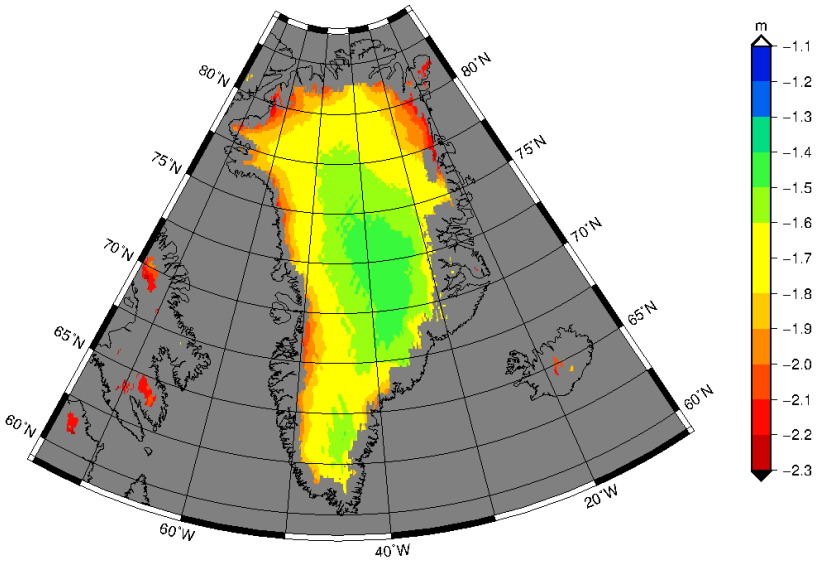

Figure 6.6: **The dry and wet tropospheric corrections on the GrIS.**

As a **validation** test the dry and wet tropospheric corrections are compared to the RADS provided ones for the sea regions, as these are available on RADS and the new calculation. The following figure 6.7 displays the difference between these two estimations. The difference in both is close to 0 for the sea surface areas. However, the wet tropospheric correction by the RADS database for the sea regions close to the GrIS and northern latitudes shows higher values. This is explained by the fact that the model used in RADS does not take into account the existence of sea-ice and therefore the reduction of the water vapour causes a reduction on the wet tropospheric effect.

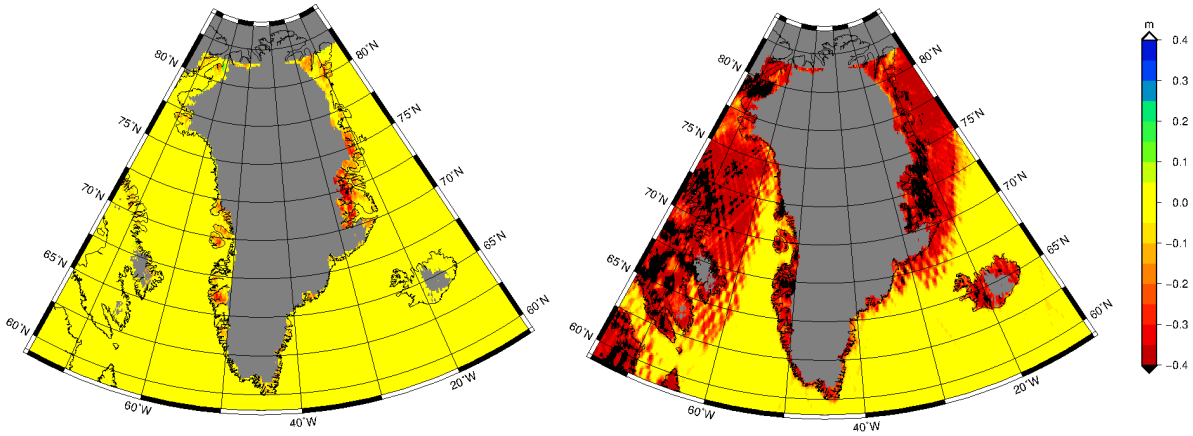

Figure 6.7: **The difference on the dry (left) and wet (right) tropospheric corrections for sea regions between the RADS and the software estimated value.**

6.3.2. Slope Correction

The correction of the slope-induced error is a major issue in the accurate characterization of the ice sheets. As explained in section 3.1.2 the displacement caused by the non-perpendicular surface on the nadir direction is given by a simple geometrical relation

$$H = \frac{H_m}{\cos\alpha} \tag{6.12}$$

$$\Delta H = H(1 - \cos\alpha) \approx H\alpha^2/2 \tag{6.13}$$

As introduced in 3.3 α represents the angle relative to the vector normal to the reference ellipsoid.

In first place, due to the lack of information about the processing that the satellite data has gone through the data available in RADS database is tested to check whether the satellite track has already been corrected for the deviation caused by the first contact point's wrong location.

For this goal an 8^{th} degree polynomial is fitted to the satellite track coordinates and the error of the observed data over the ice sheet and the oceans is used to draw a conclusion on the existence of such a processing. On this test the data corresponding to the 8^{th} cycle and pass #3 of the Altika mission are used, a track that starts over the Atlantic ocean then crosses the GrIS to go into the Arctic ocean. The fitting is done using *MATLAB's polyfit()* utility, that allows the curve fitting of a n^{th} degree polynomial to the data, on the normalized latitude and longitude values.

The fitting produces 9 coefficients and this fitting is then compared to the observed latitude points, producing the following errors, figure 6.8. The resulting errors have a normalized error of the order of $2\text{x}10^{-5}$, where the non-normalized ($1 \approx 15°$) error corresponds to $3\text{x}10^{-4}$. This error magnitudes at the ground-track represent a deviation of around 30 meters what is a low value when compared to the precision of the track coordinates that have a footprint of 8 km. It is orders of magnitude below the precision of the measurement location and a first contact point correction would give rise to a much greater deviations. In addition, the fitting shows a smooth pattern, opposed to the ocean-ice sheet and ice sheet-ocean crossings that happen on the data, what supports the idea of a raw satellite orbit coordinates as the surface slope variations on the coastal margins of the ice sheet would create more irregular patterns on the crossings. So, in conclusion, the correction of slope-induced deviations has not been applied to the coordinates.

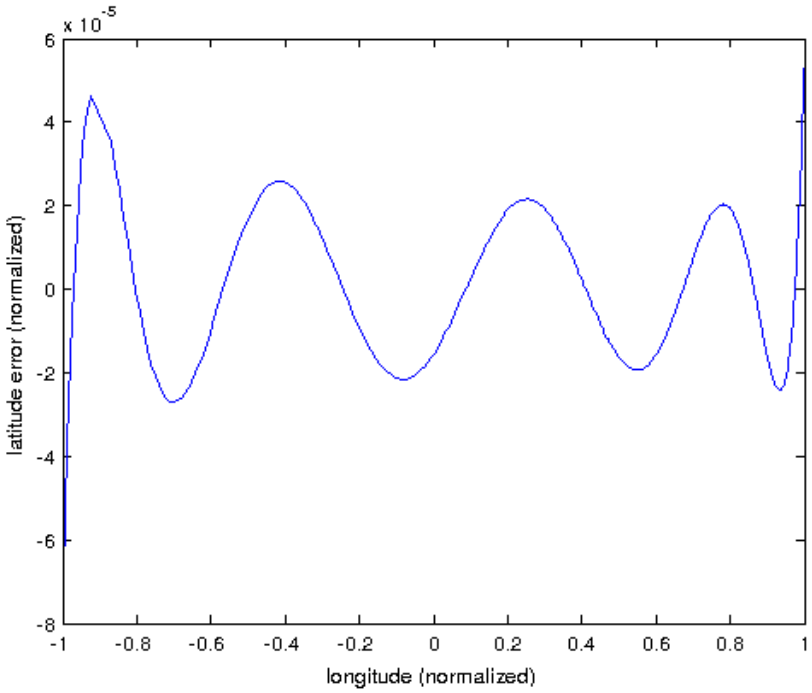

Figure 6.8: **The difference between the observed and the fitted normalized latitude, longitude values. An 8th degree polynomial has been fitted, that emulates the satellite track equation.**

In order to correct this a method has been designed and applied. The method is described in the following paragraphs and the main parts of the code can be found on the sections A.2 and B.2 of the appendix.

In first place the slope angles need to be defined in order to quantify the magnitude of the correction through the geometric equations. In order to do so, the DEM is used to get the height values in the satellite's along- and across-track directions, as both are necessary to define the plane in which the signal rebounds, more information on the used DEM can be found on the section 6.3.1. The along- and across-track height profiles are created using the *'grdtrack'* function in GMT, the script can be found on A.2. With this tool two files that include the DEM values on the along- and across-track direction are created, this represent the height profile on both directions for each of the measurements. The width defined for the profiles is of approximately between 7 and 13 km, as these size is accurate enough for a satellite that travels at 7.5 km per second and at this scale the ice sheet's surface is still uniform enough.

With the height profiles stored, the C++ routine B.2 is run on them to extract the slope angle values on both directions through the use of a linear least squares method. With the slopes calculated the correction is applied to the range values and the slope corrected range value is obtained. The following figures show the estimation of the slopes over Greenland for the SARAL/Altika tracks.

On figure 6.9 the modulus of the maximum slope angle, θ, for each point on the GrIS can be found, this magnitude is given by the next equation for a plane defined by two perpendicular angles. The dihedral angle is the angle between two planes when looked along their line of intersection, what corresponds to the steepest slope angle on the surface of the ice sheet. In this case the along- and across-track angles define the plane of the GrIS surface while the z = 0 plane corresponds to the one perpendicular to the nadir direction.

$$\Pi_{general} :: a_1\ x + b_1\ y + c_1\ z + d_1 = 0 \tag{6.14}$$

$$\Pi_{surface} :: z - \tan\alpha_{across-track}\ x - \tan\alpha_{along-track}\ y = 0 \tag{6.15}$$

$$\Pi_{satellite-track} :: z = 0 \tag{6.16}$$

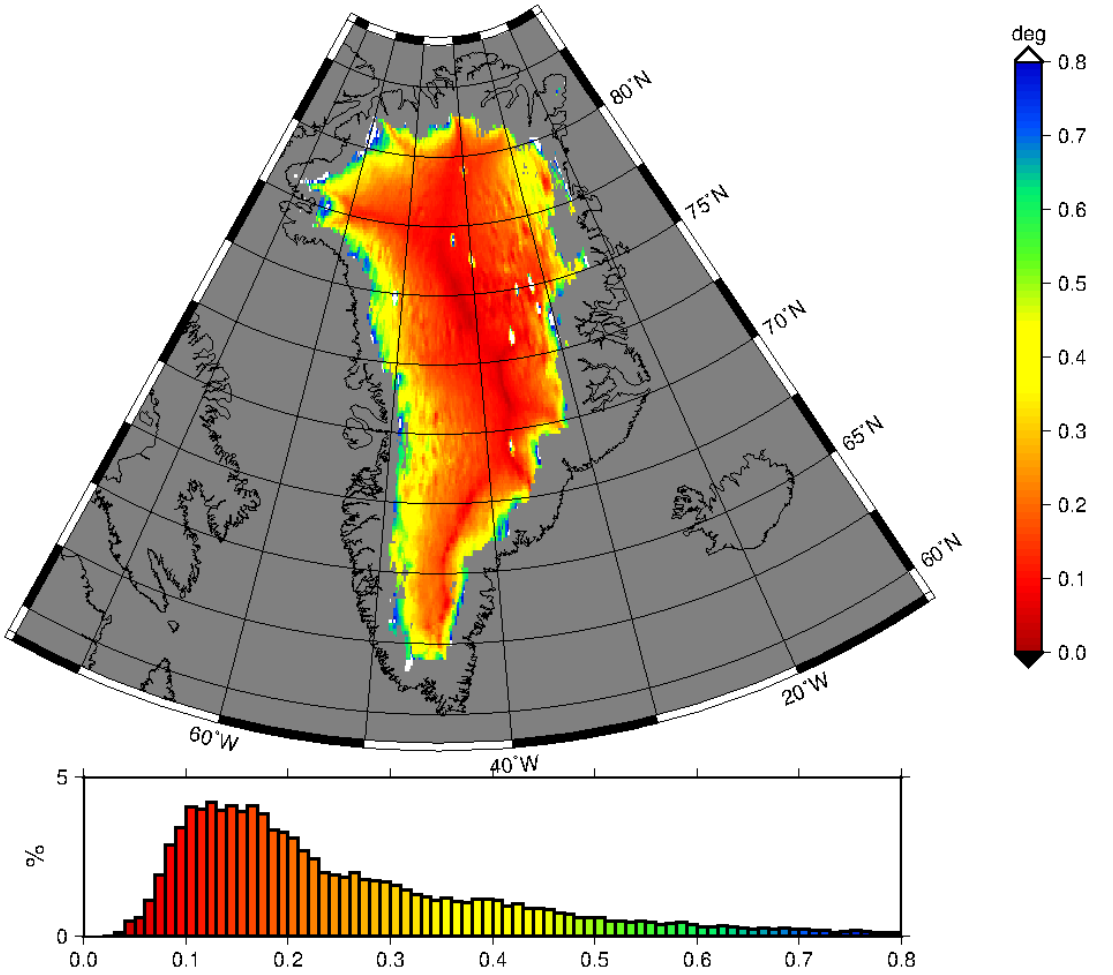

Figure 6.9: **The values of the slope on the steepest direction on each point in the GrIS.**

The dihedral angle for two planes:

$$\cos\theta = \frac{a_1a_2 + b_1b_2 + c_1c_2}{\sqrt{a_1^2 + b_1^2 + c_1^2}\sqrt{a_2^2 + b_2^2 + c_2^2}} = \frac{1}{\sqrt{1 + \tan^2\alpha_{along-track} + \tan^2\alpha_{across-track}}} \tag{6.17}$$

$$\tan^2\theta = \frac{\sin^2\theta}{\cos^2\theta} = \frac{1 - \cos^2\theta}{\cos^2\theta} = (1 + \tan^2\alpha_{across-track} + \tan^2\alpha_{along-track}) - 1 \tag{6.18}$$

$$= \tan^2\alpha_{across-track} + \tan^2\alpha_{along-track} \approx \alpha_{across-track}^2 + \alpha_{along-track}^2 \tag{6.19}$$

where θ represents the angle at the steepest direction on the plane that fits the DEM on the nadir point and taking into account that the angles are small and thus higher order elements are ignored.

In figure 6.9, it is clearly depicted how the central higher parts of the GrIS are almost flat while the edges show much more steeper geometry and therefore bigger deviations. The magnitude of the slopes is maintained below 0.2° for the central parts of the GrIS and it can rise as high as 1° values closer to the edges. Our results are in agreement with the results presented by Helm et al. 2014 p.1546 [11].

Regarding the corrections derived from the slope angles the absolute correction values are depicted on figure 6.10. The central regions of the GrIS show almost no correction as they show slope values below 0.1°, while the steeper edges show corrections that go from 10 to 50 meters.

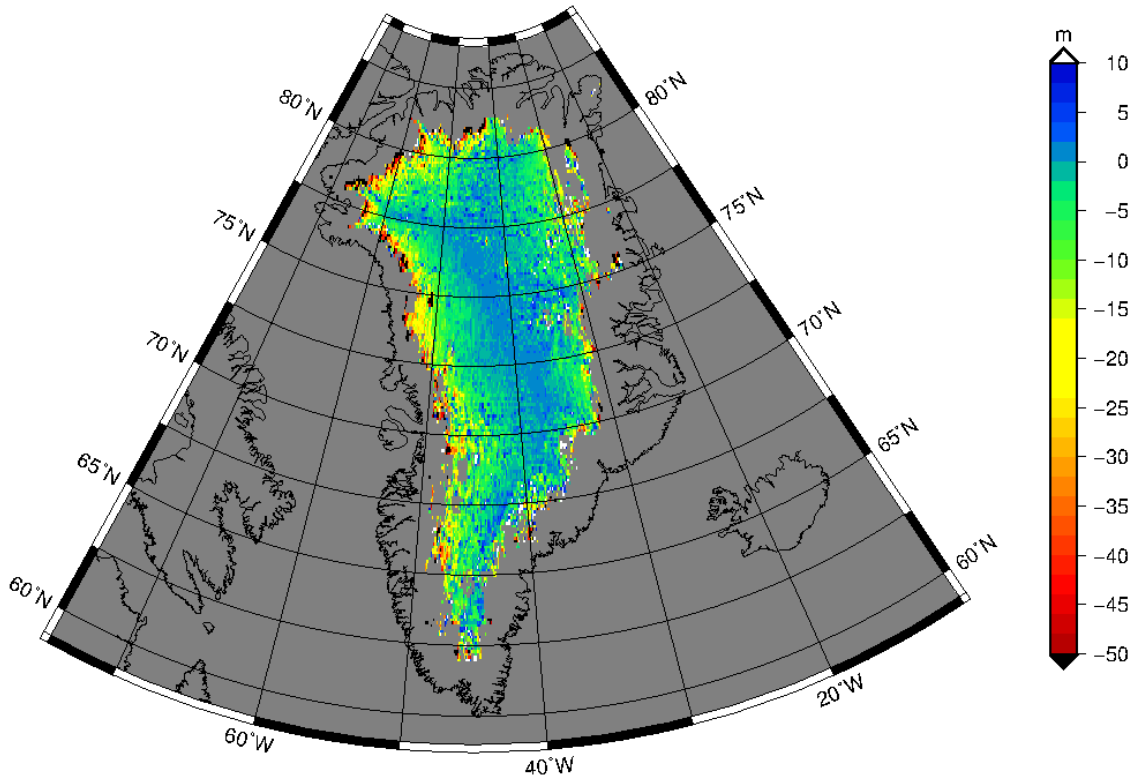

Figure 6.10: **The slope-induced deviation correction on the GrIS for SARAL/Altika.**

In order to estimate the quality of these results, the uncertainty of the slope-induced range deviations is calculated. This is derived from propagating the standard error of the linear regressions used to estimate the value of the slope angles on both dimensions (along- and across-track). The range correction is given by the relation in equation 6.12 and from here the relation between the slope-error and the range-error is derived, 6.20.

$$\sigma_H^2 = \sum_{i=1}^{2} f'(\alpha_i)^2 \ \sigma_{\alpha_i}^2 = \tag{6.20}$$

$$= H_m^2 \left[\left(\frac{\sin \ \alpha_{along}}{\cos^2 \alpha_{along}} \right)^2 \ \sigma_{slope \ along}^2 + \left(\frac{\sin \ \alpha_{across}}{\cos^2 \alpha_{across}} \right)^2 \ \sigma_{slope \ across}^2 \right] \tag{6.21}$$

Here σ_α represents the error on the determination of the slope angles on the along- and across-track dimensions.

The following figure 6.11 depicts the propagated error estimation values for the thickness on the ice sheets.

The figure along with the histogram shows that the correction quality is high on the high altitude centre areas of the GrIS while it decreases on the edges, where values above 4 meters can be found. As mentioned by Helm et al. 2014 [11] the uncertainty between the measurements by laser and radar altimetry range between 4 $\pm$ 25 meter for the regions with slopes below 1°, with the margins with higher slopes deviating by more than 7 $\pm$ 40 m. Therefore the measurements showing an estimated error above 25 meter have been excluded from the data set.

This shows the difficulty of determining the slope angle values along the edges of the GrIS where

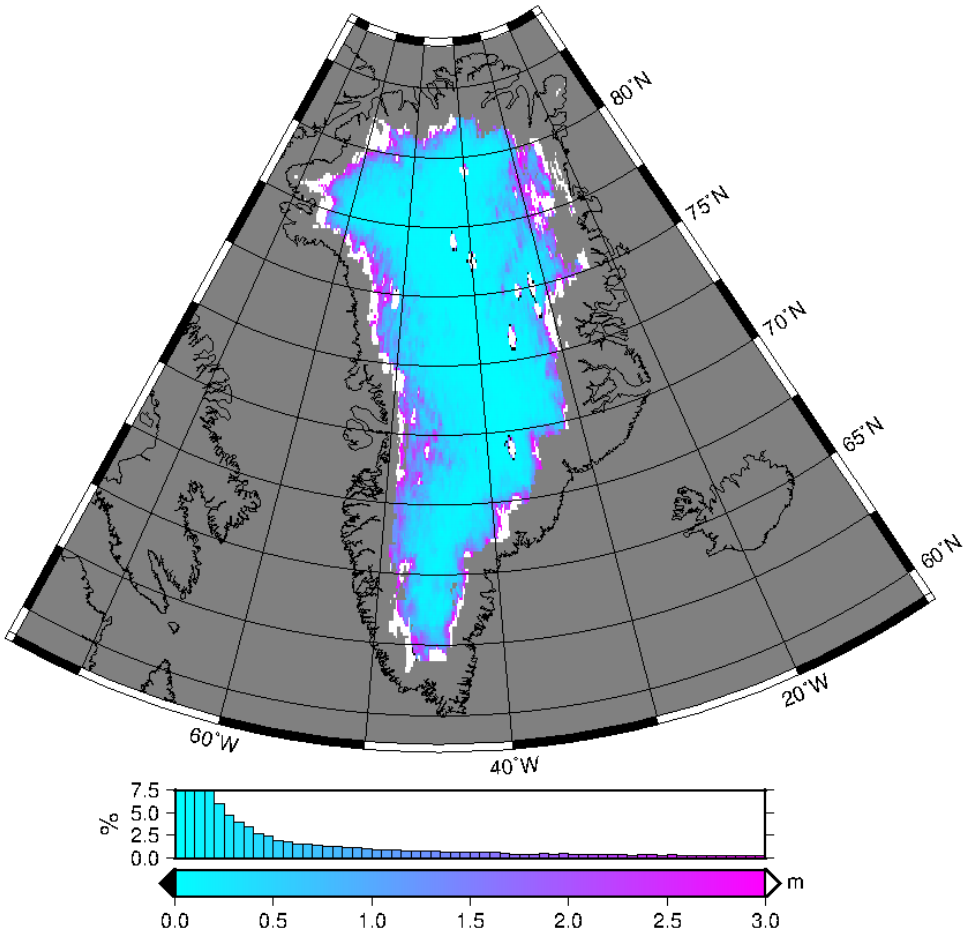

Figure 6.11: **The propagated error of the GrIS thickness SARAL/Altika data.**

the geometry is more irregular and the data models start to fail. The selected approach works correctly for the main area of the GrIS, although it fails to accurately describe it on the more steep and irregular regions.

Unfortunately, due to the accuracy limits set for the data, some of the data from the margins of the GrIS are lost and therefore the characterization of the ice melt signal from this regions lack the consistency of more central parts. This is again taken into account on later calculations.

6.4. Result

Once the corrections have been applied, the obtained thickness profile looks like the one on figure 6.12, while the difference with the DEM has been reduced as can be observed on figure 6.13.

This phase of the project has been developed using the data from 8^{th} cycle of the Altika radar altimeter measurements on the SARAL mission. This data correspond to measurements done from the 14^{th} of November of 2013 to the 19^{th} of December 2013.

The corrections have been able to get the satellite data produce thickness estimates closer to the DEM values. As can be seen on the histogram below the figure most of the data cells are within a $\pm$ 10 m error. And in addition a considerable area of the most central parts of the GrIS shows values close to $\pm$ 2 m. An article by Helm et at. 2014 [11] states the uncertainty between the radar altimetry and the laser ICESat DEMs to be less than 3 $\pm$ 15 meter, thus the results obtained for the Altika radar altimeter

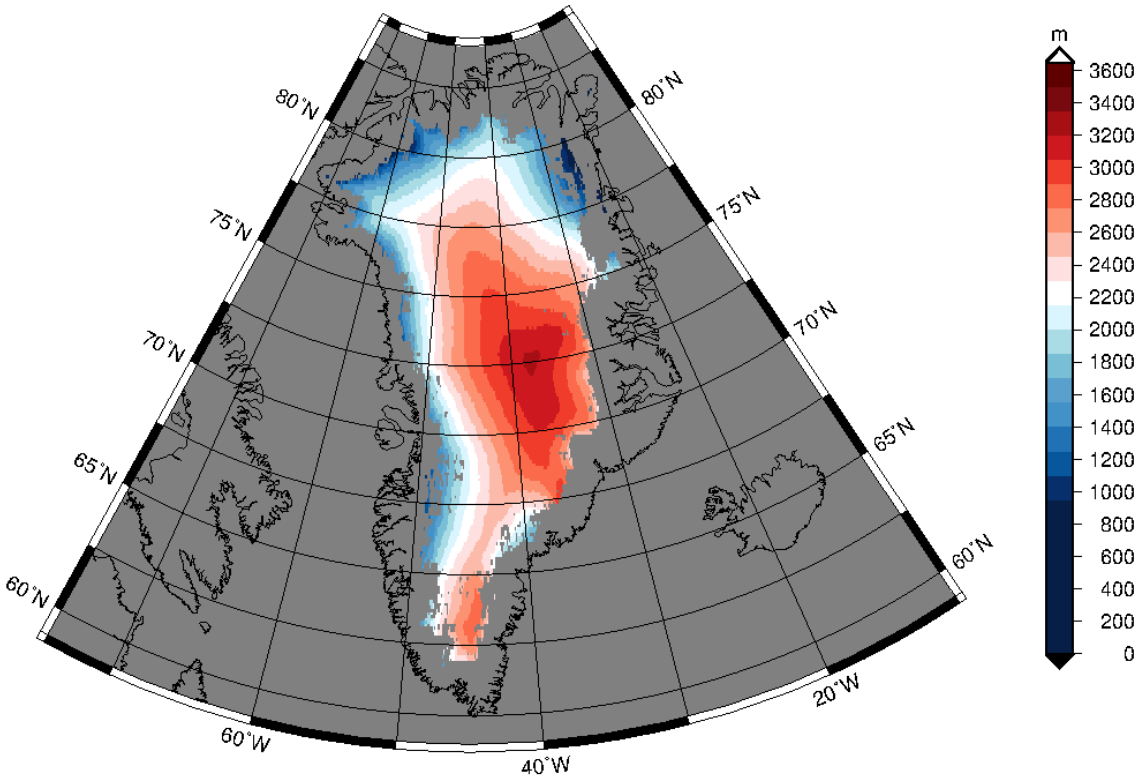

Figure 6.12: **The corrected version of the GrIS thickness measurements from SARAL/Altika.**

are within reasonable limits. This significant difference may be physically explained due to the inherent difference between the two techniques. As explained on section 3.1.2, the physical characteristics of the radiation used for each technique makes the measurement slightly different as the higher frequency of the laser altimetry radiation is reflected at the top of the ice sheet, on top of the snow, while the radar altimetry signals of SARAL/Altika and CryoSat-2 on the K_a and K_u bands penetrate deeper.

On the accurate determination of the satellite range estimation, as mentioned on the theoretical chapters 3, other phenomena also produce further deviations on the measurements that have not been characterized on this processing. Some like the signal penetration on the less dense part of the ice sheet or the volume scattering of this signal on the ice could account for part of the difference that is still seen on these results.

Another issue to take into account is the 8 year difference between the SARAL/Altika measurements (2013-2014) and the used DEM reference data set from the ICESat mission (2003-2005), that due to the increasing reduction of the GrIS could also bring some error into the data analysis. However, the yearly decrease on the thickness of the GrIS has been estimated to be at the centimetre level on its central regions, and higher on the edges, and therefore could not explain the several meter level differences observed on these results.

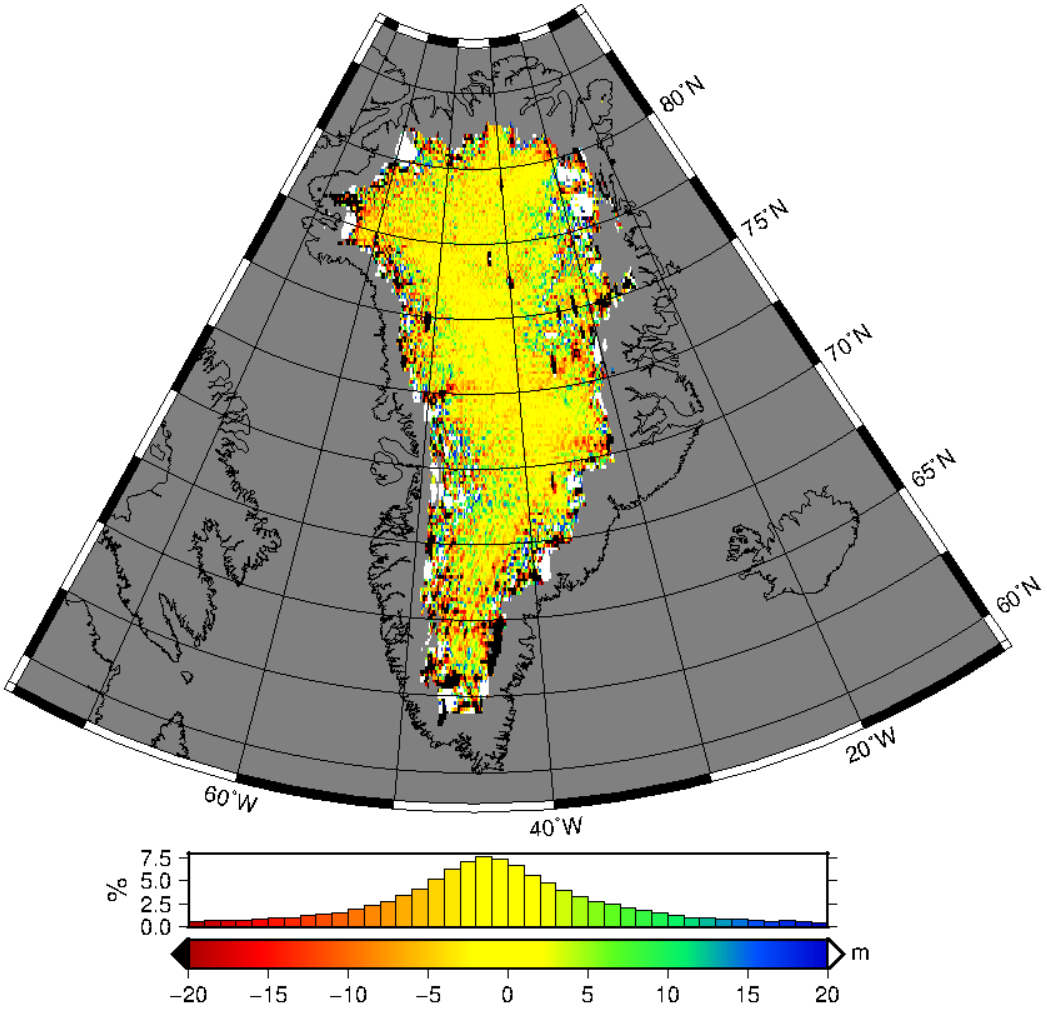

Figure 6.13: **The corrected version of the GrIS thickness measurements from SARAL/Altika.**

7

The Crossover Point Analysis

Being the main goal of this project the characterization of the rate of change of the Greenland ice sheet's mass, on this phase the calculation of the elevation changes is performed. This elevation changes are computed from the thickness measurements obtained on the previous chapter, however, first, a method to compare thickness measurements from different time-periods located on the same spot of the GrIS is designed. This happens at overlapping satellite tracks, which depending on the satellite orbit design happen on repeat-orbit tracks or at crossover points (intersections between ascending and descending tracks from different cycles), this way also eliminating the non-temporal errors on the range estimates. This is why the distribution of the satellite tracks and their intersections are thoroughly studied when designing an Earth observation mission.

Over the decades, several approaches have been used on satellite remote sensing missions when designing the optimum orbit that the altimeter should fly when collecting data. There are various criteria that are taken into account when doing so: the required spatial coverage and resolution, the temporal resolution (how frequently completes the satellite a whole data cycle/set) or the way the data-set is to be collected (data-set patterns and characteristics). Therefore in every mission the data collection is specifically studied and designed to provide the optimal quality and coverage.

Many Earth Observation missions are designed in a way in which the satellites fly over the exact same ground-track after some given time period or number of orbits. The following equations 7.2 describe the relation between the orbital elements in order to keep an **Exact Repeat Orbit** (ERO) with a certain cycle-periodicity (k, number of nodal days) and number of orbits (j) per cycle. These two parameters, j and k, deliver independent sun-synchronous orbit solutions when they have no common prime factors.

The required orbit altitude to get the desired exact repeat orbit is the following (Wertz 2001 [41]):

$$H = \mu^{1/3}(n\pi/180)^{-2/3} - R_E \tag{7.1}$$

where n, stands for the mean angular motion.

$$n = (j/k)(\dot{L} - \dot{\Omega}) - (\dot{w} + \dot{M}) \tag{7.2}$$

Being n the required mean angular motion for the ground track, and $\dot{L}$ and $\dot{\Omega}$ the angular motions of the Earth and the satellite track's ascending node. Then, the $\dot{w}$ and $\dot{M}$ represent the rate of change of the perigee and the mean anomaly.

$$\dot{L} = 360 \ \deg/side - real \ day \tag{7.3}$$

$$\dot{\Omega} = -2k_2 \ a^{-7/2} \ \cos i \ (1 - e^2)^{-2} \tag{7.4}$$

$$\dot{w} = k_2 \ a^{-7/2} \ (5\cos^2 i - 1) \ (1 - e^2)^{-2} \tag{7.5}$$

$$\dot{M} = k_2 \ a^{-7/2} \ (3\cos^2 i - 1) \ (1 - e^2)^{-3/2} \tag{7.6}$$

Where k_2 represents the J_2 effect due to the oblateness of the Earth:

$$k_2 \equiv 0.75 \ J_2 \ \mu^{1/2} \ R_E^2 \tag{7.7}$$

This brings some advantages at the moment of comparing the data and analysing their evolution. The data from satellites that make use of EROs can be processed through a **collinear analysis** method that makes use of those repeating ground tracks to improve the accuracy of the radial errors estimation. This eliminates the static components on the range estimation errors, for example the sea height variability estimations are improved by separating the ocean height variations from the geoid variations [42]. This orbit setting has been applied several times in many ocean height observing missions like Seasat, Geosat, Topex or ESA's ERS missions.

However, this technique does come with certain drawbacks. The main issue is the one related to the building up of resonance effects on the orbit perturbations, what makes the missions more sensible to geologically induced perturbations. This also concludes on a higher propulsion being required to keep nominal orbit to counter the increased perturbations.

In many other cases, where the measurement conditions and range deviations are harder than in oceans or the atmosphere (ice sheets on Greenland or Antarctica) the satellite tracks are designed to provide a number of intersection points between the ascending and descending tracks. These intersection points are then used to make estimations on the variability of the observed magnitude.

On the following pages, the theoretical explanation for the use and generation of crossover points is introduced on section 7.1. Then the practical methods and results of the calculation of elevation changes through crossover points are presented on section 7.2.

7.1. Crossover Analysis: Theory

As mentioned on the introduction, on the satellite altimetry technique several methodologies have been employed for the computation of the elevation variations at different time moments. And after analysing the relevant literature and considering the characteristics of the SARAL/ALtika mission for this project we have selected the crossover difference method as the most suitable.

The satellite orbit tracks are generally classified in two groups, the tracks that follow an **ascending** trajectory towards higher latitudes, and the **descending** ones. As it can be observed in figure 7.1 the SARAL/Altika satellite on its retrograde (longitude decreasing direction) crosses the Greenland area on ascending and descending trajectories.

Notice that the orbit geometry itself produces an imbalance between the number of crossover points in the higher and lower regions of the GrIS, where a higher density of crossover points is found in the higher latitudes.

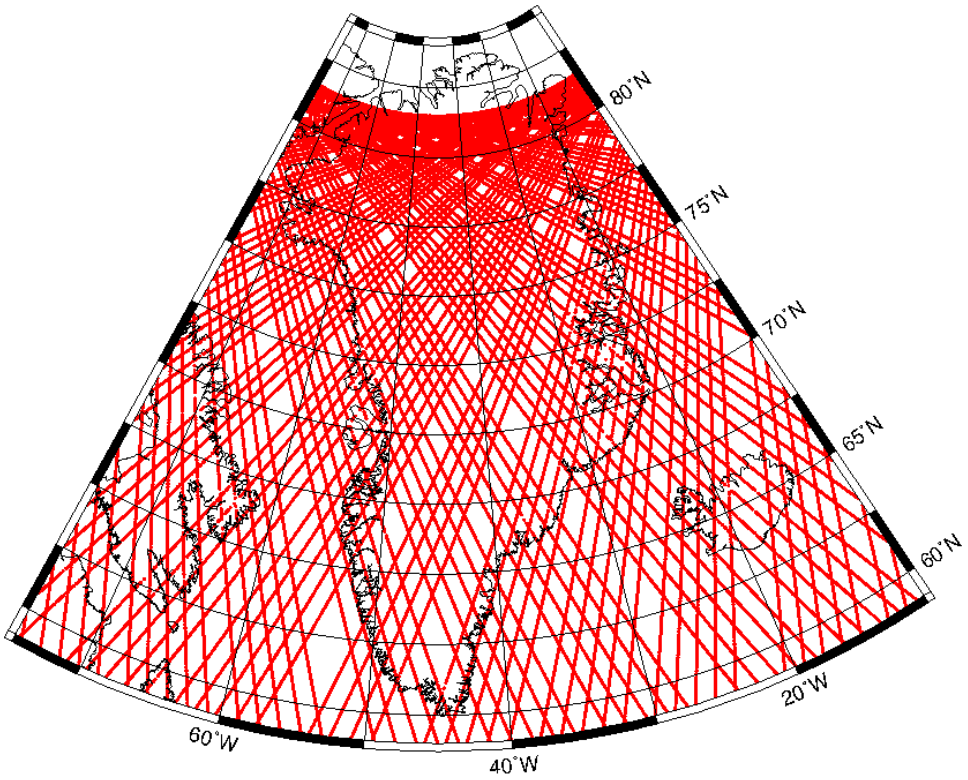

Figure 7.1: **The of the ascending and descending tracks intersecting at crossover points, for the SARAL/Altika mission on the 6th cycle. Just half of the tracks are shown as to reduce the density and make the figure clearer.**

These track intersection points are used as reference points where the analysis of different magnitudes can be done. The range values on the two intersecting tracks are used to make an estimation on the difference between the two and thus get an elevation change estimate.

As described on the previous chapter 6.2, the range of the satellite to the target can be described in the following way:

$$r_{corrected} = r_0 + \delta r_{geoid\ height} + \delta r_{atm} + \delta r_{earth\ surface\ variations} + \delta r_{instr.} \tag{7.8}$$

where the r_0 is the range value with respect to the reference ellipsoid. And the δr values are the range corrections applied for the atmospheric, geoid height, Earth surface or instrumental effects.

On these crossover points the crossover difference is calculated:

$$\Delta r_{t_i,t_j} = \Delta r_0 + \Delta(\delta r_{geoid\ height}) + \Delta(\delta r_{atm}) + \Delta(\delta r_{earth\ surface\ variations}) + \Delta(\delta r_{instr.}) \tag{7.9}$$

where $\Delta r_{t_i,t_j}$ is the range difference from time t_i to t_j at the crossover point. On this magnitude, the non-temporal or long-term changing elements are eliminated what enables the used of this difference for the study of the temporal variations of the range at this crossover points.

The crossover differences have generally been computed the following way, combining the range difference between the ascending and descending tracks on both times, also in Armitage et al. 2014 [43]:

$$\Delta H_{21}^{(\pm)} = \frac{1}{2}[(H_a(t_2) - H_d(t_1)) \pm (H_d(t_2) - H_a(t_1))] \tag{7.10}$$

when using the sum ”+” version of the equation the time-varying component is kept and averaged between the two crossover differences (ascending and descending as reference) at the same location.

While when using the subtraction "-", the time-varying element is erased and just the static-component is kept. However, the existence of a bias between the ascending and descending tracks causes a significant differences and reduces the measurement's accuracy.

This technique has been applied when studying data from several radar altimetry missions like the ISRO/CNES SARAL/Altika campaigns. It could also be applied using multi-mission data or just single-satellite one, although the difference between the satellites may add some extra biases that need to be identified.

7.2. Crossover Analysis: Data

The crossover points for studying the SARAL/Altika data have been generated using the '*max2*' function incorporated on the RADS library. This utility makes use of orbital dynamics equations to predict at which time and position certain satellite tracks will intersect.

In first place, once the satellites, cycles and passes to be analysed are specified, 'max2' reads and stores in the cache all the relevant pass information. Then, comparing all the possible ascending and descending pass couplings the valid crossover points are identified. The main input used by the software is the equatorial crossing time and position of the specific passes, what allows for the identification of the position where two passes will intersect with each other.

Once the position and time of the crossover point is identified, '*max2*' uses the closest measurement points in each pass to interpolate the values of the target magnitudes on the crossover point.

This way a set of crossover points has been generated for every cycle using one cycle as reference, cycle number 2 that corresponds to a 35 day cycle starting on the 18^{th} of April 2013.

In order to incorporate the missing corrections to the new data set, dry and wet tropospheric effect and the slope induced deviation explained on chapter 6, a time tagged list of these corrections has been created for the SARAL/Altika mission. This allows for the identification of the measurements on the crossover points by time tagging and thus applying the necessary corrections on them.

On the same line as by the '*max2*' code interpolation at the crossover point for the range estimation, another interpolation is carried out for the above mention corrections. The interpolation is done by using the time tagged corrections and linking the crossover points times to the time-tagged correction record.

The '*sample1d*' utility on GMT enables for various interpolation schemes that have been useful for this task. In order to determine which scheme delivers the most reliable results with the lowest standard deviation, a comparison between three interpolation schemes, the linear, cubic spline and Akima, has been done. The Akima interpolation is an sub-spline interpolation that makes use of third order polynomials with next-neighbour points.

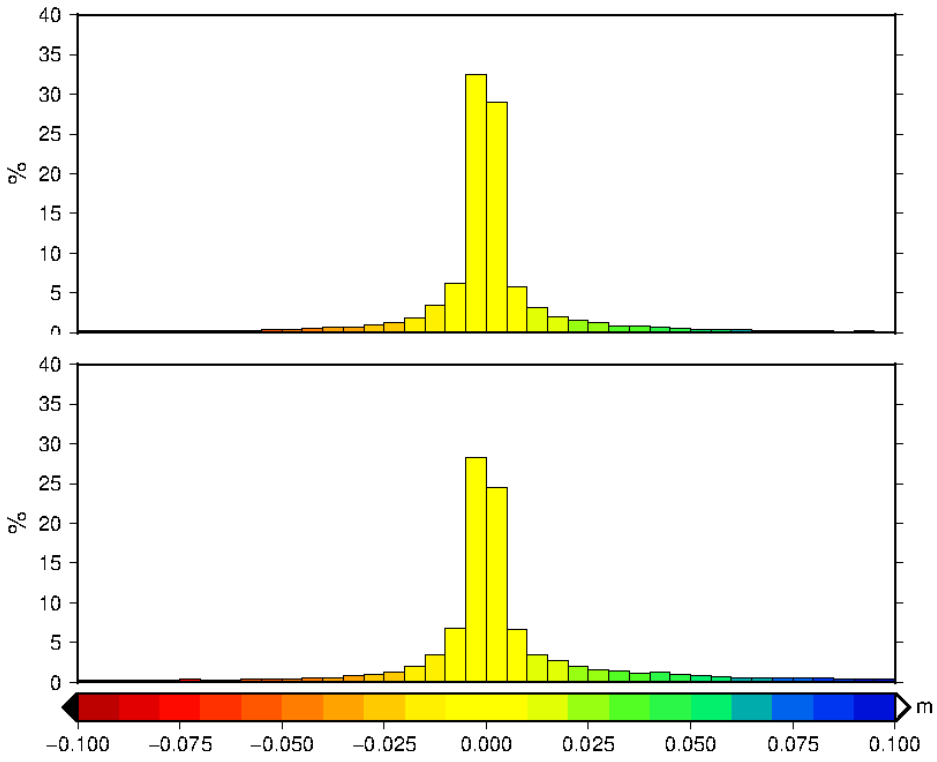

Figure 7.2: **Histograms of the uncertainty difference between the linear interpolation and the Akima (top)/ cubic-spline (bottom) interpolations. The predominance of negative values proves that lower uncertainties are produced on the linear method.**

The comparison between the interpolation schemes has resulted in the linear method being the most reliable one. The following figure 7.2 shows the difference on the standard deviations of the generated interpolated points between the three interpolation methods, the results from the linear case are subtracted with the other two cases. The result is very similar for the three cases, the difference does not amount to higher than 3 millimetres, however it is clear that the linear case has yielded lower standard deviations in general and thus this one has been selected.

Once the corrected range values were available at the crossover points the crossover differences have been computed. On this process a data quality filter has been applied due to these data points being clearly outliers, it excludes every measurement with higher elevation changes than 10 meters, a filter also applied by Zwally et al. 1989 [44].

Using this methodology a common result of the location of qualifying crossover points is depicted on figure 7.3.

Here it can be observed how as in the figure 7.1 the density of crossover points is much higher in northern latitudes. In addition, the availability of the data and accuracy filters set on them yields a coastal region without crossovers. This factors make the characterization of the elevation variability significantly harder. This issues will be better analysed on the discussions chapter 10.

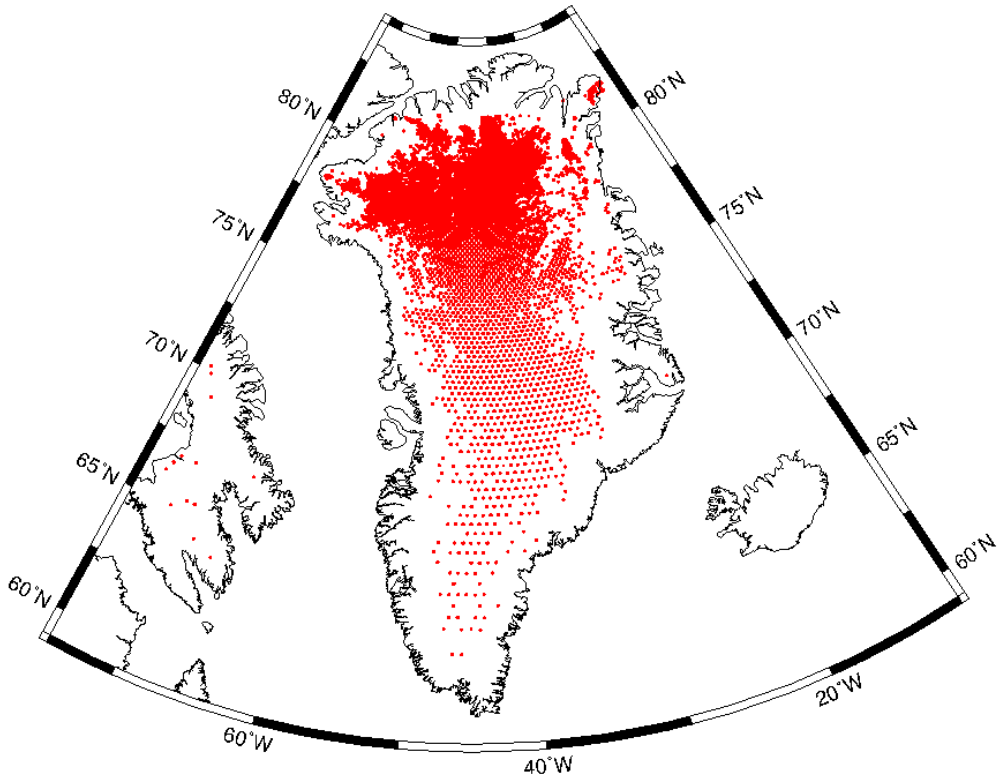

Figure 7.3: **Crossover points with valid data on the GrIS generated between the cycles 2 and 14 for the SARAL/Altika mission.**

7.2.1. Data analysis

The above described method has been applied for every cycle available for the SARAL/Altika mission, using cycle number 2, April 2013, as the reference cycle for computing the elevation changes. The code can be found on appendix A.3.

This first figure 7.4 shows the change observed on the crossover points between the cycles 2 and 7. For the plotting a 0.5°x0.5° near-neighbour gridding procedure has been applied. The changes have been computed by subtracting the oldest cycle, 2, to the newest, 7, thus the negative (blue) values represent elevation reductions and the positive (red) elevation raises.

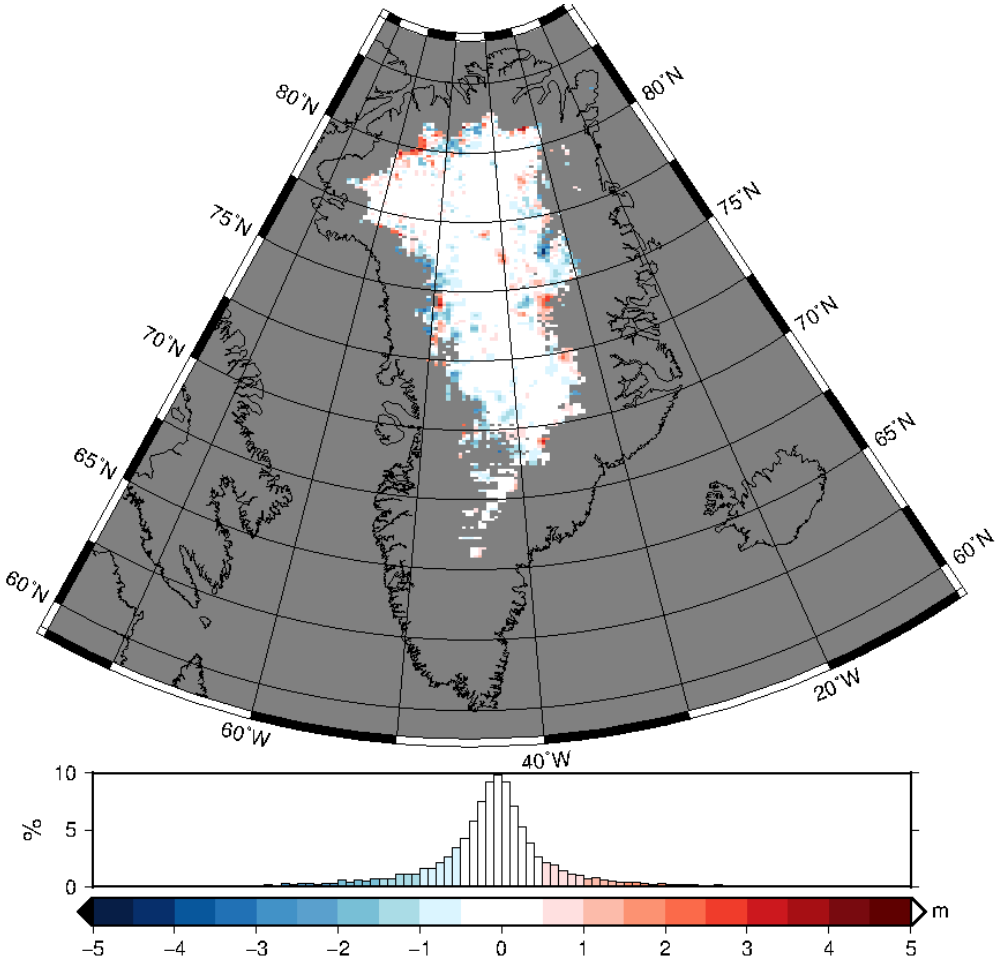

Figure 7.4: **Crossover elevation differences between cycles 2, April 2013, and 7, October 2013.**

The general trend of change shows a considerable variability on the more coastal regions of the GrIS, while the high altitude plains do not show much change. However, it is difficult to state which the general trend on this figure is without looking at the histogram below, as there are regions showing both increasing and decrease elevations. The histogram shows a slight tendency to the negative values, indicating an overall loss of volume, which is expected for a period spanning the summer months. However, a broader analysis with more data points and longer time-spans is required to properly address this question.

On this second figure of elevation changes 7.5 on the GrIS the results from the cycles 12, 13, 14 and 15 (that gather data from April to July 2014) have been used, taking cycle number 2 as the reference.

These results with 29918 crossover points show a more smooth pattern for the elevation changes on Greenland with blue (decrease) being predominant for most of the coast, although there are some areas that show elevation increases too in the south. The coverage of the data is also slightly improved when compared to 7.4 as the data reaches closer to the coast regions.

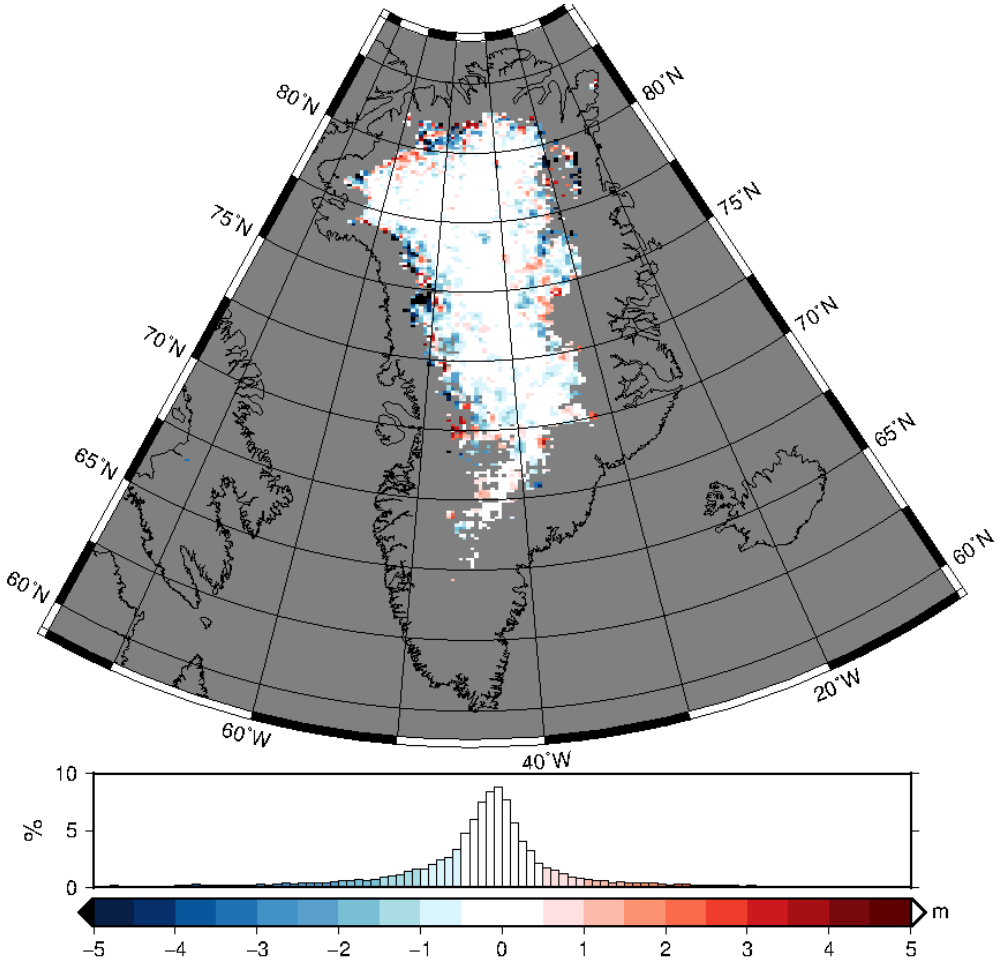

Figure 7.5: **Averaged elevation changes at crossover points for the cycles 12, 13, 14 and 15 vs. cycle 2.**

This figure supports the idea of a decrease on the overall ice sheet volume through the almost two years of operation of SARAL/Altika, as both the map and the histogram show. However on the next section more a statistical analysis of the data is attempted.

As mentioned on the beginning of this section, a remark must be done on the clear loss of data going on on the coastal, steeper, regions of the ice sheet. This data loss is linked both to the quality of the range estimation measurements and the slope correction's accuracy, as well as the availability of measurements over this region. As explained on the altimetry remote sensing chapter 3, the altimeter uses a tracker to properly centre the signal reception window for the two-way travel time of the area it is orbiting. However, the performance of this tracker decreases on the regions where significant slopes are found, like the coastal regions of an ice sheet. Therefore an improved tracking, a re-tracking, is done once the data is downloaded to the ground processors. An extensive research on the optimization of the re-tracking algorithms is currently on-going, this could help to extend the availability of data for these regions.

7.2.2. Overall change trend estimation

In order to more precisely estimate the variations going on the GrIS surface data, the crossover differences have been studied making use of two different bulk methods.

In the first case every data point has been treated as equal. The elevation changes have been studied against the time (between the reference measurement at cycle 2 and the measurement one), the data points are plotted in the next figure 7.6.

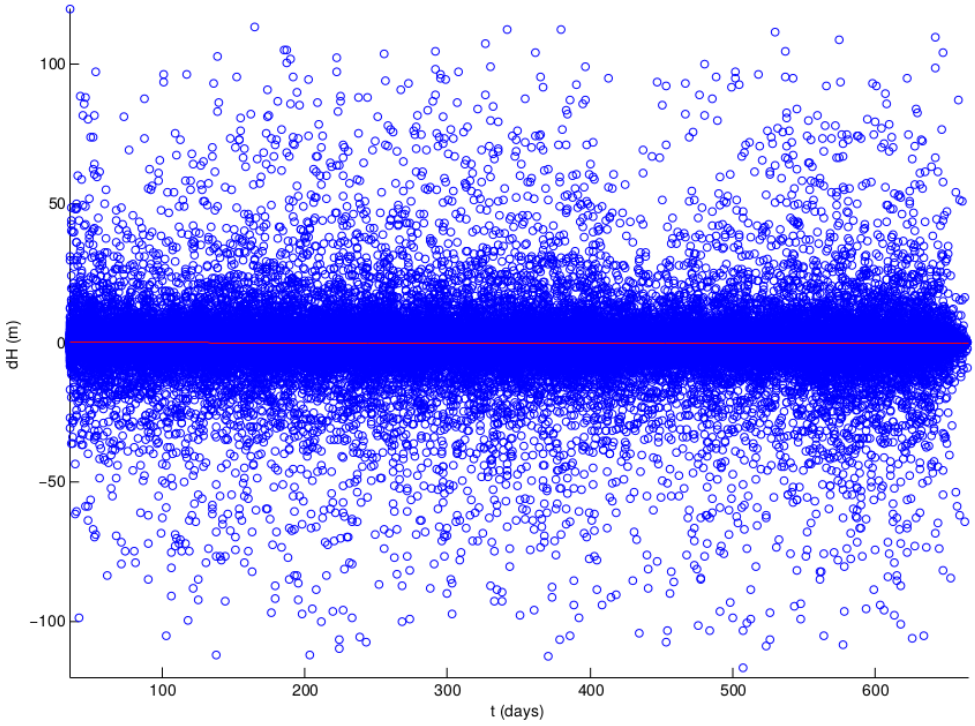

Figure 7.6: **Linear fit of all the crossover elevation change points available over the SARAL/Altika mission.**

The figure shows the wide range of elevation changes included on the 140296 crossover point measurements, raging from -100 to +100 meter. A linear fit has been calculated on them, described by the next equation where time (t) is given on days and the elevation change (dH) in meters. The overall pattern from the individual elevation change points shows a decreasing trend.

$$dH = -0.0003925\ t(days) + 0.05181 \tag{7.11}$$

The slope of the linear fit yields a 14.33 cm per year elevation decrease estimate for the GrIS. In order to estimate the standard error (SE) of the linear fit's slope the following equation is applied:

$$SE_{slope} = \frac{\sqrt{\sum(dH_i - \hat{dH}_i)^2/(n-2)}}{\sqrt{\sum(t_i - \bar{t})^2}} \tag{7.12}$$

where n is the number of data points.

For this first case the SE of the linear regression's slope amounts to 0.0001244 m/day or 4.5404 cm/yr. Resulting in an annual overall elevation change of:

$$\frac{dH}{dt} = -14.327 \pm 4.540\ cm/yr \tag{7.13}$$

In a different attempt to quantify the evolution of the ice sheet in a bulk, the cycles have been treated individually by averaging the values of the elevation changes 7.14 of each cycle and studying the variation with respect to the average time of the cycle (35 day intervals). The following figure 7.7 shows the individual points of elevation changes for each of the cycles referenced after April 2013,

cycle number 2.

$$dH_{j\ average} = \frac{\sum_{i=1}^{N}(H_{i,j} - H_{i,2})}{N} \tag{7.14}$$

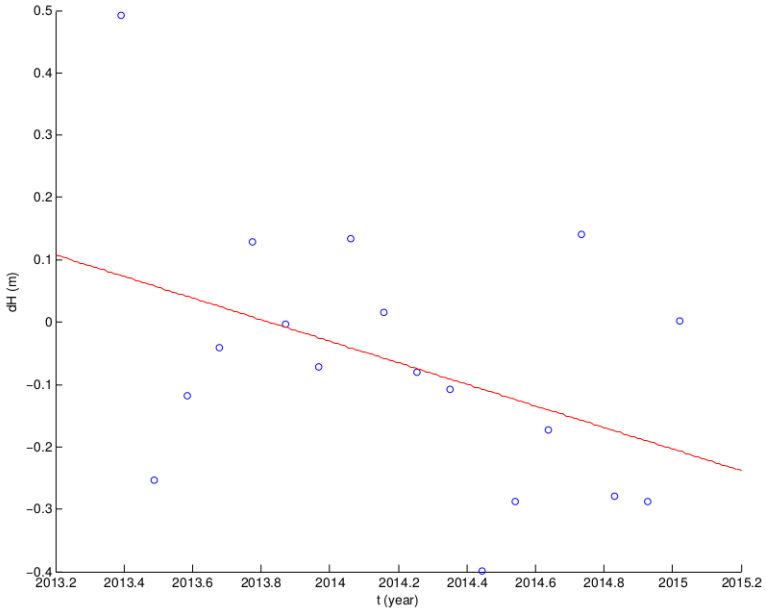

Figure 7.7: **Linear fit of the elevation changes averaged per cycle (35 days). The first data point corresponds to the 3^{rd} cycle, May 2013.**

The linear fit results in a 17.307 cm per year decrease, in this case the time t in the equation is given in years.

$$dH = -0.1731t(years) + 348.54 \tag{7.15}$$

The obtained standard error using equation 7.12 of the linear fit's slope is of 9.336 cm/yr.

$$\frac{dH}{dt} = -17.307 \pm 9.336\ cm/yr \tag{7.16}$$

On figure 7.7 seasonal patterns could have been observed, however, due to the short temporal extent of the available data at the moment for the SARAL mission, almost two years, and the uncertainty on them it is difficult to say whether the oscillations on the elevation variations correspond to a seasonal variation or not.

7.2.3. Regionalized elevation changes

The above presented estimations of the overall elevation change rates are an interesting magnitude to analyse how the general trend on the ice sheet is evolving. However, when aiming for precise results, it is necessary to consider the loss of certain regional data on those coastal regions where most of the mass loss is reported to happen, Hurskman et al. 2014 [45], and Sørensen et al. 2011 [10]. Therefore, on this section the consideration of the contribution of this uncovered area is attempted.

On the following analysis, in order to better characterize the elevation changes the crossover points are regionally classified by using equally-sized cells. This way the elevation change and volume change

signals can be locally identified and through more refined extrapolation techniques the overall GrIS volume change estimate calculated.

However, as mentioned on previous sections, due to the satellite orbital mechanics the density of crossover points is not the same on all the regions of the GrIS, it significantly decreases with latitude leading to the averaged values being formed with fewer points in the southern part. Therefore an analysis on the number of points has been carried out, which revealed the distribution of the number of points averaged on each cell, this is depicted on figure 7.8 (right).

When doing the regionally distributed analysis of the data, a step is required to be taken in order to filter out the out-lying crossover difference points. Thus, elevation changes at crossover points higher than 10 meters are left out of the computation. This filtering procedure eliminates 1545 crossover points out of the set of 15141 point data-set formed by cycles 12 and 13 referenced to cycle number 2, the same as the one used in figure 7.8. It must be noted that values presented on the following figures are normalized to the annual period values.

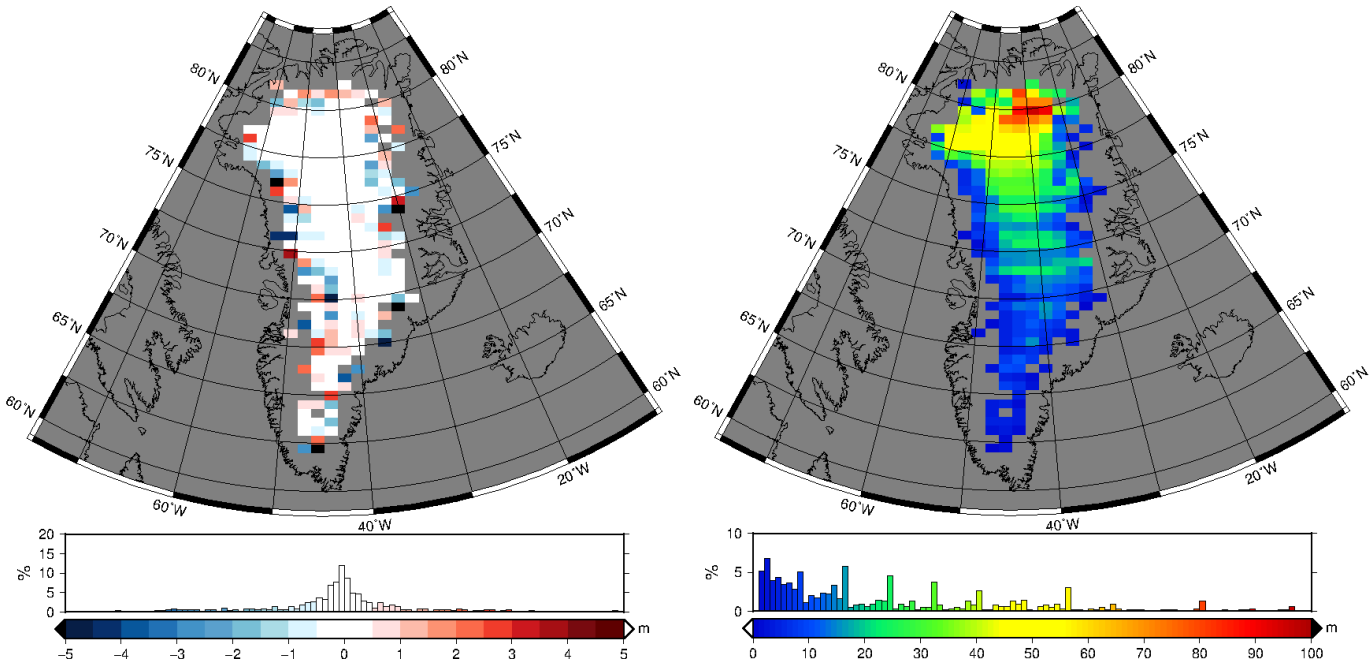

Figure 7.8: **50x50 km^2 sized cell averaged values of the elevation change on the GrIS for the cycles 12-13 using cycle 2 as reference (left). The number of crossover points on each 50x50 km^2 cell (right).**

Due to the unreliability of cells that contain a low number of points, the cells with fewer than 6 crossover points have been rejected and thus a new regionalized picture is obtained. The limit of 6 data points has been empirically obtained in an attempt to keep the highest coverage excluding the most unreliable data, in the case of 25x25 km^2 the limit is reduced to 4 due the lower size of the cell.

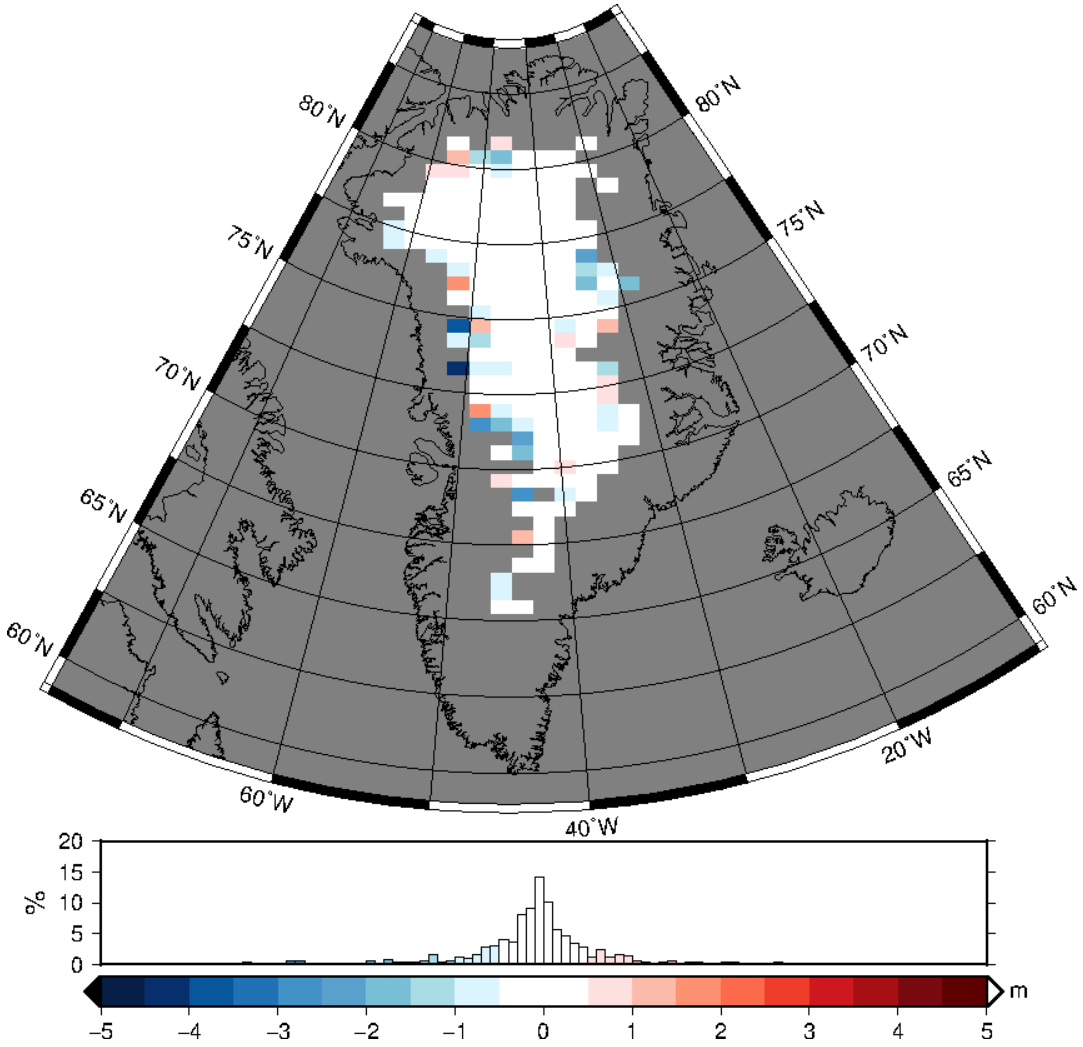

Figure 7.9: **Regionalization of the elevation changes averaged in 50x50 km^2 cells, where cells with less than 6 points have been rejected.**

When comparing the two versions of the regionalized data plots, the one where the cells containing fewer than 6 points were rejected shows less extreme values and a smoother geographical distribution.

The calculation of the standard error of these regional values has been done by computing the propagated standard deviation of the crossover points contained on the regionalized cells. This way a realistic error estimate can be computed on the volume and mass change estimations.

$$\Delta(\Delta H) = \sqrt{\frac{1}{N^2}\sum_{i=0}^{N}\sigma_{H_i}^2} \tag{7.17}$$

where N represents the number of points contained in each cell. The following figure 7.10 shows the standard errors obtained for the regionalized elevation changes on 50x50 km^2 cells. It can be observed how most of the cells show deviations below the 1 meter, while a few on coastal regions show higher ones.

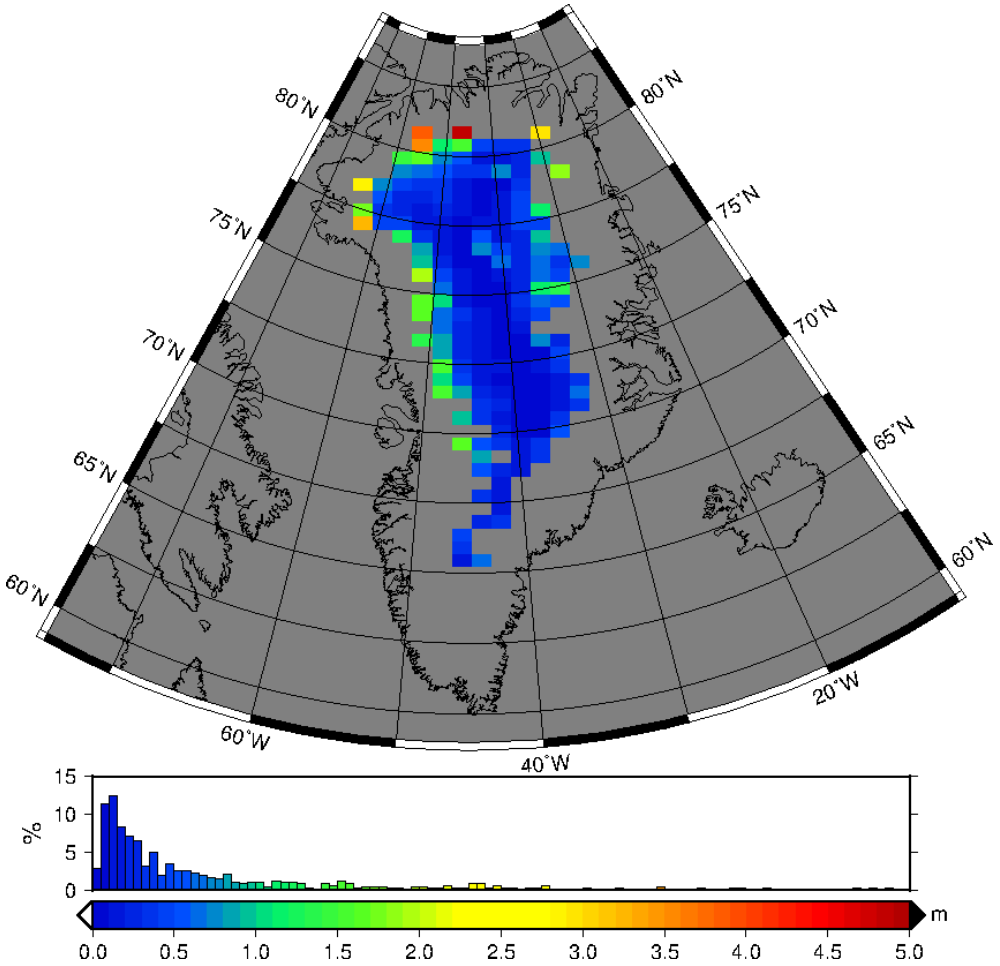

Figure 7.10: **Standard error of the regionalization of the elevation changes averaged in 50x50 km^2 sized cells.**

The same procedure has been applied to form a regionalized elevation change grid of 25x25, 75x75 and 100x100 km^2 cell sizes. The figures are not included in this chapter because they do not provide any further insight, but the data is later used on the volume change estimation.

The regionalized picture of the elevation changes shows significant elevation decreases on the north-western and north-eastern coasts of the GrIS, while the central and northern regions show a more stable situation. In addition, the southern part shows some slight signs of elevation increase. When observing the histogram of the resulting data, although the data is wide and flat, a clear negative elevation change can be noticed.

This results come into agreement with the general pattern of the GrIS's evolution described in other sources like the analysis made by Sørensen et al. 2015 [46] for the Envisat mission between 2003 and 2009, where significant elevation decreases were observed over the coast especially on the northern west and east coast, but also in the south-eastern coast, while the southern interior parts showed a small growth on the thickness.

7.2.4. Laplacian Differential Molecule method: Smoothed elevation changes over the GrIS surface

As for the third method applied on the estimation of elevation changes, a mathematical relation has been established to ”fill” the regions that have few or are filled with unreliable data points. In this way the extrapolation of the elevation change is done more smoothly using a Laplacian differential relation propagation between contiguous cells. In order to apply this method, a Matlab code has been written to handle the matrix calculations, it can be found on the appendix section C.1.

With this method, first, the crossover points computed as presented in the previous chapter have been used as the input and have been organized into a regular grid where 0.5°x0.5° cells have been used. These cell-by-cell averaged elevation changes form the observation data array and have also been used as initial values for applying the Laplacian differential molecule method.

On a second step, one of the problems that the previous methods highlighted is tackled; the existence of empty cells due to the lack of data or unreliability. Therefore, in this method a set of core points is selected to represent the GrIS that include ’empty’ and data filled cells. The core points are thus formed by the measurement filled cells and those cells that are within close reach of these first ones (three step proximity has been chosen as neighbouring distance). This way, the interior empty cells and the lost data areas in the coastal regions are accounted for by using the laplacian differential molecule propagation from the core cells. Regarding the cells that lay on the margins of the GrIS, and thus have connection to one or more core cells, are identified as the boundary cells that hold a no-elevation change conditions.

The Laplacian differential molecule method is based on establishing the signal propagation relation between the core and adjacent cells using the Laplacian matrix 7.11. On the first part of this matrix the relations obtained from the Laplacian operator working on the observations array are defined. The following equations explain the condition for smoothing the surface signal that is directly related to the difference between one core point and the surrounding ones next to it, thus for example flat surfaces will have a null operation acting on them.

The laplacian operator acting on ϕ with the no curvature condition.

$$\Delta\phi = \nabla^2\phi = \frac{d^2\phi}{d^2x} + \frac{d^2\phi}{d^2y} = 0 \tag{7.18}$$

On the specific grid elements this translates into.

$$\phi_{i,j} = \frac{1}{4}(\phi_{i+1,j} + \phi_{i-1,j} + \phi_{i,j+1} + \phi_{i,j-1}) \tag{7.19}$$

$$\phi_{i,j} - \frac{1}{4}(\phi_{i+1,j} + \phi_{i-1,j} + \phi_{i,j+1} + \phi_{i,j-1}) = 0 \tag{7.20}$$

This Laplacian operator equations are structured in the following way for the Laplacian matrix: the central nodes are connected to the 4 contiguous grid cells, thus the degree of these nodes is 4 and the diagonal of matrix is filled with values of the degree. For the adjacent grid cells -1 values are allocated.

By establishing this kind of relation between the differences between the grid cells in the same area are reduced in every iteration smoothing the transitions and completing for the empty nodes.

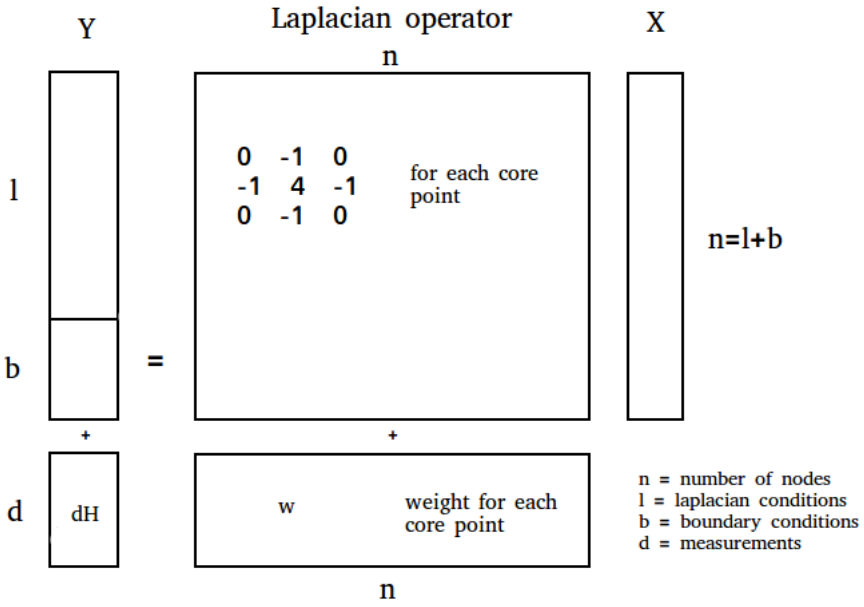

Figure 7.11: **Structure of the Laplacian differential matrix that is solved through least squares method.**

In addition to the core points, the set of boundary cells are defined to suffer no elevation changes by setting an identity on the boundary conditions part of the matrix and zero value elevation changes on the observation data array.

The third element added to the condition equations to be filled by the solution values is the condition to hold the pattern of the original elevation change values of the crossover measurements. In order to give bigger relevance to the Laplacian estimates and allow certain level of propagation of the smoothing, a weight is given to the elevation change measurements from crossover points. The value of this weight is the inverse of the variance of the elevation change observations array.

$$w = \frac{1}{\sigma^2_{\Delta H}} \tag{7.21}$$

The following equation shows the relation of the above depicted matrix structure (L) and the observations array (X) from which a smoother estimate of the overall elevation changes is obtained by applying a least square method. In order to obtain the intended propagation of the observed signal equation system is solved iteratively at least three times, what yields a smoothed signal distribution for the regionalized elevation changes.

$$Y = L * X + \epsilon \tag{7.22}$$

The following picture 7.12 depicts the more detailed distribution of elevation changes for the case comparison between the crossovers computed between the year 2014 (cycles 10 to 20) and the second cycle (April 2013) used as a reference, for an amount of 73975 crossover points. In this case the comparison between the months of April of the years 2013 and 2014 has been avoided due to the low number of points that it provides, what is critical for the use of this method.

A similar procedure has been applied to the standard error values and the resulting distribution can be seen on the next figure 7.13.

By comparing both results to the one obtained on the regionalized method 7.2.3, although the observed time periods are different, it can be said that the elevation change and standard deviations follow a similar pattern on both cases. An elevation decrease is observed on the north west and east

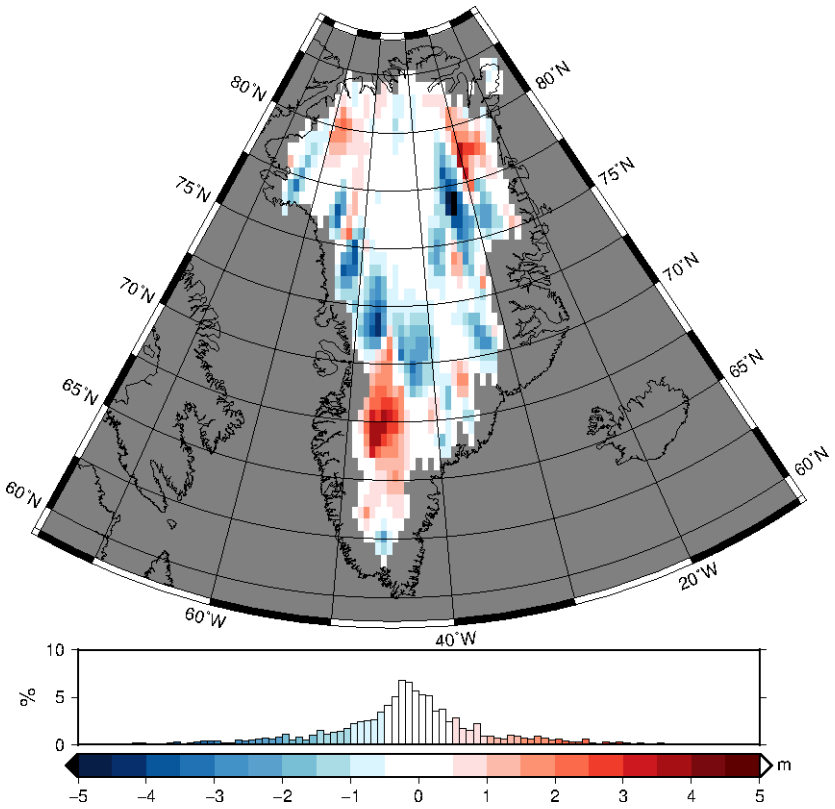

Figure 7.12: **The observed elevation change obtained using the laplacian differential molecule method on the crossover points from measurements from 2014 referenced to cycle number 2.**

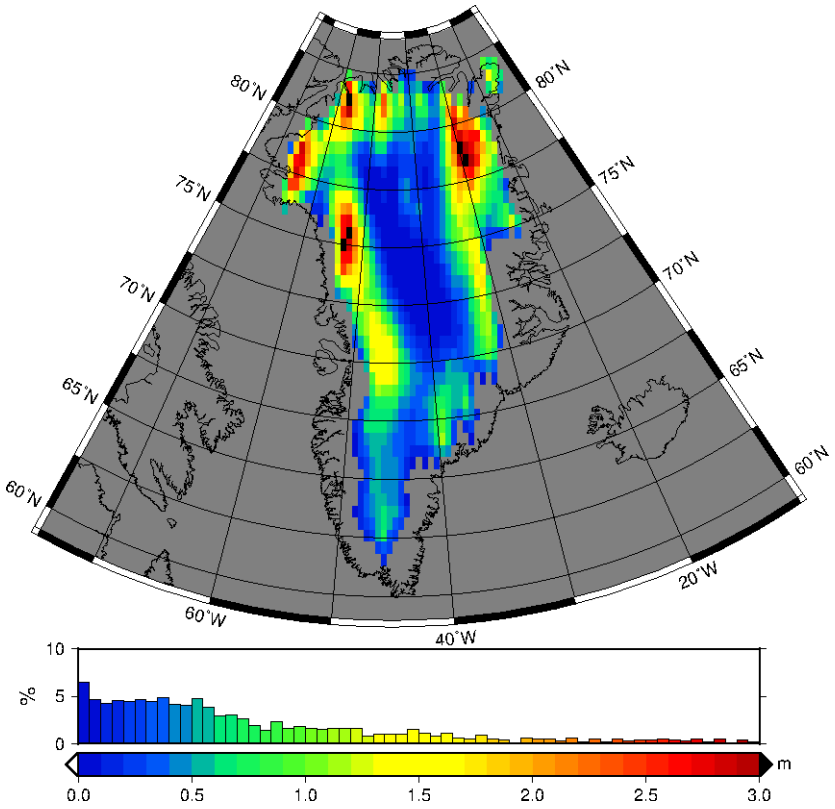

Figure 7.13: **The observed standard error on the elevation changes obtained by using the laplacian differential molecule method on the crossover points from cycles 10 to 20 referenced to cycle number 2.**

coasts, with higher changes for the west coast. While the southern regions show certain increases. Regarding the standard errors the same happens with a significantly higher error in the north and north-west areas of the GrIS.

At this point it must be mentioned that the Laplacian differential molecule method successfully delivers a significantly increased coverage of the GrIS area, what has been one of the main goals for it. However, the constraints and the lack of knowledge about the real dynamics on the coastal margins, leads us to make certain underestimation of the elevation changes happening on these regions. As explained at the beginning of this section the boundary conditions defined for the Laplacian matrix assume an arbitrary boundary limit, due to the difficulty to define what is part of the GrIS and what is non-ice-covered land in Greenland. This leads to a simplification of the boundary problem, where the boundary is defined to lay three 0.5° steps away from the closest measurement and no elevation change is allowed to happen on it.

Each of the three methods presented on this chapter have proven to be capable of delivering coherent estimates of the elevation changes observed on a set of crossover points. The delivered results show similar patterns of a significantly predominant decreasing signal on some regions of the GrIS on all three of them. The validity of each method has not been compared or evaluated deeply on this chapter due to the lack of clear criteria to measure the differences apart from the regional standard errors, which in general are within the same range. The next chapter, focused on the determination of annual volume changes on the GrIS, will give us chance for doing so.

8

Volume Change Estimation

The estimation of the total volume variation of an ice sheet is a complex step where several assumptions and extrapolations are required. On this chapter the estimations on the elevation change obtained on the previous chapter are used to compute the volume changes.

According to Tedesco et al. 2015 [47] Greenland has a total extension of 2.166 million km^2 from which 1.71 million are covered by the GrIS. The volume estimate of the ice in the GrIS is instead of 2.85 10^6 km^3.

As the elevation changes have been obtained using various methods, on this chapter the methods to convert these results into volume changes are presented. First, the linear regression slopes that describe the general trend on the elevation change in the GrIS as explained in section 7.2.2 are used to compute the volume change. In the case of the regionalized elevation changes, regionalized volume changes are computed and summed.

A relevant issue present on each of the cases is that as seen on the previous chapter the estimation of the elevation changes in the GrIS results in some of the regions not being well characterized and thus having lost-data regions. Therefore, for estimating the contribution of these regions to the overall result different strategies has been applied.

A comparison of the four different results obtained from the different methods are listed and compared on the last section 8.4.

8.1. General volume change estimation

Using the general trends on the evolution of the GrIS elevations computed in section 7.2.2 the total volume change over a year period is obtained by assuming that the elevation change is an effective value of the overall elevation change on the whole GrIS.

Thus using the following relation the annual volume change is obtained.

$$\Delta V = \frac{dH}{dt} * t * A = \Delta H_{annual} * A \tag{8.1}$$

In the previous chapter two methods have been applied to obtain the elevation change trends: using all the data indistinctively (case i) and averaging the data into each cycle (case ii).

$$\frac{dH_i}{dt} = -14.327 \pm 4.540\ cm/yr \tag{8.2}$$

$$\frac{dH_{ii}}{dt} = -17.307 \pm 9.336\ cm/yr \tag{8.3}$$

Using these values on equation 8.1 the annual volume changes for each case are computed.

$$\Delta V_i = -245 \pm 78\ km^3 \tag{8.4}$$

$$\Delta V_{ii} = -296 \pm 160\ km^3 \tag{8.5}$$

Both results yield comparable annual estimates of volume change that fall within each others error margins.

8.2. Regionalized volume change estimation

In the case of the regionalized elevation changes the conversion into volume is done by computing the change in each of the individual regions or cells. As done in the previous section the elevation change estimate (dH) of each cell is multiplied with the area (A) covered by the cell (25x25, 50x50, 75x75 and 100x100 km^2 in this case). Thus, the individual volume changes can be added up to make an estimate of the total volume change produced in the GrIS.

However, as already mentioned before, not all the area of the GrIS is well sampled and therefore a significant area signal is lost. In order to compensate for the lost signal the assumption that the lost volume change signal is proportional to the amount of area left uncovered is done. This, to certain extent, leads to an under-estimation of the lost volume change signal as the coastal areas is where the elevation change is predominantly reported to happen.

The piece of code where the volume change calculation is done can be found on the appendix A.4. The GMT '*grdvolume*' utility calculates the area and volume covered between two references from an elevation change grid file input. This allows for the calculation of the area covered in each case and the volume change correspondent to them.

8.2.1. Lost data proportion

Four different size regionalizations have been used for the volume variations and the resulting covered area varies from case to case. The crossover points included in each cell vary significantly as seen on figure 7.8 and it is dependent on the size of the regionalization cell size. This is why a different minimum number is set for each of the cases as the data distribution is different on each of them. A minimum number of 6 crossover points are set as the filter for qualifying the cells' reliability, and due to the low number of points per cell the limit in the 25x25 km^2 case is set to 4. These limits are based on empirical research in order to reduce the out-lying points while keeping a high coverage of the area.

The following table shows the covered area results obtained for the cases and the proportion of the GrIS area that is not covered in extent.

Resolution	Covered area	Covered proportion of the GrIS
25x25 km^2	694639	40.6 %
50x50 km^2	936946	54.8 %
75x75 km^2	1158503	67.7 %
100x100 km^2	1326381	77.6 %

Table 3. The area coverage results for each cell averaging size in km^2.

This shows that using different cell sizes also acts as an extrapolation for areas that do not have data measurements (or not enough) and may help characterizing the whole ice sheet.

8.2.2. Volume changes

As explained before, the volume estimates are obtained by multiplying the size of the cell with the specific elevation change in that cell. In addition, the lost signal area is compensated for by assuming a proportional ice elevation change to the one measured in the covered ice sheet.

As in this chapter the main goal is the estimation of annual elevation changes, another issue to be taken into account is the time passed from the reference cycle to the one that the data points were measured. This is why the time difference of all the crossover points is averaged and the measured elevation changes are re-calculated to a 1 year time difference scale.

The following table lists the annual volume changes calculated using data from cycles 12 and 13 compared to cycle number 2, that comprise the months of April in 2013 and 2014. The selection of these cycles is based on the goal of reducing the impact of seasonal signals by selecting the same periods of the year for the comparison.

Resolution	Measured ΔV	Lost % of the GrIS area	Estimated GrIS ΔV
25x25 km^2	-58	59.4 %	-143
50x50 km^2	-142	45.2 %	-259
75x75 km^2	-154	32.3 %	-227
100x100 km^2	-174	22.4 %	-225

Table 4. The volume change results for each regionalization cell size case in km^3.

The propagation of the uncertainty on the crossover differences to the volume changes is done by calculating the standard deviation of the volume change relation 8.1. It is assumed that the individual cells are independent to each other and that there is no correlation between the deviations in one cell to the contiguous ones.

$$\sigma_{\Delta V} = \sqrt{\sum_{i=0}^{N} A^2 \Delta H_i^2} = A \sqrt{\sum_{i=0}^{N} \Delta H_i^2} \tag{8.6}$$

The compensation for the lost signal areas is also applied on the uncertainty values.

These are the final annual volume change values and their uncertainties.

Resolution	Estimated GrIS $\Delta V \pm \sigma_{\Delta V}$	GrIS area covered
25x25 km^2	-143 $\pm$ 48	40.6 %
50x50 km^2	-259 $\pm$ 127	54.8 %
75x75 km^2	-227 $\pm$ 227	67.7 %
100x100 km^2	-252 $\pm$ 327	77.6 %

Table 5. The final annual volume change estimates with the corresponding standard deviation.

This clearly depicts that the use of big cell sizes, although it delivers higher coverages applying a sort of extrapolation for the uncovered areas itself, at the same time it yields higher standard deviation and thus lower reliability. From the above listed values, the 25x25 km^2 averaging shows a significantly lower estimation due to its low coverage of the GrIS's areas with just a 40.6 % of the land covered. As for the other three estimates, the obtained results agree on a volume change estimate of around -230 to -250 km^3, however, due to the averaging cell sizes the 75x75 km^2 and 100x100 km^2 cases are rejected. This leaves the 50x50 km^2 case as the reliable volume change estimation from the regionalized elevation changes.

$$\Delta V = -259 \pm 127 km^3 \tag{8.7}$$

8.3. Laplacian differential molecule method

As concluded in the previous section it is difficult to give a clear estimate of the volume change of the GrIS without making significant assumptions, and in that same section the lost signal was extracted using big averaging areas and extrapolating the proportional amount of volume change to the uncovered areas. In this section however, as a continuation of the work done on section 7.2.4 the Laplacian differential molecule technique results are used, which already cover most of the GrIS area with an elevation change surface being calculated computationally.

The calculation of the volume estimates for this third method is done in a similar way as with the regionalization method A.4. The volume change observed on the elevation change grid are computed using the '*grdvolume*' GMT utility. The calculation of the Laplacian differential method has been done using a 0.5°x0.5° grid.

The computation has been applied to a data set of 2014 cycle crossovers referenced to the cycle number 2, as explained on the previous chapter for the application of this method properly a higher amount of crossovers is required.

The area covered by the data has been of 1545372 km^2, 90.4 %, what is considerably closer to the value of the complete GrIS area as given in Tedesco et al. 2015 [47].

The final volume change result obtained from this method with its corresponding uncertainty is the following.

$$\Delta V = -289 \pm 36\ km^3 \tag{8.8}$$

8.4. Results

The methods here described have resulted in different estimations of the total annual volume change for the GrIS. When compared to certain extent they all agree as the results are within each ones error margins, as most of the results fall within the same range of 250-300 km ^{3}. The following table lists the results obtained.

The characteristics of each method with their benefits and drawbacks have been described on the specific sections and it could be said that the reliability of each method is proportional to the complexity applied on its computation. Indeed, the more complex analysis done on the regionalized data with the Laplacian minimization yields the most reliable estimation.

Here the list of the final estimates and a final average extracted from them is presented.

Method	Measured ΔV (km^3)	Standard Dev. (km^3)	GrIS Covered area
General i	-245	78	-
General ii	-296	160	-
Regionalized ΔH	-259	127	54.8 %
Laplacian	-289	36	90.4 %
Total Average	- 272	55	-

Table 6. The volume change results of the 4 methods employed, in km^3. With the average from the 4 methods listed below.

9

Linking Volume and Mass Variations

The translation into mass variations of the volume variations for an ice sheet is one of the trickiest parts of the mass balance calculation. A standard volume to mass conversion is done by the multiplication of the volume value with the density of the contained medium, however, on the ice sheets, the estimation of a density value for the volume variations is considerably more complex as the density is not homogeneous on the GrIS and comes from different ice or snow type regions and from different time periods. As an example of these variations, figure 9.1 depicts the relation of the density with the depth from the ice sheet's surface, that shows the slow densification process that the ice sheets go through.

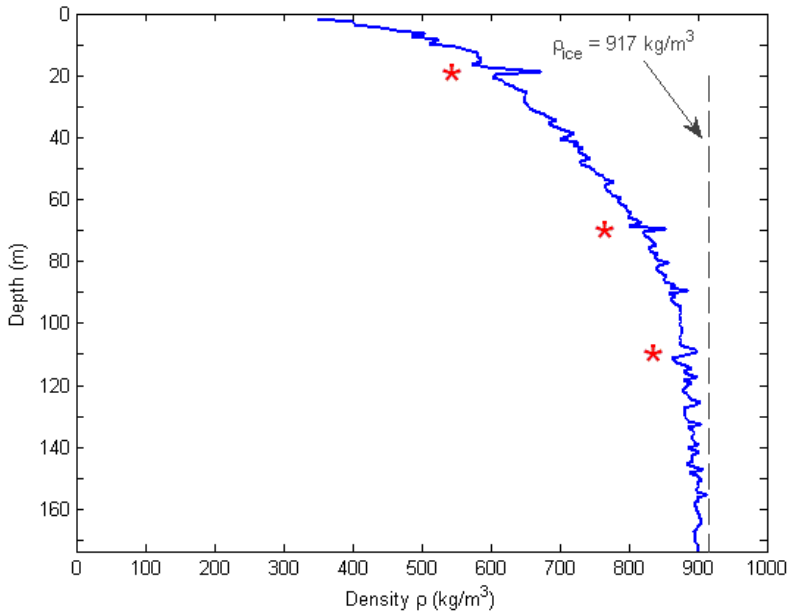

Figure 9.1: **The relation between the ice density and the depth from the ice sheet's surface. [Credit: Centre for Ice and Climate [6]].**

On the literature study prepared on the subject of this thesis, a chapter on the topic of ice density estimation can be found where the most relevant factors and methods in determining the volume to mass conversion rates is introduced. An interesting technique applied to overcome this problem is the identification of the ice type that suffers the ablation. On areas identified to have bigger surface snow

melting are allocated with lower effective densities, around ρ_{ice} = 350 kg/m^3, while areas where the surface mass balance is positive and thus the elevation change mostly comes from the basal ablation are given values similar to the density of ice, ρ_{ice} = 916.7 kg/m^3. In brief, this method identifies the type of ice that is suffering the ablation on certain region and allocates an effective density to that cell. In order to estimate the processes happening at the different layers of an ice sheet, models for monitoring the evolution of each are set, like the calculation of surface mass balances through meteorological models or the use of glacier dynamics applied to the basal melting estimations. All these elements are a necessary input to attempt the identification of the layer that suffers the thinning.

The application of this method of determination of local effective ice density values could have improved the final estimates presented on this thesis project, however, due to time and effort constraints on the development of a MSc thesis, this aspect of the mass balance determination has been left out of this project.

9.1. Mass change with density

In an attempt to get a reasonable, visual and comparable final estimate of the mass change estimate, the volume changes obtained in the previous chapter are translated through an effective density estimate, ρ_{eff}. The selected ρ_{eff} corresponds to the value 900 kg/m^3 that as mentioned by Zwally et al. 2011 [48] is appropriate for long-term solid ice volume changes in ice sheets. Then, through the direct relation of equation 9.1 the mass variation results for each method are obtained and listed on table 7. The error margins have also been translated into the mass magnitude, assuming that all the deviations comes from the volume change estimation.

$$\Delta M = \rho_{eff} * \Delta V \tag{9.1}$$

By directly applying this relation to the volume change estimates on the previous chapter the following is obtained.

Method	Measured ΔM ± Standard Dev.(Gt)
General i	-221 ± 70
General ii	-266 ± 144
Regionalized ΔH	-233 ± 114
Laplacian	-260 ± 32
Total Average	-245 ± 50

Table 7. The mass change results of the 4 methods described on chapter 8 in Gt/yr.

It is interesting to see how these results from different techniques show a convergence around the same estimates, although the result that is more reliable when the calculation process and uncertainty are considered is the last one, the Laplacian differential molecule method. However, a comparison with the results published on other independent researches is necessary.

The following table collects the main mass change estimations published about the GrIS in the last years. In order to more clearly depict the differences the techniques, missions and time periods from which the results come from are also listed.

Period	Measured ΔM $\pm$ Standard Dev. (Gt)	Mission	Reference
2005-2010	-263 $\pm$ 30	various	Sheperd et al. 2012 [15]
2000-2011	-211 $\pm$ 37	various	Sheperd et al. 2012 [15]
2003-2007	-171 $\pm$ 4	ICESat	Zwally et al. 2011 [48]
2003-2008	-191 $\pm$ 23 to -240 $\pm$ 28	ICESat	Sørensen et al. 2011 [10]
2003-2008	-235 $\pm$ 47	ERS-2, ICESat	Hurksman et al. 2014 [45]
2011-2014	-338 $\pm$ 22 (from ΔV)	CryoSat-2	Helm et al. 2014 [11]
2007-2011	-262 $\pm$ 21	InSAR, various	Andersen et al. 2015 [49]
2003-2008	-165 $\pm$ 15	GRACE	Siemes et al. 2012 [50]
2003-2013	-278 $\pm$ 19	GRACE	Schrama et al. 2014 [51]
2013-2014	-260 $\pm$ 32	SARAL/Altika	This study (most reliable method)
2013-2014	-245 $\pm$ 50	SARAL/Altika	This study (final average)

Table 8. Mass change estimates from recent literature publications compared to this study.

When comparing the mass change estimation obtained on this study to the rest of the literature, it can be said that on the broad picture it comes to a close agreement with most of the estimates. More specifically the Laplacian differential molecule method has yielded a result, -260 $\pm$ 32, that is very close to the -263 $\pm$ 30 obtained by Shepherd et al. 2012 [15], the -235 $\pm$ 47 by Hurskman et al. 2014 [18] and the -262 $\pm$ 21 by Andersen et al. 2015 [49] estimates. Some of the other estimates show lower mass loss estimates, as in Zwally et al. 2011 [48] or Siemes et al. 2012 [50]. In these cases it must be noted that they are produced using data from earlier time periods (not taking years from 2008 on) and so a difference could be expected, as the amount of lost mass is steadily increasing. As for Helm et al. 2014 [11], this research presents a higher estimate for the mass loss with -338 $\pm$ 22 Gt/yr, as in the case of Schrama et al. 2014 [51]. They both present estimates than are close to the 300 Gt/yr while covering a time-period up to the 2013-2014, this could show certain underestimation by the method applied on this project.

This last table 8 shows the complexity involved in the calculation of mass change estimates and the difficulty of obtaining accurate results. Overall, it can be said that the mass change value obtained on this study is in agreement with the results published by other independent studies. However, many factors decisively act on the calculation of these final estimates, elements like the different techniques being applied or the time-period from which the data come from are affecting the comparisons. Thus, a more detailed analysis of the effect that different techniques and time-periods, like an accelerated mass-loss, bring on the estimates is required.

10

Discussion

This thesis report has so far presented in a chronological order the main phases of this thesis project, the chapters dedicated to each of them described the details on the development of each phase and introduced the results obtained with a brief analysis. On this chapter the general picture is tackled instead, an overview of the whole project's results is given together with a critical interpretation of the relevant aspects. This discussion is presented on section 10.1. In addition, the applied validation and reliability calculation methods are reviewed and evaluated on sections 10.2 and 10.1.1.

10.1. Results

The introductory chapter defined this thesis project as aimed at the calculation of mass loss estimations on the Greenland ice sheet and at this point it can be said that within reasonable limits this objective has been achieved. Before diving into an overall analysis, several other intermediate results also worth of mention are analysed in this section.

The starting point of this thesis project has been the radar altimetry satellite data files provided by missions like SARAL/Altika or CryoSat-2 and the first phase has attempted the calculation of the thickness of the GrIS over Greenland. For this first intermediate goal, the RADS database has been accessed and the range estimates, together with the atmospheric, geoid shape or instrumental corrections, already available in the database, have been used to compute the first **GrIS thickness estimates**, depicted on figures 6.1 and 6.2 for SARAL/Altika and CryoSat-2 (only LRM mode).

In this regard the computation has been successfully implemented, as proven by the **validation technique** that makes use of a **DEM** produced through independent sources as comparison model, by DiMarzio et al. 2007 [22]. This DEM however, makes use of an EGM96 geoid height model, which is only compatible with the SARAL/Altika data on the RADS database, while the CryoSat-2 data is only available referenced to a EGM2008 geoid model. Another DEM model could have been implemented for the case of the CryoSat-2 data, however, no proper DEM was found for these conditions. This added to the lack of coverage of whole GrIS of the CryoSat-2 LRM mode (the processing of the SARInM data was considered out-of-reach for the time and effort constraints of this thesis project) concluded in the continuation of the project solely with SARAL/Altika data. Therefore, working only for SARAL/Altika, the result from the validation method resulted in figure 6.4 that depicts the differences between the DEM and the calculated thickness values. This result is already interesting as the differences show certain agreement, mostly on the central parts, while it clearly shows an increasing difference as the coast is approached. This phenomena is related to the slope-induced deviations caused by the increasing slopes in the coastal margins of the GrIS, which have been accounted for and corrected in section 6.3.2.

The estimation of the missing **error corrections** not available in RADS, the **dry and wet tropospheric** and **slope-induced error**, have been implemented as explained in the corresponding chapter 6. On both cases, these corrections have reduced the difference between the DEM and the computed thickness as can be seen when comparing the figures 6.10, that includes both corrections, and 6.4 that just represents the GrIS thickness obtained directly from the RADS data. The estimation of the slope-induced error has been able to significantly reduce the behaviour difference between the coastal and interior areas, although the uncertainty remains higher on the outer regions as the estimation of the slope correction on the abrupt coastal areas is more complex.

By focusing more into the **slope-induced deviation** correction, as proven by figures 3.4 and 3.5 the calculation of along- and across-track slope angles by using the satellite track orientation and the DEM values has yielded positive results. The central parts of the GrIS show a plain topography, while the coastal margins show slopes to up to 0.8° what results in significant slope-induced corrections on these margins. This results follow the pattern also shown by a similar calculation by Helm et al. 2014 [11] on page 1546. In addition, the uncertainty distribution on the GrIS elevation change estimates, figure 6.11, is also significantly close to the one presented by Helm et al. in the same article on page 1555 as it ranges from 0 to a few meters on the margins.

With the procedure to compute the corrected thickness estimates from each SARAL/Altika measurement ready, the next phase of the project has established a procedure to compute **elevation changes on the intersection points** between the satellite's ascending and descending tracks from different time periods, the crossover points. Chapter 7 introduces the theory and the method applied on this phase to obtain the values of the ice thickness on crossover points and compute the differences. The cycle number 2 of the SARAL/Altika data set has been selected as the reference cycle to compare the rest of the cycles to, due to it being the earliest cycle on the set and being placed at a relatively stable month, April 2013, when no significant melting or snow accumulation event happens.

Three methods have been applied to compute the elevation changes: overall trends, where all the cycle data are used as a bulk over the whole GrIS; the regionalized pattern, where the elevations are regionally divided and analysed; and the Laplacian differential molecule method, that uses the regionalization scheme and applies a Laplacian minimization to fill the empty regions on GrIS and smooth the elevation changes.

The first method where an **overall trend for the GrIS** is estimated has also been separated into two cases, a first one, where all the elevation change estimates have been considered as equal and a linear regression has been fitted through the more than 140.000 crossover points from cycles 3 (May 2013) to 20 (December 2014). The results has yielded a -14.327 $\pm$ 4.540 cm/yr elevation change overall, what when translated into volume change with a 1.71 million km^2 area of the GrIS accounts for -245 $\pm$ 78 km^3/yr. In the second case, the elevation changes have been averaged per cycle in order to check whether a seasonal signal could be observed on the elevation variation, depicted on figure 7.7. However, with a limited period of time, less than two years, it is complicated to state so, a much longer observation period would have been required. On this second case, a linear fit has also been fitted through the data organized per cycle and the obtained slope has shown an elevation variation of -17.307 $\pm$ 9.336 cm/yr and thus a volume change over the GrIS of -296 $\pm$ 160 km^3/yr.

The second method has applied **regional averages of the elevation changes** on different cell sizes (25x25, 50x50, 75x75 and 100x100 km^2) what results in a regional distribution of the elevation change signal 7.9. For this method the months of April-May from 2014 and 2013 have been compared in order to keep the seasonal effects as limited as possible. This method has enabled the identification of the regions where the elevation change is predominantly happening, like the north-west and north-east coastal regions, while the inner regions of the ice sheet show little variations. In the southern western high-lands some accumulation is observed too. This pattern is also observed in other publications like Sørensen et al. 2011 [10]. A drawback of this method is the lack of reliable coverage in some of the regions, where the measurement conditions are not optimum, as it can be seen on section 7.2.3 not all the area of the GrIS is covered by this method. Thus the elevation change signal is proportionally

extrapolated to the missing area. The volume change estimates from this method have been produced by using different cell sizes 8.2, and the result obtained varies as the used averaging is different and the resulting uncertainty is also higher for bigger cell sizes. Due to the significant difference between each case, the 50x50 km^2 has been selected as the most reliable case, as it delivers the lower standard error with a considerable coverage of the GrIS. This has provided a final volume change estimate of -259 $\pm$ 127 km^3/yr and 54.8% of the GrIS area covered.

A last method applied on the crossover elevation change data is the **Laplacian differential molecule method**, it combines the static information provided by the regionalized elevation change estimates and the dynamic relation between the regions through the Laplacian matrix. The matrix and observations structure has been solved using a least-squares method, where the satellite measurements have been given a weight inverse of their variance. This way a smoother and more complete picture of the GrIS elevation changes has been obtained, figure 7.12. For this calculation due to the higher data requirements all the cycles included in year 2014 have been used, including cycles 10 to 20. This may have included in the data record certain seasonal differences that happen from year to year, however, the use of specific periods, like done in the previous method with months, would have limited the coverage of the results. These elevation change estimates have also been converted into total annual volume changes, giving an estimate of -289 $\pm$ 36 km^3/yr with a coverage of 90.4% of the GrIS.

On the last stage of the project the annual volume change estimates have been translated into **annual mass change** estimations. This process can be extremely complex as the determination of the correct ice density that corresponds to the lost volume ice varies both in time and location. For this project an effective ice density value of ρ_{eff} = 900 kg/m^3, that according to Zwally et al. 2011 [48] represents a reasonable estimate for long-term changes on solid ice, has been used. There are more accurate methods available for making this last step, however, due to the constraints for a MSc thesis project the effective ice density method has been applied. The results yielded by this can be observed in table 7, with a final average estimate of -245 $\pm$ 50 Gt/yr. It must be mentioned that the Laplacian method, the most reliable method applied, has resulted in a -260 $\pm$ 32 Gt/yr annual mass change estimate.

On table 8 most of the mass change estimates available on recent literature has been gathered. The comparison of these results with the estimates obtained on this study shows an agreement around annual estimates around -250 Gt. Most of the studies, [15] [45] [10] [49], show values compatible within margins with the final result of this study. Although it must be noted that these estimates pertain to earlier time period, 2000-2010, while the dynamic during the last half-decade may have changed. The most recent estimate provided by Hurksman et al. 2014 [45] yields a value as high as -338 $\pm$ 22 from CryoSat-2 data. This could to certain extent mean that the present study on the mass changes between 2013-2014 underestimates the real amount of lost mass on the GrIS, however a more detailed analysis would be required to state so.

A few general remarks can be drawn on the overall result and performance. First and foremost, the present study has been able to confirm the GrIS's elevation change patterns and annual mass change estimates reported in other studies. The predominant decrease of the ice sheet on the coastal margins of the north-western and eastern coast are identified as the leading processes on the overall mass loss of the GrIS. A small accumulation increase has also been observed on the inner southern areas.

The schemes produced for the estimation of slope-induced deviations have successfully provided corrections on the range estimates. And in addition, the routines created to calculate and process the elevation changes have proven to work satisfactorily providing reasonable final estimates.

Even though the final result is very satisfactory there are some issues that require some attention. In first place, the lack of longer period satellite data records increases the exposition of the final results to short-term variations and signal noise, reducing their accuracy. The availability of longer satellite data records will allow a better characterization of the overall trends, as well as, of the seasonal signals

on the GrIS. An example of the phenomena that result in short-term variations on the elevation of the GrIS are the hydrological processes, as the water flowing from the melted surface or the discharge of sub-glacial lakes does not necessarily flow out into the oceans, it can go through several re-freezing phases. It is therefore of high relevance that the satellite data record is as long and continuous as possible.

Another relevant issue to consider is the already mentioned loss of signal on the less-homogeneous and steeper margins of the GrIS. The lack of a significant amount of data on these areas results in a lower reliability and thus a poorer monitoring of the areas that show the most prominent elevation changes. This problem is closely related to the tracking process applied on-board that centres the receiver window in order to receive the waveforms centred. However, on rapidly varying regions like the coastal margins this method fails to correctly track the range and a re-tracking post-processing is done on the ground. For this re-tracking, as explained on section 3.1.1, there are several algorithms and the ongoing research aims for the identification of the optimum re-tracker algorithm in order to produce more reliable data on this more poorly covered areas. The currently operational SARInM measurement mode of the CryoSat-2 mission aims to tackle this problem by improving the cross-track resolution of the coastal region measurements and could lead to more accurate results in the future.

10.1.1. Uncertainty

Another relevant aspect has been present on various phases of this thesis project, the calculation of uncertainty at the different intermediate results has enabled to keep a track of the uncertainty of the different magnitudes. The obtained results have been presented together with their linked standard deviations or figures showing the geographical distribution of the uncertainty, like in 6.11, as this accuracy provides a powerful tool to understand the meaning of each result and their trustworthiness.

The calculation of uncertainties has been done by using standard statistical procedures; like the calculation of standard errors for equation fitting (7.12) or the propagation of standard deviation uncertainties from one magnitude to other through the equation that relates them, 6.20, 7.17 or 8.6.

Some of the methods applied have resulted in uncertainties that were at the same order of magnitude as the main values. This has happened in some the regionalization cases due to the considerable assumptions and sizes used on the averaging of the crossover elevation changes. The size of the standard error is clearly related to the size of the boxing used in each case, as it can be seen on table 5. Therefore, the decision to select an intermediate cell sizing that also delivers a considerable coverage of the GrIS, 50x50 km^2 has been taken.

10.2. Validation

Throughout the project development several verification calculations have been done in order to ensure the validity of the obtained results. There are different ways of validating the correctness of the applied methods; some are based on comparisons with reliable sources; others use more sophisticated methods to test that the data and methods fulfil the expected behaviour under certain conditions. On this project several validation tests have been applied at different stages, which were formally described on the previous chapters, and they are analysed from a more general view on this section.

One of the main validation tests applied on the data has been the comparison of the obtained GrIS thickness with a DEM. The used DEM is an ICESat data based elevation model produced by the NSIDC that provides in a stereographic projection the thickness of the GrIS, the data set has been further described on section 6.2. This DEM has been used on the initial phase of the project to validate the results obtained on the first GrIS thickness calculations from the satellite data. The result has been very positive as most of the regions show divergences lower than 10 meters, with values around 0 and 1 meter on the central less steep regions of the ice sheet. In addition, this validation technique has proven the improved thickness estimations obtained when the slope-induced deviation was corrected,

as the difference with the DEM decreased.

Another successful validation has been applied to the independently computed dry and wet tropospheric corrections, as the ones provided in RADS did not include these corrections over the GrIS areas. Depicted on figure 6.7, the dry and wet tropospheric deviation estimations have been compared to the RADS computed ocean estimations in the surroundings of the GrIS. The differences between the two estimations are close to zero, fact that validates the quality of the method applied to get the corrections, although it must be mentioned that due to the use of a different model the RADS estimate for the wet tropospheric effect yields higher values as it does not account for the sea ice covered areas having almost no water vapour and thus suffering no wet tropospheric effect.

In order to check that the processed satellite tracks in the RADS library had not been previously corrected for the effect of the slope-induced deviations, an 8^{th} degree polynomial has been fitted to a pass of the satellite over the GrIS. The test described in section 6.3.2, proves that the satellite track of the altimetry data shows no divergence at all, order of magnitude 10^{-5}, from the nominal satellite orbit track, what proves the fact that the data had not been processed previously.

In an attempt to put some of the more complex results into context, at different phases of the project the results have been compared to similar results obtained in other independent researches. This is the case of the slope-angle determination done for the GrIS in 6.3.2 or the regionalized elevation change, total volume change or total mass change comparisons done throughout chapters 7, 8 or 9. These comparison where in addition accompanied by the calculation of standard deviation values to further support the results.

On a lower relevance level, the backscatter coefficient provided by the satellite data works as a simple validation for the different characteristics of the icy and water surfaces. As depicted on figure 6.3, the backscatter coefficient on the GrIS is significantly higher than in the surrounding sea areas, proving that the energy return from the higher albedo icy surfaces is higher thus proving the expected behaviour of the satellite data and the possibility to use the backscatter coefficient to identify the extent of the ice sheet.

Overall, it can be said that the validation tests have all successfully proven the correctness of the applied methodology and of the obtained results on the different stages of this study.

11

Conclusions and Recommendations

Throughout the core chapters of this report the main results have been described in detail and the discussions chapter 10 delivers a critical overview on the most relevant elements on this study. On this chapter the final conclusions are listed on section 11.1, then followed by some recommendations for future research on section 11.2.

11.1. Conclusions

The main goal of this thesis project, as stated on the introductory chapter, has been to calculate ice sheet mass changes on the Greenland ice sheet using radar altimetry. As explained on chapter 6 the efforts have been centred on processing the SARAL/Altika k_a band altimeter's data available in the RADS library that range from April 2013 to December 2014. The following points gather the main conclusions that have been drawn on this study.

- Confirmed the validity of the radar altimetry processing for monitoring the evolution of ice sheets.
- Successfully applied the computation of GrIS thickness using SARAL/Altika and calculating the required error estimates. The 2D (along- and across-track) slope-induced deviations have been accounted for and an independent DEM has been set-up for validation purposes.
- Created a scheme that computes elevation change estimates at crossover points and successfully analysed these through three different methods.
- Confirmed the validity of the regionalization of crossover point height variations as a technique towards the characterization of the distribution of ice elevation change on the GrIS.
- Applied a Laplacian differential molecule method in order to dynamically relate the regional cells to each other, what has yielded very positive results in terms of area coverage and uncertainty.
- Confirmed that the volume changing occurs predominantly on specific areas of the GrIS, figure 7.12, the elevation loss predominantly happens on coastal areas while the increase is only observed on the southern interior area.
- Quantified annual volume (ΔV) and mass change (ΔM) estimates: -272 $\pm$ 55 km^3/yr and -245 $\pm$ 50 Gt/yr. The obtained values agree within margins with the variations reported in other studies.
- The conventional radar altimetry technique shows certain signal loss on the most abrupt areas of the GrIS. This is related to the error on the tracking of the incoming waveforms, which can be studied and improved by optimizing the post-processing re-tracking carried out on the ground.

- The short length of the data presented on this study leads to higher than desirable noise signal and the difficulty for eliminating the seasonal effect.

11.2. Recommendations

Along with the conclusions drawn on the section above, during the development of this project many interesting research areas and questions have been identified. These research lines could, to some extent, have been part of the project, however due to temporal and effort constrains have not been investigated. The research onto these topics could significantly contribute to the understanding of the evolution of the Earth's ice sheets, as well as improving the quality of the here presented results. On the following paragraphs some recommendations for future work are listed divided on the ones related to the physical modelling of the ice sheets and the ones more related to the software and techniques used on this project.

11.2.1. Physical model

Regarding the physical models and the description of the physical processes studied on this project certain improvements and further research could be applied.

- One of the main drawbacks to be improved with respect to the results presented on this project is the temporal extent of the data measurements. Due to the variability of the year-to-year ice sheet heights a several year-long measurement record is required to eliminate this uncertainty. Currently, due to the short live of the SARAL mission, almost two years, an interesting improvement could consider other mission range records, like ENVISAT or ICESat, in order to observe how it evolves over the lifetime of all the satellites. In this case the differences between different missions would have to be studied and accounted for. It has already been applied for other cases with positive results, Hurksman et al. 2014 [45] did so with the ERS-2 1995-2003 and ICESat 2003-2009 records.

- Studying the density of the ice at which the volume change is happening is another relevant area where improvements could be made. The separation of areas where the melting occurs on snow-like densities or in the ice core could include estimations of surface mass balances through the use of meteorological records.

- The implementation of a signal penetration and volume scattering estimation model in order to eliminate the variability introduced by these phenomena.

- Using the described method on this project on other regions of the Earth's cryosphere like the Antarctic Ice Sheet or the Svalbard and Alaskan glaciers could be an interesting line of research that would for sure raise new questions and observations.

- Due to the time and effort constraints on the development of this project the focus has been put on the SARAL/Altika mission data. Therefore, as also mentioned on the software recommendations, the implementation of the CryoSat-2 data into a study on a similar trend could improve the monitoring of the GrIS, specially with the SARInM data.

11.2.2. Software

As for the possible lines of work for improving the computational part of this project a few main areas can be mentioned.

- Implement the processing of raw ESA or CNES satellite data files. More specifically the implementation of the SARIn mode offered by the SIRAL altimeter on CryoSat-2 would improve the determination of range measurements over the margins of the ice sheets, the area where most of the data is lost on common altimetry.

- The implementation of an updated version of the DEM used for the calculation of the slopes on the satellite track, a DEM more in-line with the period where the satellite data measurements where collected.

- An in-depth analysis of the re-tracker algorithm applied to the data available on RADS could lead to an improvement on both the availability of data and the quality of the measurements overall.

The research along these lines of work could significantly improve the knowledge and precision monitoring of the evolution of the Earth's cryosphere. Therefore, I encourage anyone interested to investigate deeper in any of these and contribute to the humanity's scientific knowledge of the cryosphere.

Bibliography

[1] R. Greve and H. Blatter, *Dynamics of Ice Sheets and Glaciers* (Springer, 2009).

[2] A. C. Brenner, R. A. Bindschadler, R. H. Thomas, and H. J. Zwally, *Slope-Induced Errors in Radar Altimetry Over Continental Ice Sheets,* **88**, 1617–1623 (1987).

[3] A. Cazenave and L. L. Fu, *Satellite altimetry and Earth sciences: A book of techniques and applications* (Academic Press, International Geophysics series 69., 2001).

[4] CNES, *SARAL/AltiKa Products Handbook SALP-MU-M-OP-15984-CN,* (2013).

[5] D. J. Wingham, C. R. Francis, S. Baker, C. Bouzinac, D. Brockley, R. Cullen, P. de Chateau-Thierry, S. W. Laxon, U. Mallow, C. Mavrocordatos, L. Phalippou, G. Ratier, L. Rey, F. Rostan, P. Viau, and D. W. Wallis, *CryoSat: A mission to determine the fluctuations in Earth's land and marine ice fields,* Advances in Space Research **37**, 841–871 (2006).

[6] C. for Ice and f. t. j. A. o. G. Climate, *Flow of ice, densification,* (2015).

[7] IPCC, *Climate change 2007 : An assessment of the intergovernmental panel on climate change,* IPCC panel , 12–17 (2007).

[8] H. J. Zwally and M. B. Giovinetto, *Overview and Assessment of Antarctic Ice-Sheet Mass Balance Estimates: 1992-2009,* Surveys in Geophysics **32**, 351–376 (2011).

[9] M. Mcmillan, A. Shepherd, A. Sundal, K. Briggs, A. Muir, A. Ridout, A. Hogg, and D. Wingham, *Increased ice losses from Antarctica detected by CryoSat-2,* Geophysical Research Letters **41**, 3899–3905 (2014).

[10] L. S. Sørensen, S. Simonsen, K. Nielsen, P. Lucas-Picher, G. Spada, G. Adalgeirsdottir, R. Forsberg, and C. S. Hvidberg, *Mass balance of the Greenland ice sheet (2003–2008) from ICESat data – the impact of interpolation, sampling and firn density,* The Cryosphere **5**, 173–186 (2011).

[11] V. Helm, A. Humbert, and H. Miller, *Elevation and elevation change of Greenland and Antarctica derived from CryoSat-2,* The Cryosphere **8**, 1539–1559 (2014).

[12] T. Thorsteinsson, T. Jóhannesson, and A. Snorrason, *Glaciers and ice caps: Vulnerable water resources in a warming climate,* Current Opinion in Environmental Sustainability **5**, 590–598 (2013).

[13] B. Chellaney, *Water: Asia's new battleground* (Georgetown University Press, 2011).

[14] IPCC, *Climate change 2001 : The scientific basis,* (2003).

[15] A. Shepherd, E. R. Ivins, G. A, V. R. Barletta, M. J. Bentley, S. Bettadpur, K. H. Briggs, D. H. Bromwich, R. Forsberg, N. Galin, M. Horwath, S. Jacobs, I. Joughin, M. a. King, J. T. M. Lenaerts, J. Li, S. R. M. Ligtenberg, A. Luckman, S. B. Luthcke, M. McMillan, R. Meister, G. Milne, J. Mouginot, A. Muir, J. P. Nicolas, J. Paden, A. J. Payne, H. Pritchard, E. Rignot, H. Rott, L. S. Sø rensen, T. a. Scambos, B. Scheuchl, E. J. O. Schrama, B. Smith, A. V. Sundal, J. H. van Angelen, W. J. van de Berg, M. R. van den Broeke, D. G. Vaughan, I. Velicogna, J. Wahr, P. L. Whitehouse, D. J. Wingham, D. Yi, D. Young, and H. J. Zwally, *A reconciled estimate of ice-sheet mass balance.* Science (New York, N.Y.) **338**, 1183–9 (2012).

[16] E. J. O. Schrama and B. Wouters, *Revisiting Greenland ice sheet mass loss observed by GRACE,* Journal of Geophysical Research **116**, B02407 (2011).

[17] E. M. Enderlin, *An improved mass budget for the Greenland ice sheet,* Geophysical Research Letters **41**, 866–872 (2014).

[18] T. J. Hughes, *Ice Sheets* (Oxford University Press, New York, 1998).

[19] R. Sabadini and B. Vermeersen, *Global Dynamics of the Earth: Applications of Normal Mode Relaxation Theory to Solid-Earth Geophysics* (Springer, Modern Approaches in Geophysics, 2004).

[20] W. Farrell, *Earth tides, ocean tides and tidal loading,* Philosophical Transactions of the Royal Society of London. Series A, Mathematical and Physical Sciences **274**, 253 (1973).

[21] R. Forsberg and L. S. Sørensen, *Comprehensive Error Characterisation Report for the IceSheetscci project of ESA's Climate Change Initiative,* **1.2** (2013).

[22] J. DiMarzio, A. Brenner, R. Schutz, C. A. Shuman, and H. J. Zwally, *GLAS/ICESat 1 km laser altimetry digital elevation model of Greenland,* National Snow and Ice Data Center. Digital media. **88** (2007).

[23] A. Patel, J. Paden, C. Leuschen, R. Kwok, D. Gomez-Garcia, B. G. Panzer, M. W. J. Davidson, and S. Gogineni, *Fine-resolution radar altimeter measurements on land and sea ice,* IEEE T. Geoscience and Remote Sensing **53**, 2547–2564 (2015).

[24] F. Rémy and S. Parouty, *Antarctic Ice Sheet and Radar Altimetry: A Review,* Remote Sensing **1**, 1212 (2009).

[25] E. eoPortal, Earth Observation Portal, *Cryosat-2 (earth explorer opportunity mission-2),* (2015).

[26] E. eoPortal, Earth Observation Portal, *Saral (satellite with argos and altika),* (2015).

[27] NORAD, *Saral satellite details,* (2015).

[28] NORAD, *Cryosat-2 satellite details,* (2015).

[29] V. Chobotov, *Orbital Mechanics (3rd edition)* (American Institute of Aeronautics and Astronautics, 2002).

[30] C. Goetz, *CryoSat-2 Precise Orbit Context,* CS-TN-ESA-SY-0239. ESA (16 February 2007).

[31] T. Parrinello, *CryoSat: ESA'S ice Explorer Mission. 4 years in operations: status and achievements.* Geophysical Research Abstracts EGU2014-4996 **16** (2014).

[32] W. Abdalati and H. J. Zwally, *The ICESat-2 laser altimetry mission,* Proceedings of the IEEE **98**, 735–751 (2010).

[33] R. Scharroo, E. Leuliette, J. Lillibridge, D. Byrne, M. Naeije, and G. Mitchum, *RADS: Consistent multi-mission products,* Proc. of the Symposium on 20 Years of Progress in Radar Altimetry, Venice, 20-28 September 2012, Eur. Space Agency Spec. Publ., ESA SP-710 , 4 (2013).

[34] P. Wessel and W. H. F. Smith, *Free software helps map and display data,* EOS Trans. AGU **72**, 441 (1991).

[35] ESA and CNES, *Brat, basic radar altimetry toolbox,* (2015).

[36] Unidata, *Netcdf, network common data form, unidata,* (2015).

[37] J. Snyder, *Map Projections - A Working Manual* (US Geological Survey Professional paper 1395, 1987).

[38] N. G. S. F. Center and Nima, *Egm96 geopotential model,* (2015).

[39] A. C. Brenner, J. P. DiMarzio, and H. J. Zwally, *Precision and Accuracy of Satellite Radar and Laser Altimeter Data Over the Continental Ice Sheets,* IEEE Transactions on Geoscience and Remote Sensing **45**, 321–331 (2007).

[40] E. Kaplan and C. Hegarty, *Understanding GPS: Principles and Applications, Second Edition* (Artech House, 2005).

[41] J. Wertz, *Mission Geometry; Orbit and Constellation Design and Management: Spacecraft Orbit and Attitude Systems* (Springer, 2001).

[42] A. C. Brenner, C. J. Koblinsky, and B. D. Beckley, *A Preliminary Estimate of Geoid-Induced Variations in Repeat Orbit Satellite Altimeter Observations,* Journal of Physical Research **95**, 3033 (1990).

[43] T. W. K. Armitage, D. J. Wingham, and A. L. Ridout, *Meteorological Origin of the Static Crossover Pattern Present in Low-Resolution-Mode CryoSat-2 Data Over Central Antarctica,* IEEE Geoscience and Remote Sensing Letters **11**, 1295–1299 (2014).

[44] H. J. Zwally, *Growth of Greenland ice sheet: Interpretation,* (1989).

[45] R. T. W. L. Hurkmans, J. L. Bamber, C. H. Davis, I. R. Joughin, K. S. Khvorostovsky, B. S. Smith, and N. Schoen, *Time-evolving mass loss of the greenland ice sheet from satellite altimetry,* The Cryosphere **8**, 1725–1740 (2014).

[46] L. S. Sørensen, S. Simonsen, R. Meister, J. F. Levinsen, R. Forsberg, and T. Flament, *Envisat-derived elevation changes of the Greenland ice sheet, and a comparison with ICESat results in the accumulation area,* Remote Sensing of Environment **160**, 56–62 (2015).

[47] M. Tedesco, J. E. Box, J. Cappelen, X. Fettweis, T. Mote, R. S. W. van de Wal, C. Smeets, and J. Wahr, *Greenland ice sheet,* Arctic Report Card: Update for 2014 (January 2015).

[48] H. Zwally, J. Li, A. C. Brenner, M. Beckley, H. G. Cornejo, J. Dimarzio, M. B. Giovinetto, T. a. Neumann, J. Robbins, J. L. Saba, D. Yi, and W. Wang, *Greenland ice sheet mass balance : distribution of increased mass loss with climate warming ; 2003 – 07 versus 1992 – 2002,* Journal of Glaciology **57**, 88–102 (2011).

[49] M. Andersen, L. Stenseng, H. Skourup, W. Colgan, S. Khan, S. Kristensen, S. Andersen, J. Box, A. Ahlstrøm, X. Fettweis, and R. Forsberg, *Basin-scale partitioning of greenland ice sheet mass balance components (2007–2011),* Earth and Planetary Science Letters **409**, 89–95 (2015).

[50] C. Siemes, P. Ditmar, R. E. M. Riva, D. C. Slobbe, X. L. Liu, and H. H. Farahani, *Estimation of mass change trends in the Earth's system on the basis of GRACE satellite data, with application to Greenland,* Journal of Geodesy **87**, 69–87 (2012).

[51] E. Schrama, B. Wouters, and R. Rietbroek, *A mascon approach to assess ice sheet and glacier mass balances and their uncertainties from GRACE data,* Journal of Geophysical Research: Solid Earth **119**, 6048–6066 (2014).

A

Data processing scripts

The GMT utilities have generally been used through script files, the '*awk*' language has also been used on some of the scripts to initially set the data columns in the proper form for the GMT utilities.

A.1. Height profile calculation

This first script just handles the data obtained from the RADS database and computes the range values without applying any correction, followed by the plotting commands that produce the initial plot on the range over the GrIS on a Lambert conic conformal projection.

```
#!/bin/bash
# GMT script to plot
# AVN

#####################################################################
# Initial Settings
# Output file name
ps=tmp.ps

# Create a letter ize bounding box
gmtset PS_MEDIA letter FORMAT_GEO_MAP D
gmtset MAP_GRID_CROSS_SIZE_PRIMARY 0
gmtset FONT_ANNOT_PRIMARY=13
gmtset FORMAT_GEO_MAP=ddd:mmF

#####################################################################
# Process the data of the SARAL/Altika's 8th cycle and the CryoSat2 cycle 2
# range measurement file obtained from RADS database
# Calculate height difference in the data for lon,lat
cat GrIS_Altika_c8.asc | awk '($3-$4-$6-$7-$8-$9-$10>100)&&(($3-$4-$6-$7
  -$8-$9-$10)!~/^nan/){print $2,$1,$3-($4+$6+$7+$8+$9+$10)}' > tmpAlt.xyz

cat GrIS_CryoSat_c2.asc | awk '($3-$4-$6-$7-$8-$9-$10>100)&&($3-$4-$6-$7
  -$8-$9-$10!~/^nan/){print $2,$1,$3-$4-$6-$7-$8-$9-$10}' > tmpC2.xyz

# Create a mean position and value for the data with BLOCKMEAN
blockmean tmpAlt.xyz -R -I0.1 -V > tmpAltb.xyz
blockmean tmpC2.xyz -R -I0.1 -V > tmpC2b.xyz

# Create a grid file z(x,y)
```

```
nearneighbor tmpAltb.xyz -R -S1 -I0.1 -V -GtmpAlt.grd
nearneighbor tmpC2b.xyz -R -S1 -I0.1 -V -GtmpC2.grd


######################################################################
# Plot the data into a file
# Draw Basemap with a Lambert Conic conformal projection
psbasemap -R-75/-10/59/84 -JL-45/75/70/80/20 -B -Y2 -X2 -K -V > $ps

# Create palette - the palette has been manually created: 19palette_1000.cpt

# Plot the grid into the ps image
grdimage tmpAlt.grd -J -C19palette_1000.cpt -R -O -K -V >> $ps
#grdimage tmpC2.grd -J -C19palette_1000.cpt -R -O -K -V >> $ps

# Add vertical color scale
psscale -D22/8.5/13/0.6 -E -C19palette_1000.cpt -B200/:m: -O -K -V >> $ps

# Add coast
pscoast -R -J -Ba20f10g10/a5f2.5g2.5:."GrIS Thickness":WESn -Di -N1/thick
   -A1000 -W1/0.5p,black,solid -V -O >> $ps

# Clean up some temporary files
rm tmp.ps tmp.cpt
rm tmpA.grd tmpC.grd tmpC22.grd
rm tmpA.xyz tmpB.xyz tmpC.xyz tmp.xyz tmp2.xyz tmpAlt.xyz tmpC2.xyz tmpC22.xyz

exit 0
```

A.2. Dry & Wet tropospheric and slope corrections

On this code the dry and wet tropospheric corrections are incorporated into the range calculation and the along- and across-track height profiles are set into files to later calculate the slope angle values from them.

The files $n.along\_profile.xyz$ and $n.across\_profile.xyz$ will contain the height profiles in both orientations for each measurement and the slope values are extracted from these on the C++ code presented on Appendix B.2, where *n* is the cycle number of the input file.

```
#!/bin/bash
# GMT script to plot
# AVN

######################################################################
# Initial Settings
# Clean up general elements
rm tmp.ps tmp.cpt

# Output file name
ps=tmp.ps

# CREATE A LETTER SIZE BOUNDING BOX
gmtset PS_MEDIA letter FORMAT_GEO_MAP D
gmtset MAP_GRID_CROSS_SIZE_PRIMARY 0
gmtset FONT_ANNOT_PRIMARY=13
```

```
gmtset FORMAT_GEO_MAP=ddd:mmF

# Set the input file cycle number on the next names
n=GrIS_Alt_c12
m=GrIS_Alt_c12_track

#####################################################################
# Take Data from the SARAL/Altika 8th cycle and incorporate the dry tropospheric
# data from the SARAL/Altika track file named :: n=GrIS_Alt_c12
# Incorporate the dry tropospheric data and exclude dry+wet $5,$6
# and WGS84 $10
cat $n.asc | awk '(($1)!~/^#/){print $1,$2,$3,$4,$5,$6,$7,$8,$9,$10,$11,$12
  }' > new.xyz
cat $m.out | awk '(($1)!~/^%/){print $4,$5}' > new2.xyz
paste new.xyz new2.xyz | awk '{print $1,$2,$3,$4,$5,$6,$7,$8,$9,$10,$11,$12
  ,$13,$14}' > tmp0.xyz

# Compute the correction, reorganize and geographically filter the added data
# file
cat tmp0.xyz | awk '($3-$4-$7-$8-$9-$11>10.0)&&(($4)!~/^NaN/)&&($2>-75.0)
  &&($2<-10.0)&&($1>59.0)&&($1<84.0)&&(($3-$4-$7-$8-$9-$11+$13+$14)!~/^nan/)
    {print $2,$1,$4+$7+$8+$9+$11-$13-$14,$3,$3-($4+$7+$8+$9+$11-$13-$14),$12}'
      > tmp.xyz

#####################################################################
# Grdtrack for getting the alongtrack height profile for the slope calculation
grdtrack tmp.xyz -GtmpB2.grd -V > tmp2.xyz
# filter out the non-qualifying data points, with NaN
cat tmp2.xyz | awk '($7!~/^NaN/){print $1,$2,$6,$3,$4,$5,$7}' >
   $n.along_profile.xyz

# The cross track profile that will be processed through the C++ code on the
# appendix B.2
grdtrack tmp.xyz -GtmpB2.grd -C6k/1k -V > tmp3.xyz
# filter out the non-qualifying data points, with comments
cat tmp3.xyz | awk '($1!~/^>/){print $1,$2,$3,$4,$5}' > $n.tmpacross.xyz

# Clear some of the files
rm tmp2.xyz tmp3.xyz new.xyz new2.xyz
exit 0
```

A.3. Processing of crossover points

This script processes the crossover point datasets. First it applies the slope correction estimate for each of the time-tagged records using the *sample1d* utility. In this script the $Slope\_correction.txt$ file is used as input for the time-tagged slope correction values that are applied on the crossover points.

```
#!/bin/bash
# GMT script to plot
# AVN

#####################################################################
# Initial Settings
# file name for the incumbent cycles: 6 and 15 and the output figure name
m=GrIS_Alt_c02vs20
n=tmp.ps

# Clean up
```

```
rm $m.ps $n tmp.cpt tmp.xyz tmp0.xyz

#######################################################################
# Create t,z or t,correction record file
cat Slope_correction.txt | awk '($1!~/^#/){print $1,$5,$6}' > tmpS.xyz

# Access the satellite data and classify the crossover points in two groups
# 1, where the old cycle is ascending, and 2, new cycle ascending, and each
# of them separated into ascending (a) and descending (d) too.
cat $m.rxf | awk '($1!~/^#/)&&($4-$3>35.0)&&($12!~/^NaN/)&&(print $3,$7,$5,
  $9-$11-$13-$15-$17-$19,$1,$2}' > tmpR1a.xyz
cat $m.rxf | awk '($1!~/^#/)&&($4-$3>35.0)&&($12!~/^NaN/)&&(print $4,$8,$6,
  $10-$12-$14-$16-$18-$20}' > tmpR1d.xyz
cat $m.rxf | awk '($1!~/^#/)&&($3-$4>35.0)&&($12!~/^NaN/)&&(print $3,$7,$5,
  $9-$11-$13-$15-$17-$19,$1,$2}' > tmpR2a.xyz
cat $m.rxf | awk '($1!~/^#/)&&($3-$4>35.0)&&($12!~/^NaN/)&&(print $4,$8,$6,
  $10-$12-$14-$16-$18-$20}' > tmpR2d.xyz


#######################################################################
# Use sample1d utility over time-tagged slope correction to get a fine
# interpolation file : tmpS.xyz
sample1d tmpS.xyz -I0.00001 -Af -Fa -V > tmpSl.xyz

# Apply the fine interpolation of slope_corrections to get the correction on
# the crossover range files : the output has slope-correction values per group
sample1d tmpSl.xyz -NtmpR1a.xyz -V > $m.tmpSc1a.xyz
sample1d tmpSl.xyz -NtmpR2a.xyz -V > $m.tmpSc2a.xyz
sample1d tmpSl.xyz -NtmpR1d.xyz -V > $m.tmpSc1d.xyz
sample1d tmpSl.xyz -NtmpR2d.xyz -V > $m.tmpSc2d.xyz

# Paste both records on the same file and then the same for each group
paste tmpR1a.xyz $m.tmpSc1a.xyz | awk '{print $5,$6,$1,$2,$3,$4,$8,$9}' >
    tmpRc1a.xyz
paste tmpR1d.xyz $m.tmpSc1d.xyz | awk '{print $1,$2,$3,$4,$6,$7}' > tmpRc1d.xyz
paste tmpR2a.xyz $m.tmpSc2a.xyz | awk '{print $5,$6,$1,$2,$3,$4,$8,$9}' >
    tmpRc2a.xyz
paste tmpR2d.xyz $m.tmpSc2d.xyz | awk '{print $1,$2,$3,$4,$6,$7}' > tmpRc2d.xyz

paste tmpRc1a.xyz tmpRc1d.xyz | awk '{print $1,$2,$3,$4,$5,$6,$7,$8,$9,$10,
  $11,$12,$13,$14}' > tmpC1.xyz
paste tmpRc2a.xyz tmpRc2d.xyz | awk '{print $1,$2,$3,$4,$5,$6,$7,$8,$9,$10,
  $11,$12,$13,$14}' > tmpC2.xyz

# Re-organize and compute the asc. vs desc. group crossover elevation, slope corr.
# differences, slope-corrected crossover differences and standard deviations
cat tmpC1.xyz | awk '($6!~/^nan/)&&($12!~/^nan/)&&($6>20.0)&&($12>20.0){print $2,
  $1,$3,$6,$7,$8,$9,$12,$13,$14}' > tmpDH1.xyz
cat tmpC2.xyz | awk '($6!~/^nan/)&&($12!~/^nan/)&&($6>20.0)&&($12>20.0){print $2,
  $1,$3,$6,$7,$8,$9,$12,$13,$14}' > tmpDH2.xyz

cat tmpDH1.xyz | awk '{print
    $1,$2,$3,$4,$5,$6,$7,$8,$9,$10,$8-$4,$9-$5,$8-$4-($9-$5),
  sqrt($6*$6+$10*$10)}' > $m.DH1xyz
cat tmpDH2.xyz | awk '{print
    $1,$2,$3,$4,$5,$6,$7,$8,$9,$10,$4-$8,$5-$9,$4-$8-($5-$9),
  sqrt($6*$6+$10*$10)}' > $m.DH2xyz

#######################################################################
# prepare the columns for plotting
cat $m.H1xyz | awk '($14>0.0)&&($13<100.0)&&($13>-100.0)&&($14<100.0)
```

```
  {print $1,$2,$13,$4"\t",$12,"\t",$13,"\t",$6,"\t",$10,"\t",$14}' > tmpI1.xyz
cat $m.H2xyz | awk '($14>0.0)&&($13<100.0)&&($13>-100.0)&&($14<100.0)
  {print $1,$2,$13,$4"\t",$12,"\t",$13,"\t",$6,"\t",$10,"\t",$14}' > tmpI2.xyz


######################################################################
# PLOT - uses a similar method as in Appendix A.1
######################################################################

# CREATE A LETTER SIZE BOUNDING BOX
gmtset PS_MEDIA letter FORMAT_GEO_MAP D
gmtset MAP_GRID_CROSS_SIZE_PRIMARY 0
gmtset FONT_ANNOT_PRIMARY=13
gmtset FORMAT_GEO_MAP=ddd:mmF

######################################################################
# Draw Basemap
psbasemap -R-75/-10/59/84 -JL-45/75/70/80/20 -B -Y5.25 -X2 -K -V > $m.ps

######################################################################

nearneighbor tmpI1.xyz -R -S50k -I10k -V -GtmpI1.grd
nearneighbor tmpI2.xyz -R -S50k -I10k -V -GtmpI2.grd

# makes use of manually created elev.cpt color palette

# average the old(ascending) and old(descending) results
grdmath tmpI1.grd tmpI2.grd ADD 0.5 MUL = tmpII.grd -V

q=tmpII.grd

grdimage $q -J -Celev.cpt -R -O -K -V >> $m.ps

psscale -D10.0/-3.5/18/0.6h -E -Celev.cpt -B1/:m: -O -K -V >> $m.ps

# Add coast
pscoast -R -J -Ba20f10g10/a5f2.5g2.5:."GrIS":ESwn -Di -N1/thick -A1000
    -W1/0.5p,black,solid -V -O -K >> $m.ps

######################################################################
# Makes an histogram with the elevation change values
grd2xyz $q -V > histogram.t
cat histogram.t | awk '(($3)!~/^NaN/){print $3}' > histogramI.t
pshistogram -Bya5+l"%" -BWesn histogramI.t -R-5/5/0/10 -JX18/2.5 -Celev.cpt -O
    -Y-3.25 -X1.0 -L0.33p -Z1 -W0.1 -V >> $m.ps

exit 0
```

A.4. Volume change estimate

This script is the one used to process the gridded elevation change estimates and calculate the volume changes.

```
#!/bin/bash
# GMT script to plot
# AVN

# file name
```

```
m=tmp

rm tmp.xyz tmpI1.xyz

cat GrIS_Alt_c2vs10-20_laplace_0.5deg_varweigh.txt | awk '($1<-1.0){print
    $1,$2,$3,$4}' > tmpI1.xyz

cat tmpI1.xyz | awk '($4>-10.0){print $1,$2,$4}' > tmpI1s.xyz

# Compute the regionalizations and math
xyz2grd tmpI1.xyz -R -An -I50k -V -GtmpI1n.grd # number of measurements box
xyz2grd tmpI1.xyz -R -I50k -V -GtmpI10.grd
xyz2grd tmpI1s.xyz -R -I50k -V -GtmpI1s0.grd

# create a grid with covered and uncovered cells, while eliminating low
    reliability cells
grdmath tmpI1n.grd 6 GE 0 NAN -V = tmpI1nNAN.grd

# Eliminate the boxes with too few points and Normalize to annual values
grdmath tmpI10.grd tmpI1nNAN.grd MUL -V = tmpI10b.grd
grdmath tmpI1s0.grd tmpI1nNAN.grd MUL -V = tmpI1s0b.grd

grdmath tmpI10b.grd 0.992768 MUL -V = tmpI1.grd
grdmath tmpI1s0b.grd 0.992768 MUL -V = tmpI1s.grd

# compute the sum of squares of the standard deviations on the cells
grdmath tmpI1s0.grd SQR -V = tmpI1s00.grd
grdmath tmpI1s00.grd SUM -Vl = tmp000.grd

# the area and volume on the grid files is computed
grdvolume tmpI1.grd -Sk -V > tmpV.txt
grdvolume tmpI11.grd -Sk -V >> tmpV.txt

exit 0
```

B

C++ code

On this section the main pieces of the C++ code used on the development of this project are included. They generally take care of processing data written on different data files and computing the desired calculations on them, which in the end is outputted into another data-file.

The section B.2 shows the code that takes care of computing the slope angles from the along- and across-track height profiles. First, using the code on section B.1 the across-track profile is re-formatted in order to fit properly the general slope angle calculation code.

B.1. Across-track height profile formatting

```
#include <iostream>
#include <sstream>
#include <fstream>
#include <stdio.h>
#include <stdlib.h>
#include <math.h>

using namespace std;

//*********************************************************************************************
//
// MAIN
//
//*********************************************************************************************
int main()
{
// Open data files with the height profiles
ifstream mydata;
mydata.open("GrIS_Alt_c21.tmpacross.xyz");
ofstream outdata;
outdata.open("GrIS_Alt_c21.across_profile.xyz");

double lon, lat, thk, thk_0, range, orb_alt;
double la, lo, dist, az, thk_c;
double B_0;

int j = 0;
int m_j;
int m = 200000;
char a[20];
```

```
double la_vec[m];
double lo_vec[m];
double az_vec[m];
double dist_vec[m];
double thk_vec[m];

if(mydata.is_open())
{
  while(!mydata.eof())
  {
    mydata >> lo >> la >> dist >> az >> a;
    //cout << lo << ' ' << la << ' ' << a << endl;
    j++;

    if(a[0]=='N')
    {
      cout << j << ' ';
      cout << "YES " << a << endl;
      thk = 0.0;
    }
    else
    {
      thk = atof(a);
    }

    lo_vec[j] = lo;
    la_vec[j] = la;
    thk_vec[j] = thk;
    dist_vec[j] = dist;
    az_vec[j] = az;

    if(dist == 0.0)
    {
      if(a[0]=='N')
      {
        cout << "CASEEEE A " << a << endl;
        j = j-4;
        mydata >> lo >> la >> dist >> az >> a;
        mydata >> lo >> la >> dist >> az >> a;
        mydata >> lo >> la >> dist >> az >> a;
      }
    }
    m_j = j;
  }
}

for(int i=1; i<m_j; i++)
{
  outdata << lo_vec[i] << '\t' << la_vec[i] << '\t' <<
    dist_vec[i] << '\t' << az_vec[i] << '\t' << thk_vec[i] << '\n';
}

cout << m_j << ' ' << double(m_j-1)/7.0 << endl;

mydata.close();
outdata.close();
return 0;
}
```

B.2. Slope angle determination

```
#include <iostream>
#include <sstream>
#include <fstream>
#include <string>
#include <stdio.h>
#include <stdlib.h>
#include <math.h>
#include <utility>
#include <vector>


# include <cstdlib>
# include <iomanip>
# include <cmath>
# include <ctime>

//# include "llsq.hpp"

#define pi 3.14159265358979323846

using namespace std;


//:::::::::::::::::::::::::::::::::::::::::::::::::::::::::::::::::::::::::/
//:: This function converts radians to decimal degrees /
//:::::::::::::::::::::::::::::::::::::::::::::::::::::::::::::::::::::::::/
double rad2deg(double rad) {
  return (rad * 180.0 / pi);
}

//:::::::::::::::::::::::::::::::::::::::::::::::::::::::::::::::::::::::::/
//:: This function converts degrees to radians     /
//:::::::::::::::::::::::::::::::::::::::::::::::::::::::::::::::::::::::::/
double deg2rad(double deg) {
  return (deg * pi / 180.0);
}

//::::::::::::::::::::::::::::::::::::::::::::::::::::::::::::::::::::::::::::::/
//:: This function calculates the distance between two lat,lon coordinates /
//::::::::::::::::::::::::::::::::::::::::::::::::::::::::::::::::::::::::::::::/
double distance(double lat1, double lon1, double lat2, double lon2) {

   double R_earth = 6371009;

   double dlat1=deg2rad(lat1);
       double dlon1=deg2rad(lon1);
       double dlat2=deg2rad(lat2);
       double dlon2=deg2rad(lon2);

       double dLon=dlon1-dlon2;
       double dLat=dlat1-dlat2;

       double aHarv =
           pow(sin(dLat/2.0),2.0)+cos(dlat1)*cos(dlat2)*pow(sin(dLon/2),2);
       double cHarv = 2*atan2(sqrt(aHarv),sqrt(1.0-aHarv));
       double dist = R_earth*cHarv;

  return (dist);
```

```
}



//****************************************************************************80

void llsq ( int n, double x[], double y[], double &a, double &b, double
    &variance_a )

//****************************************************************************80
//
// Purpose:
//
//   LLSQ solves a linear least squares problem matching a line to data.
//
// Discussion:
//
//   A formula for a line of the form Y = A * X + B is sought, which
//   will minimize the root-mean-square error to N data points ( X[I], Y[I] );
//
// Licensing:
//
//   This code is distributed under the GNU LGPL license.
//
// Modified:
//
//   17 July 2011
//
// Author:
//
//   John Burkardt
//
// Parameters:
//
//   Input, int N, the number of data values.
//
//   Input, double X[N], Y[N], the coordinates of the data points.
//
//   Output, double &A, &B, the slope and Y-intercept of the least-squares
//   approximant to the data. And variance
//
{
  double bot;
  int i;
  double top;
  double xbar;
  double ybar;
  double variance;
//
// Special case.
//
  if ( n == 1 )
  {
    a = 0.0;
    b = y[0];
    return;
  }
//
// Average X and Y.
//
```

```
  xbar = 0.0;
  ybar = 0.0;
  for ( i = 0; i < n; i++ )
  {
    xbar = xbar + x[i];
    ybar = ybar + y[i];
  }
  xbar = xbar / ( double ) n;
  ybar = ybar / ( double ) n;
//
// Compute Beta.
//
  top = 0.0;
  bot = 0.0;
  for ( i = 0; i < n; i++ )
  {
    top = top + ( x[i] - xbar ) * ( y[i] - ybar );
    bot = bot + ( x[i] - xbar ) * ( x[i] - xbar );
  }
  a = top / bot;

  b = ybar - a * xbar;

  double SSE = 0.0;
  for(i=0; i<n; i++){
   SSE = SSE + (y[i]-(b + a*x[i]))*(y[i]-(b + a*x[i]));
  }

  double SSE_A = 0.0;
  for(i=0; i<n; i++){
   SSE_A = SSE_A + (x[i]-xbar)*(x[i]-xbar);
  }

  variance = sqrt(SSE/double(n-2.0));
  variance_a = variance*sqrt(1.0/SSE_A);

  return;
}
//****************************************************************************80




//****************************************************************************80
//
// MAIN
//
//****************************************************************************80

int main()
{

// Open data files with the height profiles
ifstream mydata;
mydata.open("GrIS_Alt_c12.along_profile.xyz");
ifstream mydata2;
mydata2.open("GrIS_Alt_c12.across_profile.xyz");
ofstream outdata;
outdata.open("GrIS_Alt_c12_corrected.txt");

//cout << distance(66,70,66.01,70) << endl;
```

```
int m=50000;
int n=7;

double lo_vector[m];
double la_vector[m];
double thk_vector[m];
double range_vector[m];
double orb_alt_vector[m];
double thk_0_vector[m];
double thk_0_vector2[m];
double across_slope_vector[m];
double along_slope_vector[m];
double thk_std_var[m];
double time_vector[m];

double dist_profile[n];
double height_profile[n];
double dist_profile2[3];
double height_profile2[3];

string line;
double lon, lat, thk, thk_0, range, orb_alt, la, lo, dist, az, thk_c, time, B_0;

char a[20];

int ERROR = 0;
int i=0;
int j=0;

double d, res1,res2,var;

// set cout digit prescision
cout.unsetf ( std::ios::floatfield );
cout.precision(6);
cout.setf( std::ios::fixed, std:: ios::floatfield ); // floatfield set to fixed

if(mydata.is_open())
{
  if(mydata2.is_open())
  {
    while(!mydata.eof() &&!mydata2.eof())
    {
      mydata >> lon >> lat >> time >> range >> orb_alt >> thk >> a;

      if(a[0]!='N')
      {
      //cout << "YES " << a << endl;
        thk_0 = atof(a);
        for(i=0; i<n;i++)
        {
          mydata2 >> la >> lo >> dist >> az >> a;
          thk_c = atof(a);
            if(a[0]!='N')
            {
              ERROR = 1;
              dist_profile[i] = dist*1000.0;
              height_profile[i] = thk_c;
            }else
            {
              cout << "Wrong value (NaN) or end of file " << a << endl;
```

```
                cout << la << ' ' << lo << ' ' << thk_c << endl;
              }
          }

          if(ERROR==1)
          {
            j++;
            //
            // Let's calculate some crosstrack slopes here!!!!!!!!!!!!!!!1
            // The equation::
            // H = H(x) + B*dist(x)

            // The linear fit for the slope value for the height profile
            B_0 = (height_profile[4]-height_profile[2])/(dist_profile[4] -
                dist_profile[2]);

            if(B_0 > -10.0){

              llsq(7,dist_profile,height_profile, res1, res2, var);

              for(i=0;i<n;i++)
              {
                //cout << dist_profile[i] << ' ' << height_profile[i] << ' ';
              }
              lo_vector[j]=lon;
              la_vector[j]=lat;
              time_vector[j]=time;
              range_vector[j]=range;
              orb_alt_vector[j]=orb_alt;
              thk_vector[j]=thk;
              thk_0_vector[j]=res2;
              across_slope_vector[j]=res1;
              thk_std_var[j] =
                  pow(range_vector[j]*sin(res1)/pow((cos(res1)),2.0),2.0)*var*var;
              double z = orb_alt_vector[j]-range_vector[j];

              cout << j << ' ' << time_vector[j] << ' ' << lo_vector[j] << ' ' <<
                  la_vector[j] << ' ' << range_vector[j] << ' ' <<
                  orb_alt_vector[j] << ' ' << thk_vector[j] << ' ' <<
                  across_slope_vector[j] << ' ' << thk_0_vector[j] << ' ' << var
                  << ' ' << z << endl;

              //cout << endl;
            }
          }
        }
        else
        {
        cout << "Wrong value " << a << endl;
          for(i=0;i<n;i++)
          {
            mydata2 >> la >> lo >> dist >> az >> a;
          }
        }
        ERROR = 0;
      }
    }
}

cout << endl << "DATA points :: " << j << endl;
int max_j = j;
```

```
//-------------------------------------------------------------------------------------------------
// Calculation of the ALONG-TRACK SLOPE: using the points in thk_0[], a width of
    6 km wide like for the across, this corresponds to +/-3 datapoints surrounding
    each position
// output: along_slope_vector[]


// Test for the distance function:: distance between SS and delft expected
    1077.11 km
//cout << distance(52.01666,4.36666,43.323611,-1.9847222) << endl << endl;
int k=0;
double range_slope_corrected[m];
double range_slope_corrected2[m];

//for(j=0;j<1000;j++)
for(j=0;j<max_j;j++)
{

  // 5 point slope
  // calculate the distance between the points lat, lon and stablish the profile
      vector
  dist_profile[0] =
      -distance(la_vector[j-2],lo_vector[j-2],la_vector[j],lo_vector[j]);
  dist_profile[1] =
      -distance(la_vector[j-1],lo_vector[j-1],la_vector[j],lo_vector[j]);
  dist_profile[2] = distance(la_vector[j],lo_vector[j],la_vector[j],lo_vector[j]);
  dist_profile[3] =
      distance(la_vector[j+1],lo_vector[j+1],la_vector[j],lo_vector[j]);
  dist_profile[4] =
      distance(la_vector[j+2],lo_vector[j+2],la_vector[j],lo_vector[j]);

  double mean_d = (-dist_profile[0]-dist_profile[1] +dist_profile[2] +
      dist_profile[3] + dist_profile[4])/4.0;

  // 3 point slope
  double mean_d2 = (-dist_profile[1] + dist_profile[2] + dist_profile[3])/2.0;

  // Print some preliminary data
  //cout << endl << endl << "DATA ################" << ' ' << mean_d << ' ' <<
      mean_d2 << endl;
  for(int i=0;i<5;i++)
    //cout << endl << la_vector[j-2+i] << ' ' << lo_vector[j-2+i] << ' ' <<
       dist_profile[i] << ' ' << thk_0_vector[j-2+i] << endl;



  // build the height profile
  height_profile[0] = thk_0_vector[j-2];
  height_profile[1] = thk_0_vector[j-1];
  height_profile[2] = thk_0_vector[j];
  height_profile[3] = thk_0_vector[j+1];
  height_profile[4] = thk_0_vector[j+2];


  // interpolate the values for the slope from thk_0 and distance values

  if(mean_d < 11000 && mean_d > 4000)
  {
    for(int i=0;i<5;i++)
      //cout << endl << dist_profile[i] << endl;
```

```
    //change sign of first 2 distance values
    //dist_profile[0] = -dist_profile[0];
    //dist_profile[1] = -dist_profile[1];

    // Run the least squares algorithm
    llsq(5,dist_profile,height_profile, res1, res2, var);
    along_slope_vector[j] = res1;
    thk_0_vector2[j]=res2;
    range_slope_corrected[j] = range_vector[j]/cos(res1);
    range_slope_corrected2[j] =
        range_slope_corrected[j]/cos(across_slope_vector[j]);
    thk_std_var[j] = thk_std_var[j] +
        pow(range_vector[j]*sin(res1)/pow((cos(res1)),2.0),2.0)*var*var;

  }else if(mean_d2 < 7000 && mean_d2 > 4000)
  {

    // Re-set the profile for 3 points
    dist_profile2[0] = dist_profile[1];
    dist_profile2[1] = dist_profile[2];
    dist_profile2[2] = dist_profile[3];
    height_profile2[0] = height_profile[1];
    height_profile2[1] = height_profile[2];
    height_profile2[2] = height_profile[3];

    for(int i=0;i<3;i++)
      //cout << dist_profile[i] << endl;

    // Run the least squares algorithm
    llsq(3,dist_profile2,height_profile2, res1, res2, var);
    along_slope_vector[j] = res1;
    thk_0_vector2[j]=res2;
    range_slope_corrected[j] = range_vector[j]/cos(res1);
    range_slope_corrected2[j] =
        range_slope_corrected[j]/cos(across_slope_vector[j]);
    thk_std_var[j] = thk_std_var[j] +
        pow(range_vector[j]*sin(res1)/pow((cos(res1)),2.0),2.0)*var*var;

  }else{
    k++;
    along_slope_vector[j] = 0.0;
    range_slope_corrected[j] = 0.0;
    range_slope_corrected2[j] = 0.0;
    thk_0_vector2[j] = 0.0;
    res2 = 0.0;
    thk_std_var[j] = 0.0;

  }

  //corrections

  thk_std_var[j] = sqrt(thk_std_var[j]);

  if( res2 > 1.0 && (pow(across_slope_vector[j],2) > pow(0.0001,2) ||
      pow(along_slope_vector[j],2) > pow(0.0001,2)) )
  {
    double z = orb_alt_vector[j]-range_slope_corrected2[j];

    //cout << endl << endl << "RESULT" << ' ' << j << endl;
```

```
    outdata << setprecision(12) << time_vector[j] << '\t' << lo_vector[j] << '\t'
        << la_vector[j] << '\t' << along_slope_vector[j] << '\t' <<
        thk_0_vector2[j] << '\t' << across_slope_vector[j] << '\t' <<
        range_vector[j] << '\t' << range_slope_corrected[j] << '\t' <<
        range_slope_corrected2[j] << '\t' << orb_alt_vector[j] << '\t' << z <<
        '\t' << thk_vector[j] << '\t' << thk_0_vector[j] << ' ' << thk_std_var[j]
        << '\n';
    //cout << thk_0_vector[j] << ' ' << along_slope_vector[j] << ' ' <<
        thk_0_vector2[j] << ' ' << across_slope_vector[j] << ' ' <<
        range_vector[j] << ' ' << range_slope_corrected[j] << ' ' <<
        range_slope_corrected2[j] << ' ' << orb_alt_vector[j] << ' ' <<
        thk_std_var[j] << ' ' << z << ' ' << thk_vector[j] << endl;
  }

  //cout << endl;
}

cout << endl << "RESULTS :: " << j-k << endl;
cout << "Failed :: " << k << endl << endl;

mydata.close();
mydata2.close();
outdata.close();
return 0;
}
```

C

MATLAB code

MATLAB has been used in certain phases of the project as it offer a highly useful software to handle matrices and managing data stored into them. In addition the vast library of useful code available to the public on the Mathworks community makes it interesting to search, like in the case of the map projection translation MATLAB code offered by the NSIDC that allows coordinate transformation from stereographic (latitude ,longitude) to Cartesian coordinates.

C.1. Laplacian differential molecule method

```
%%%%%%%%%%%%%%%%%%%%%%%%%%%%%%%%%%%%%%%%%%%%%%%%%%%%%%%%%%%%%%%%%%%%%%%%%%%%
%
%    LAPLACIAN DIFFERENTIAL MOLECULE
%
% This MATLAB code applies the Laplacian differential molecule method
% using a set of observations of the GrIS: longitude, latitude, elevation
% change (dH) and the standard deviation.
% First the grid from the GrIS elevation crossover points is created where
% the latitude and longitude represent the axes.
%%%%%%%%%%%%%%%%%%%%%%%%%%%%%%%%%%%%%%%%%%%%%%%%%%%%%%%%%%%%%%%%%%%%%%%%%%%%

% Set the grid limits
ymin = 60.0;
ymax = 85.0;
xmin = -70.0;
xmax = -10.0;
fr = 0.5; % size of the grid cells, half degree

% create the arrays and the grid matrix A
X = (xmin:fr:xmax);
Y = (ymin:fr:ymax);
A = zeros((ymax-ymin)/fr+1,(xmax-xmin)/fr+1);

% the standard deviations grid
S = zeros((ymax-ymin)/fr+1,(xmax-xmin)/fr+1);

% the number of points that falls into each grid cell: n
n = zeros(size(A));

% the code number of each grid cell; core cells: 1; boundary cells: 2;
% out of the GrIS cells: 0
code = zeros(size(A));
```

```
code0 = zeros(size(A));

% fill the matrices with the corresponding values
for i=1:length(h)
   i;
   xind = floor((lo(i)-xmin)/fr +1);
   yind = floor((ymax-la(i))/fr +1);
   A(yind,xind) = (A(yind,xind)*n(yind,xind) + h(i))/(n(yind,xind)+1.0);
   S(yind,xind) = (S(yind,xind) + s(i)*s(i));
   n(yind,xind) = n(yind,xind)+1.0;
end

% Get the standard deviation of each cell:: square-root of the sum of the
% squared standard dev. values and divide it with the number of observations
for i=1:length(Y)
   for j=1:length(X)
      S(i,j) = sqrt(S(i,j))/n(i,j);
   end
end

% Reject the data boxes with few data points
for i=1:length(Y)
   for j=1:length(X)
      if n(i,j)<7
         code(i,j) = 0.0;
         A(i,j) = 0.0;
         S(i,j) = 0.0;
      else
         code(i,j) = 1.0;
      end
   end
end

% Apply 2 growth steps to the core data matrix
for k=1:3
   for i=2:(length(Y)-1)
      for j=2:(length(X)-1)
         if code(i,j+1)==1.0 || code(i,j-1)==1.0 || code(i+1,j)==1.0 ||
             code(i-1,j)==1.0
           code0(i,j) = 1.0;
         end
      end
   end
   code = code0;
end


b = 0.0;
% Set the boundary cells to code number 2
for i=2:(length(Y)-1)
   for j=2:(length(X)-1)
      b = code(i,j+1) + code(i,j-1) + code(i+1,j) + code(i-1,j);
    if code(i,j) == 1.0 && b < 4.0
      code0(i,j) = 2.0;
    else
      code0(i,j) = code(i,j);
    end
   end
end

%imagesc(X,Y,code0);
```

```
% create the observations vectors
OBS = zeros(sum(sum(code)),1); % the observations vector for each grid point
OBS_S = zeros(sum(sum(code)),1); % the standard deviations vector of the OBS
    measurements

% this matrix relates the i,j elements on matrix A, with the observations
% array OBS and OBS_S
pos = zeros(size(A));
k=1;
% Convert the grid into an array: first list the core points and then the
% boundary ones.
for i=1:length(Y)
   for j=1:length(X)
      if code0(i,j)==1.0
         OBS(k) = A(i,j);
         OBS_S(k) = S(i,j);
         pos(i,j) = k;
         k = k+1;
      end
   end
end
for i=1:length(Y)
   for j=1:length(X)
      if code0(i,j)==2.0
         OBS(k) = 0.0;
         OBS_S(k) = 0.0;
         pos(i,j) = k;
         k = k+1;
      end
   end
end

% define the length of the observation vectors
length_obs = length(OBS);
length_obsS = length(OBS_S);

% Build the laplace propagator with the Laplacian and the boundary relations
L = zeros(length_obs);
LS = zeros(length_obsS);
for i=2:(length(Y)-1)
   for j=2:(length(X)-1)
    if code0(i,j) == 1.0
        L(pos(i,j),pos(i,j)) = 4.0;
          L(pos(i,j),pos(i+1,j)) = -1.0;
        L(pos(i,j),pos(i-1,j)) = -1.0;
        L(pos(i,j),pos(i,j+1)) = -1.0;
        L(pos(i,j),pos(i,j-1)) = -1.0;
        LS(pos(i,j),pos(i,j)) = 4.0;
        LS(pos(i,j),pos(i+1,j)) = -1.0;
        LS(pos(i,j),pos(i-1,j)) = -1.0;
        LS(pos(i,j),pos(i,j+1)) = -1.0;
        LS(pos(i,j),pos(i,j-1)) = -1.0;
      end
      if code0(i,j) == 2.0
         L(pos(i,j),pos(i,j)) = 1.0;
         LS(pos(i,j),pos(i,j)) = 1.0;
      end
   end
end
```

```
% Add the observation relations: measurements with the weight
% and set the weight for the measurements with the inverse of the
% elevation change values' variance
w = 1/(var(h));

for i=2:(length(Y)-1)
   for j=2:(length(X)-1)
      if code0(i,j)==1.0
         OBS(length_obs+pos(i,j)) = A(i,j);
         L(length_obs+pos(i,j),pos(i,j))= w;
         OBS_S(length_obsS+pos(i,j)) = S(i,j);
         LS(length_obsS+pos(i,j),pos(i,j))= w;
      end
   end
end

for k=1:4
   x_OBS = L\OBS;
   x_OBS_S = LS\OBS_S;

   sum( OBS_S - LS*x_OBS_S)
   OBS = L*x_OBS;
   OBS_S = LS*x_OBS_S;
   k = k+1;
end

% Convert the solutions on x_OBS back into a grid
dH = zeros(size(A));
SE = zeros(size(S));

%convert the grid into an array
for i=1:length(Y)
   for j=1:length(X)
      if code0(i,j)==1.0
         dH(i,j) = x_OBS(pos(i,j));
         SE(i,j) = x_OBS_S(pos(i,j));
      end
      if code0(i,j)==0.0
         dH(i,j) = NaN;
         SE(i,j) = NaN;
      end
   end
end

% Write all the data into a single matrix to easily write it into
% a text file.
data=zeros(length(X)*length(Y),4);
for i=1:length(Y)
   for j=1:length(X)
      if code0(i,j)==1.0
         data(i+length(Y)*(j-1),1) = X(j);
         data(i+length(Y)*(j-1),2) = Yb(i);
         data(i+length(Y)*(j-1),3) = dH(i,j);
         data(i+length(Y)*(j-1),4) = SE(i,j);
      end
   end
end
```

C.2. DEM grid coordinate conversion

This piece of code makes use of the NSIDC's code to make conversions from polar stereographic map projections to (latitude,longitude) data coordinates.

```
% This code converts the DEM grid from the spherical stereographic to lat lon
    coordinates.
% The grid has the following shape, from DiMarzio et al. 2007
nx=2611;
ny=2782;
DEMx = -890000:1000:1720000;
DEMy = -629000:-1000:-3410000;

% The output will be given on these grids.
Lon=zeros(nx,ny);
Lat=zeros(nx,ny);

for i=1:nx
   for j=1:ny
      i
      [Lat(i,j),Lon(i,j)]=polarstereo_inv(DEMx(i),DEMy(j),6378137.0,0.08181919,70,-45);
   end
end
```